THE UNIVERSITY OF CHICAGO

FIRST OBSERVATION OF ASSOCIATED PRODUCTION OF J/ψ MESON AND W BOSON

A DISSERTATION SUBMITTED TO
THE FACULTY OF THE DIVISION OF THE PHYSICAL SCIENCES
IN CANDIDACY FOR THE DEGREE OF
DOCTOR OF PHILOSOPHY

DEPARTMENT OF PHYSICS

BY

CONSTANTINOS MELACHRINOS

CHICAGO, ILLINOIS

DECEMBER 2013

Στην οικογένειά μου, Χαράλαμπο, Γεωργία, Πέτρο, Ηλέκτρα

Contents

List of Figures

List of Tables

Acknowledgments

This thesis would not be possible without the invaluable support of a lot of people.

First and foremost, I would like to thank Peter Onyisi for showing me the way physics is done passionately, always being supportive and helpful, but also for encouraging me to find the answers by myself to mature as a scientist. His presense in all important meetings gave me a shield of defense against even the most difficult questions.

To Florencia Canelli for assuming the responsibility of being my thesis supervisor, for bearing with me during my ups and downs, and providing me with support through the duration of the PhD.

To Mel Shochet for showing by his example what a young physicist should aspire to be, always sharp, prompt, organized and honest.

To Mark Oreglia for the financial and moral support whenever I needed it. To Jim Pilcher for being a group leader and encouraging us to give talks in regular intervals. To Young-Kee Kim for the inspiring example she sets by being so excited and tireless, and willing to "get her hands dirty" with us.

To the post-doctoral scientists that helped me along the way by giving me technical or professional advice: Antonio Boveia, Joe Tuggle, David Miller, Lauren Tompkins, Guido Volpi, Bjoern Penning, Georgios Choudalakis.

To older and younger graduate students with whom we shared offices, lunches, code tips, weekend trips and worries: Anton Kapliy, Chris Meyer, Sam Meehan, Jordan Webster, Martina Hurwitz, Eric Feng, Imai Jen-La Plante, Yang-Yang Cheng, Ho Ling Li.

To the members of my PhD committee, for their advise, comments and support: Marcela Carena, William Irvine, Frank Merritt.

To the people behind the scenes, who made sure that I was paid in time, that the computers worked, that everything was running smoothly to be able to perform research: Nobuko McNeill, Aspasia Sotir-Plutis, Mary Heinz, Rob Gardner, Charles Waldman, Aaron van Meerten, Nate Yehle, Autym Henderson.

To the BPhysics conveners, Sandro Palestini, Alessandro Cerri, James Catmore and the Onia subconvener and co-author Darren Price, and the rest of the ATLAS BPhysics group for being enthusiastic and supportive of our result throughout.

To the member of the ATLAS editorial board, Marjorie Shapiro, Cesare Bini, Andreas

Korn, Geraldine Conti, for guiding us through the ATLAS publication process and offering insightful comments to improve this analysis and their support.

To my friends in Chicago, for being there, whether it be food, drinks, boardgames, concerts, theaters, celebrations, frustrations, ναργιλέδες, we went through all of this together: Natalia, Dimitris, Chloe, Eliza, Andrea, Dionisis, Pongsakorn, Ben, Tyler, Chris W, Keith, Radha, Stephanie, Angelica, Carlos and the Chileans, Dave, Gabe, Andrea, Katherine, Elisa, Blanca, Crystal.

To my friends in Geneva, for supporting me during the most difficult part of my PhD, and making sure I came through with a smile: Natalie, Konstantinos, Andri, Zenon, Louiza, Nikiforos, Christos, Alexandros, Christia, Yiangos, Valia, Brice, Nikos, Stefanie, Carolin, Dmitry, Samir, Valerio, Matias, Antonella, Silvia, Yisel, Cian, Christina, Andrew and the techs, Mario, Carmen, Lazarides, Eleni, Vaso, Vasilis, Rania, Anastopoulos, Elizabeth, and the doctors and nurses of HUG.

To my friends everywhere for keeping in touch and inviting me to their weddings to celebrate in exotic and not exotic places, and making me feel like I have family everywhere.

To the State Scholarships Foundation of Cyprus, the A.G. Leventis Foundation, the Onassis Scholarship Foundation, the McCormick Fellowship, the US-NSF Student Support award, for financially supporting me through the PhD.

To my family, Charalambos, Georgia, Petros and Electra for their support and providing me with a strong sense of roots, values and humor to face any situation. I dedicate this work to you.

Abstract

Particle physics concerns the understanding of the fundamental building blocks of nature, the production of particles and their interactions. The experimental study of high energy collisions allows us to probe the theoretical predictions pertaining to particles. The Large Hadron Collider was built on the outskirts of Geneva, to accelerate and collide protons at the highest energies ever, and allow for the study of the products of these collisions. The ATLAS detector is designed to detect the particles resulting from the proton–proton collisions and collect the data for further study.

The discovery of the J/ψ meson in 1974 paved the way for the presence of three families of quarks in the Standard Model of Particle Physics. The production mechanism of J/ψ at the LHC is not well understood, and several models have been proposed to explain it, such as the Color Singlet and Color Octet models. The associated production of J/ψ meson with a W boson offers an additional insight on the production of J/ψ.

In this thesis, we report the first observation of the $W^{\pm} + J/\psi$ production using 4.5 fb^{-1} of ATLAS data from proton–proton collisions at center of mass energy of 7 TeV at the Large Hadron Collider. In addition, we measure the cross-section ratio of the $W^{\pm}+J/\psi$ production to the inclusive W production. The results are dominated by statistical uncertainties and suggest that a combination of the different models for J/ψ production is needed to explain J/ψ production.

Chapter 1
Introduction

A poet once said, "The whole universe is in a glass of wine." We will probably never know in what sense he meant that, for poets do not write to be understood. But it is true that if we look at a glass of wine closely enough we see the entire universe.

– Richard Feynman, *The Feynman Lectures on Physics*

Particle physics concerns the study of particles, the smallest fundamental units that make up the observable universe. Since ancient times, Leucippus, and his student Democritus defined the term άτομο (atom), which is Greek for something that is not possible to be further divided. Since then, theoretical and experimental progress has found that atoms consist of a nucleus of protons and neutrons, surrounded by electrons. Furthermore, protons and neutrons themselves are made of quarks. Interestingly, Epicurus posited around 300 B.C. that atoms do not always travel in straight lines, but that these lines of motion are occassionally disturbed, avoiding the implicit determinism of the earlier school of thought, which was only confirmed by quantum mechanics in the early 20$^{\text{th}}$ century. Epicurus also pioneered the scientific method, by insisting that "nothing should be believed, except that which was tested through direct observation and logical deduction".

To study the physics of particles, scientists have devised ways to produce fundamental particles in the laboratory. Protons or electrons are collided in high energies and the particle products of these collisions are studied for clues into how they are produced and how they interact with each other. The principle of conservation of energy allows for the production of more energetic or massive particles, by increasing the energy of collisions. Each time two particles collide, distinct probabilities govern the rate of production of each different product. These probabilities can be calculated using theoretical models, such as the Standard Model of Particle Physics, or measured in experiments built for this purpose. Higher rates of collision can be achieved with advances in technology and allow us to probe rarer processes. Rare processes have a low probability of occurring, which may be due to the energy of the colliding and produced particles, or the rules governing their interactions. Probing even rarer and processes in higher energies allows us to investigate the universe at a time nearer the Big Bang, since it is during that time that particles existed in the form that they are produced in particle collisions.

The Large Hadron Collider was built to further push the forefront of fundamental knowledge in particle physics, and the ATLAS experiment in particular was designed to detect any signs of new physics, as well as allow the study of even rarer processes than before. The first observation of one such rare process, the associated production of charmonium with a vector boson, is reported in this thesis, along with the measurement of its production cross section using 4.5 fb^{-1} of data from proton–proton collisions at 7 TeV.

Following the scientific method posited by Epicurus, the direct observation of the associated production of W and J/ψ is presented in this thesis. Despite the success of the Standard Model of Particle Physics in describing the interactions between quarks and leptons, the mechanism behind the production of J/ψ at hadron colliders is still largely unknown. The observation and measurement of the production cross section of the associated production of J/ψ and W can shed light to the production mechanism of the J/ψ. The experimental apparatus used for this measurement consists of the accelerator of the Large Hadron Collider, and the detectors of the ATLAS experiment. The analysis strategy takes into account considerations such as the choice of dataset, the selection of the experimental signature and the determination of efficiencies and background sources. A fit procedure is used to extract the $W^{\pm}$ + prompt J/ψ signal and calculate the statistical significance of the observation, considering the main sources of uncertainties. The measurement of the production cross section of the $W^{\pm}$ + prompt J/ψ process must take into account both the case where the W and J/ψ are produced from the same partons, as well as the multiple parton scattering production of W and J/ψ, where the W and J/ψ are produced in different partons in the same proton–proton collision. The results are compared with theoretical predictions from different mechanisms of J/ψ production to determine which might be the dominant contribution.

In conclusion, this thesis provides the first experimental results towards understanding J/ψ production through the associated production of vector boson with charmonium. In the interplay between theory and experiment, phenomenologists will be able to use these results to refine their models, and experimental results with more data will contribute further knowledge, when they become possible.

Chapter 2
Theoretical Motivation

I waste much time gaping and wondering. During a walk or in a book or in the middle of an embrace, suddenly I awake to a stark amazement at everything.

– W.N.P. Barbellion, *Journal of a Disappointed Man*

The associated production of W boson and J/ψ meson is described by a range of theoretical models, used to describe the production of W, J/ψ and the associated production of the two particles. In this chapter, a brief overview of the Standard Model of particle physics is presented, followed by a discussion of the theoretical ideas proposed for quarkonia production, along with a discussion of the experimental results on quarkonia.

2.1 The Standard Model of particle physics

The Standard Model of particle physics (SM), proposed by Glashow, Salam and Weinberg in the 1960s [1–3], is a theory that describes the strong and electroweak interactions between quarks and leptons via the mediation of force carriers. The theory has withstood a series of experimental tests, and has predicted the existence of particles before their discovery, and hence is the dominant theory in particle physics. The SM is a non-abelian broken gauge theory based on the group $SU(3)_C \otimes SU(2)_L \otimes U(1)_Y$. $SU(3)_C$ refers to the 'color' charge which is carried by the gluons, mediators of the strong force. The $SU(2)_L$ term denotes the left handed coupling of the weak isospin doublets, which is responsible for the electroweak force, via the photon and W and Z bosons, while $U(1)_Y$ is the weak hypercharge. The model contains three generations of quarks and leptons, with properties as described in Table 2.1.

Antiparticles of the aforementioned particles are also part of the SM and can be produced and interact in a symmetric way as their ordinary counterparts.

The four fundamental forces describe the interactions between the quarks and leptons via the exchange of virtual gauge vector bosons, which are shown in Table 2.2. The gravitational force is not included in the SM, but it is too weak at the scales described by particle physics to matter.

	Fermion	Short-hand	Generation	Charge	Mass	Spin
Quarks	up	u	I	$+\frac{2}{3}$	2.4 MeV	$\frac{1}{2}$
	charm	c	II		1.27 *GeV*	
	top	t	III		171.2 *GeV*	
	down	d	I	$-\frac{1}{3}$	4.8 MeV	$\frac{1}{2}$
	strange	s	II		104 MeV	
	bottom	b	III		4.2 *GeV*	
Leptons	electron neutrino	ν_e	I	0	< 2.2 eV	$\frac{1}{2}$
	muon neutrino	ν_μ	II		< 0.17 MeV	
	tau neutrino	ν_τ	III		< 15.5 MeV	
	electron	e	I	-1	0.511 MeV	$\frac{1}{2}$
	muon	μ	II		105.7 *GeV*	
	tau	τ	III		1.777 *GeV*	

Table 2.1: The three generations of quarks and leptons in the Standard Model.

Quantum Electrodynamics [4, 5] describes the interactions between electrically charged particles via the exchange of a photon, via the following Lagrangian:

$$\mathcal{L} = \bar{\psi}(i\gamma^\mu D_\mu - m)\psi - \frac{1}{4}F_{\mu\nu}F^{\mu\nu} \tag{2.1}$$

where γ^μ are Dirac matrices, ψ and $\bar{\psi}$ are Dirac spinors that represent fermion fields, D_μ is the gauge covariant derivative, and $F_{\mu\nu}$ is the electromagnetic field tensor.

The weak interaction, mediated by the W and Z bosons, is a flavor-changing and parity-violating force. Charged-current interactions occur via the charged $W^\pm$, while neutral-current interactions are mediated by the neutral Z^0. Leptons, quarks, and the W and Z bosons themselves can interact via the weak interaction. However, parity violation dictates that only left-handed fermions can couple with the W and Z bosons.

The electroweak theory comes from the unification of the electromagnetic and weak forces into a single field theory. This is achieved using a parity-violating weak force and a parity-conserving electromagnetic force, in the form of $SU(2)_L \otimes U(1)_Y$, and correctly predicted the neutral-current interactions. The W and Z bosons were discovered at CERN in 1983 [6–8]

Force	Boson	Charge	Mass	Spin
Electromagnetic	photon	0	0	1
Weak	W	± 1	80.4 GeV	1
Weak	Z	0	91.2 GeV	1
Strong	gluon	0	0	1

Table 2.2: The four force carriers in the Standard Model.

and firmly established the electroweak theory.

The mechanism of electroweak symmetry breaking, first described by Brout, Englert and Higgs [9, 10], is mediated by a massive scalar boson and explains how the fundamental particles, including the Higgs boson itself, acquire mass. The mathematical formalism enables the spontaneous breaking of the $SU(2)_L \otimes U(1)_Y$ symmetry to a $U(1)_Q$ symmetry that preserves the original electromagnetic symmetry, but gives rise to mass. The Higgs boson was discovered on July 4$^{\text{th}}$ 2012 by both the ATLAS and CMS experiments using the Large Hadron Collider at CERN [11, 12], and resolved one of the main questions in our understanding of nature.

Quantum Chromodynamics is a non-abelian gauge field theory based on the $SU(3)$ group and describes the strong interaction between quarks and gluons [13]. Gluons can self-interact, which leads to quark confinement, the idea that quarks cannot be observed individually in nature, and asymptotic freedom, the property that makes the force between the quarks be stronger at short distances, decreasing with increasing distance [14–16].

2.2 J/ψ production

Quarkonium is defined as the bound state of a quark and its antiquark. Based on the quark flavor, there exist different families of quarkonia, such as charmonia (charm–anticharm) and bottomonia (bottom–antibottom). The J/ψ meson is an example of charmonium, but more charmonia exist with different mass and spin (such as the χ_c meson). In addition, the Υ meson, is an example of bottomonium, which was discovered in 1977 [17]. The Standard Model cannot explain the production of quarkonium due to the fact that the velocity of the consituent quarks of the quarkonia is orders of magnitude different than the quark rest mass. This is in contrast to high–energy scattering processes, such as the quark–

antiquark annihilation to two gluons, which can be calculated from first principles. The nonrelativistic QCD (NRQCD) formalism is an effective field theory used to overcome the challenge of explaining quarkonia production by factoring out processes with mass similar to the momentum scale, from harder processes [18].

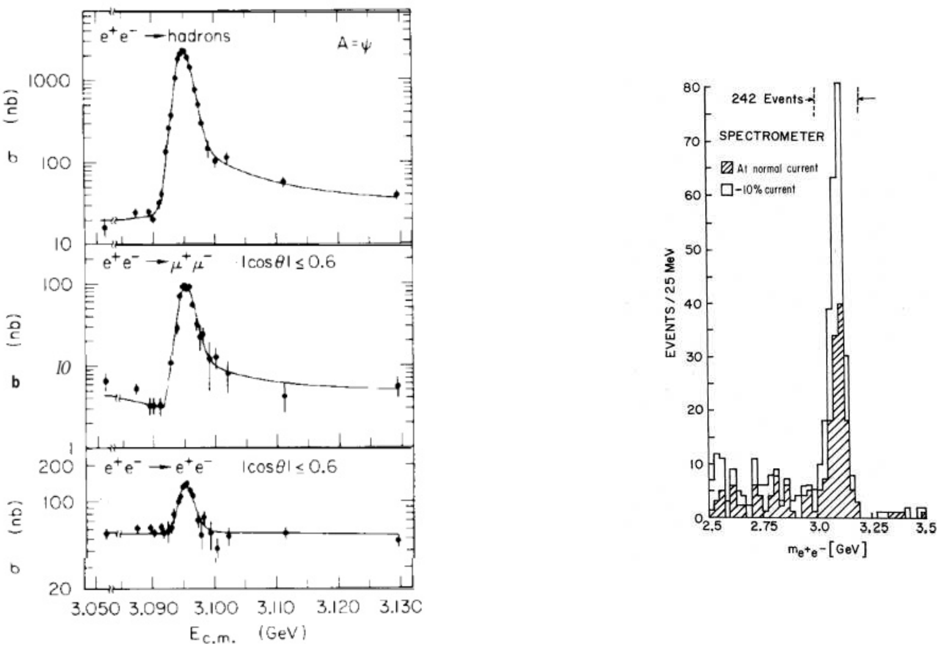

Figure 2.1: The discovery of the J/ψ meson in November 1974 independently by two experiments, SPEAR (left) and AGS (right). Both exhibit peaks in the oppositely charged dielectron mass spectrum consistent with the J/ψ mass at 3.1 GeV.

The J/ψ meson was discovered by two experiments in November 1974 independently, and cemented the quark model as the dominant theoretical description of fundamental particles. The SPEAR experiment at Stanford Linear Accelerator collided electrons with positrons and reconstructed the hadronic mass, the dimuon mass and dielectron mass of the products, all of which had a resonant peak at 3.1 GeV [19]. The AGS experiment at the Brookhaven National Laboratory had a slightly different strategy. It collided protons into Beryllium nuclei, and the dielectron invariant mass showed the same peak at 3.1 GeV [20]. The observation of the J/ψ served to begin the confirmation of the Kobayashi and Maskawa prediction of the presence of six quarks [21], which added a family of quarks to those proposed by Cabibbo [22]. The presence of six quarks was finally confirmed with the top quark observation by CDF and D0 in 1995 [23, 24].

The J/ψ meson is an electrically neutral bound state of a charm-anticharm pair, with mass 3.1 GeV and spin 1. Its orbital angular momentum is 0, and it is characterized by odd charge conjugation and parity [25]. In addition, the J/ψ width is narrower than would be naively expected. The decay of J/ψ to D meson (charm – antiquark pair) is kinematically blocked, since the mass of the J/ψ is smaller than two times the mass of the D meson. The decay of J/ψ to two gluons, that would result in a hadronic signature is forbidden by quantum mechanics, because it violates the charge conjucation parity. The decay to three gluons is accepted, but suppressed due to the OZI rule [26–28], which states that the coupling constant in QCD decreases with increasing energy. Since the gluons must have at least as much energy as the rest mass of the J/ψ, the coupling constant appears small to these gluons. Since strong decays are suppressed, or outright forbidden, the electromagnetic decay of J/ψ to a virtual photon, and consequently to two leptons or hadrons, constitutes $\approx 30\%$ of the total width [25].

Even though it was discovered more than a generation ago, the J/ψ production is not fully understood, as the proposed models fail to predict all of its properties [29–35]. Two of the main models proposed to explain the production of J/ψ are the Color Singlet Model and the Color Octet Model [36–40].

The Color Singlet Model assumes that the J/ψ is produced from the gluon gluon fusion to produce a color singlet J/ψ and a third gluon, following the leading-order decay, also shown in Fig. 2.2:

$$g + g \rightarrow c\bar{c}[J/\psi] + g \tag{2.2}$$

This model has certain shortcomings, since it does not predict the measured cross sections and wrongly predicts that most of the J/ψ's come from χ_c (charm–anticharm pair with higher mass and different spin properties than J/ψ) decays, while measurements show that this is not the case [41].

The alternative, Color Octet Model, uses the NRQCD formalism and predicts the J/ψ production in a soft gluon exchange starting from gluon gluon fusion, according to the decay, also shown in Fig. 2.2:

$$g + g \rightarrow c\bar{c}[J/\psi] + g \tag{2.3}$$

Even though the predicted cross sections of the Color Octet Model agree with the measurements, the expected spin-alignment profile does not agree, which is the shortcoming of the

Color Octet Model.

Figure 2.2: The leading-order Feynman diagrams for J/ψ production in Color Singlet Model (left) and Color Octet Model (right).

Other models have also been proposed, such as the Color Evaporation Model [42], but we focus on these two, since they exhibit differences in the associated production of $W^{\pm}+$ prompt J/ψ, which is the subject of this thesis. In reality, it is possible that the production of J/ψ is not a case of one or another, but a combination of models might be needed to explain it, and is more natural.

2.3 $W^{\pm}+$ prompt J/ψ production

The associated production of $W^{\pm}+$ prompt J/ψ is predicted from both the Color Singlet Model and the Color Octet Model. With the presence of the $W^{\pm}$ boson, the production of $W^{\pm}+$ prompt J/ψ can occur at leading-order only in the Color Octet Model, since the W boson cannot interact strongly, according to the decays, also shown in Fig. 2.3:

$$u\bar{d} \to c\bar{c}[J/\psi] + W^{+}, \bar{u}d \to c\bar{c}[J/\psi] + W^{-} \tag{2.4}$$

The leading-order Color Octet Model contributions to the $W^{\pm}+J/\psi$ production appeared

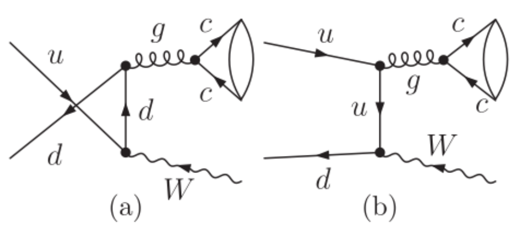

Figure 2.3: The leading-order Feynman diagrams for $W^{\pm}+J/\psi$ production in Color Octet Model.

to dominate in the literature [43, 44], and observation of the $W^{\pm} + J/\psi$ process was seen as the definitive confirmation of the Color Octet Model [37, 38].

Recently, it was proposed that next-to-leading-order Color Singlet Model contributions can have a comparable cross section as the leading-order Color Octet Model predictions [45]. The first Color Singlet Model contribution involves the strange quark - gluon fusion which produces a W +charm pair, where the charm fragments into a J/ψ:

$$s + g \rightarrow W + c + J/\psi \tag{2.5}$$

Another Color Singlet Model contribution produces the J/ψ bound state by an off-shell photon emitted by the quark that also radiates the W boson:

$$q + \bar{q} \rightarrow W + \gamma^* \rightarrow W + J/\psi \tag{2.6}$$

Feynman diagrams for both contributions can be seen in Fig. 2.4. In addition to direct J/ψ

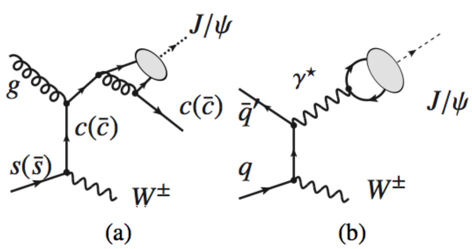

Figure 2.4: Representative Feynman diagrams for $W^{\pm} + J/\psi$ production in Color Singlet Model.

production, J/ψ is produced from χ_c radiative decays, which is taken into account in the Color Singlet Model calculations.

2.3.1 Implications for J/ψ production

The observation of the associated production of $W^{\pm} + J/\psi$ can shed light on the mechanism for J/ψ production at hadron colliders by offering a complementary measurement to direct or indirect J/ψ measurements. The relative importance of the Color Octet and Color Singlet Model contributions to the J/ψ production is still a subject of debate [29–35]. During the

J/ψ production in association with a $W^{\pm}$ boson, different partonic initial states are selected than in direct J/ψ production, and the relative contribution of Color Octet and Color Singlet Models should be different.

In addition, the spin-alignment profile of the J/ψ, which will be described in Section 5.4.2, could be different for direct J/ψ production than from $W^{\pm}+J/\psi$ production. Measuring the spin-alignment for both processes is necessary for better understanding of the J/ψ production mechanism, since it can affect the cross section of the J/ψ.

2.4 Previous searches

The CDF experiment at Fermilab, collided protons and antiprotons at a center of mass energy of 1.8 TeV and 1.96 TeV during two runs. During the first run, using 83 pb^{-1} of data at 1.8 TeV in 1994-1995, a search was performed for the associated production of Υ mesons with vector bosons [46]. The main motivation behind that search was the Higgs boson's branching fraction into ΥW or ΥZ pairs, depending on whether it is charged or neutral, according to various supersymmetric models.

The search was similar to that described in this thesis, in that the final state is the same. The differences lie in the lower expected cross section of the ΥW compared to the $W^{\pm}+J/\psi$, because of the lower mass of the Υ and the lower center of mass energy of the collisions.

The search at CDF found no evidence for ΥW or ΥZ production and set upper limits to the production cross sections. Since then, no search has been performed for $W^{\pm} + J/\psi$ or other associated production of a vector boson with a quarkonium bound state. Hence, this thesis constitutes the first search for associated production of $W^{\pm} + J/\psi$.

Chapter 3
The Large Hadron Collider

Οι πολιτείες ξένες να μας δέχονταν
οι πολιτείες οι πιο απομακρυσμένες

– Νίκος Καββαδίας, *Γράμμα σ'έναν ποιητή*

The Large Hadron Collider (LHC) [47] was built at CERN, in Geneva, Switzerland with the main goal of discovering the mechanism behind Electroweak Symmetry Breaking, and explain how the mass of the W and Z bosons arises, and subsequently that of all fermions and bosons. The LHC was designed to occupy the Large Electron Positron tunnel, a 27-km diameter circular tunnel that sits across the Swiss-French border near Lake Geneva, as seen in Fig. 3.1.

Figure 3.1: The Large Hadron Collider. The Super Proton Synchrotron accelerates the protons and feeds them to the LHC tunnel to collide at the interaction points of four experiments, ATLAS, CMS, LHCb and ALICE.

The LHC was designed to collide protons at a center-of-mass energy of 14 TeV. Protons are generated at the Super Proton Synchrotron by extracting hydrogen atoms from water molecules (H_2O) and expelling the electron in those atoms. These protons are then accelerated in a series of circular apparatus to reach the desired energy, just below the speed of light. Due to an incident with the cables connecting the superconductive magnets of the LHC together, the actual center-of-mass energy during the start-up of the LHC was 7 TeV.

Even at this reduced center-of-mass energy, the LHC achieved the highest energy collisions ever, surpassing the previous record of 1.96 TeV held by the Tevatron [48] by a factor of three. In light of this, the Tevatron shut down its proton-antiproton collision program in 2010. This makes the LHC the only machine for studying physics processes at the energy frontier, ideal for studying rare processes or uncovering previously unobserved processes.

The LHC serves as the accelerator and collider of protons for four main experiments, ATLAS [49], CMS [50], ALICE [51] and LHCb [52]. ATLAS and CMS are multi-purpose detectors which detect a variety of objects produced in proton-proton collisions and study the mechanism of Electroweak Symmetry Breaking and the Standard Model of Particle Physics. ALICE focuses on studying the quark-gluon plasma in heavy ion collisions, while LHCb specializes in studying the bottom quark. The ATLAS detector was used for this thesis and will be described in detail in Chapter 4.

Luminosity is defined as the number of particles that collide per unit area per unit time. The integrated luminosity over time is the measure of the amount of data collected at particle physics experiments. Advances in accelerator physics allow more collisions per unit time, hence more data to be collected. In addition, multiple bunches of protons can be collided at each event, resulting in an even greater amount of data. An event, in particle physics, is the result of the proton–proton collisions as it is saved by the trigger system of an experiment. During the 7 TeV run of the LHC, 5.6 fb^{-1} of data were delivered to each of the experiments ATLAS and CMS, of which 4.5 fb^{-1} were used in this analysis.

Chapter 4
A Toroidal LHC Apparatus

ve sana söylemek istediğim
en güzel söz
henüz söylememiş olduğum sözdür

– Nazim Hikmet, *En güzel deniz*

ATLAS is a multi-purpose detector built for the Large Hadron Collider (LHC) and is shown in Fig.4.1 [49].

ATLAS consists of three main parts, each with specific purposes:

1. the Inner detector, which detects all tracks that are produced from proton-proton collisions
2. the Calorimeters, which detect the energy deposits left by these tracks, and
3. the Muon detectors, which detect the paths of muons that make it all the way through the detector.

In addition, the Toroidal Magnet consists of an inner magnetic solenoid of 2 T magnetic field, which surrounds the Inner Detector, and outer magnetic solenoids of 0.5 T magnetic field, situated within the Muon detectors.

In the following Sections, each of the ATLAS main parts will be described, with an emphasis on the Muon detectors, since the experimental signature of $W^{\pm} + J/\psi$ consists of three muons and missing transverse energy.

4.1 System of coordinates

The coordinate system of ATLAS is typical of particle physics detectors. The z–axis is defined as the proton–proton beam direction, whereas the x–y plane is transverse to the beam direction at the collision point, which is the origin of the coordinate system. The positive x–direction points to the center of the LHC ring, while the positive y–direction points vertically downwards. The transverse momentum $p_{\rm T}$ is defined as the momentum of

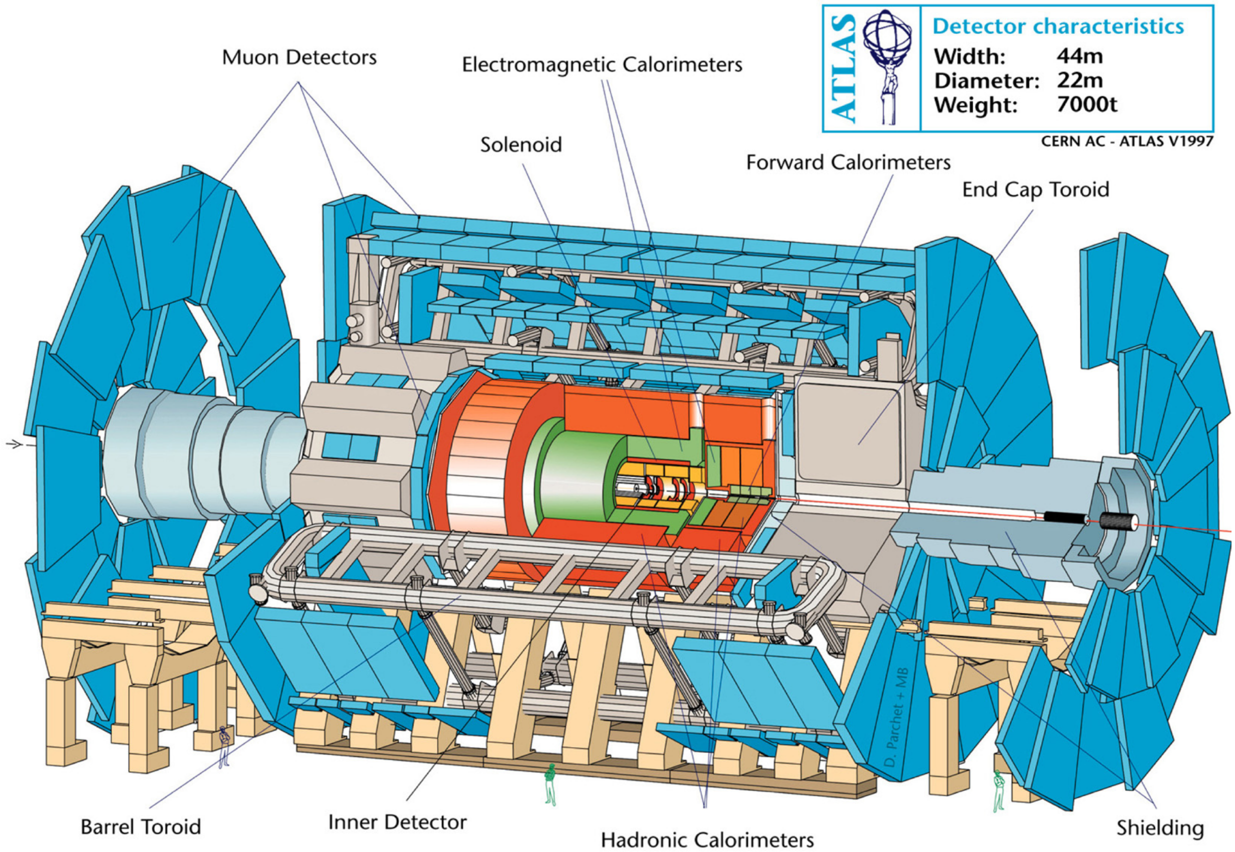

Figure 4.1: The ATLAS experiment. The interaction point is at the center of the detector, surrounded by the Inner detector, which detects all tracks that are produced from proton-proton collisions. Surrounding the Inner detector are the Liquid Argon and Tile calorimeters, which detect the energy deposits left by these tracks. The Muon detectors detect the paths of muons that make it all the way through the detector, and the magnetic solenoids aid in the particle identification and measurement of their properties.

the particle in the x–y plane. The azimuthal angle ϕ is measured around the beam axis and the polar angle θ is measured from the positive z–direction.

Rapidity is defined as

$$y \equiv \frac{1}{2} \ln \frac{E + p_z c}{E - p_z c} \tag{4.1}$$

where p_z is the particle's momentum in the beam direction, E is its energy, and c is the speed of light. Rapidity is Lorentz–invariant along the beam axis, and has the property of moving the observer from the lab frame (collisions frame) to the frame in which the particle moves only perpendicular to the beam. Rapidity is hard to measure for highly relativistic particles, because of difficulties in measuring the total momentum vector, especially at high values of rapidity where the particle is travelling near the z–axis.

The pseudorapidity, defined as

$$\eta \equiv -\ln \tan \frac{\theta}{2} \tag{4.2}$$

is easier to measure for highly energetic particles and is roughly equivalent to the rapidity.

In particle physics, rapidity is often used for quarkonia studies, since these particles do not tend to be too energetic, while pseudorapidity is used in most other cases.

The distance ΔR in pseudorapidity–azimuthal angle (η–ϕ) space is given by $\Delta R \equiv \sqrt{(\Delta\eta)^2 + (\Delta\phi)^2}$.

4.2 Inner detector

The Inner detector is situated nearest the interaction point and consists of high-granularity Pixel detectors, surrounded by Semiconductor Trackers in the barrel and endcap, and Transition Radiation Trackers further out.

The pixel detector consists of three cylinders at the radial positions 50.5 mm, 88.5 mm and 122.5 mm which consist of silicon chips of size 16.4 mm x 60.8 mm and 46 080 pixels. To cover the forward part of the detector, three pixel disks are located on each side of the barrel. As a particle travels through the pixel detector, it leaves a trace of hits that can be combined to reconstruct the track of the particle.

The Semiconductor Tracker system consists of an additional four cylinders of silicon microstrip detectors located further from the pixel detector that enable a better measure of the particles' tracks. In the forward part of the detector, nine disks on each side are used to completely cover the possible tracks.

The Transition Radiation Tracker (TRT) uses straw detectors that consist of a thin wire surrounded by Xenon gas. As charged particles travel through the TRT, they interact with the gas to leave a trail of particles which drift towards the central wire. The drift time, along with the density of the hits in the TRT are used to precisely locate the charged particle, and discriminate between electrons and hadrons in the TRT.

The momentum resolution of the Inner detector is $\Delta p_{\mathrm{T}}/p_{\mathrm{T}} = 0.04\% \times p_{\mathrm{T}} \bigoplus 2\%$ and the impact parameter resolution is 15 μm in the transverse plane.

Fig. 4.2 shows the ATLAS Inner detector, as it is traversed by two tracks at pseudorapidity 1.4 and 2.2.

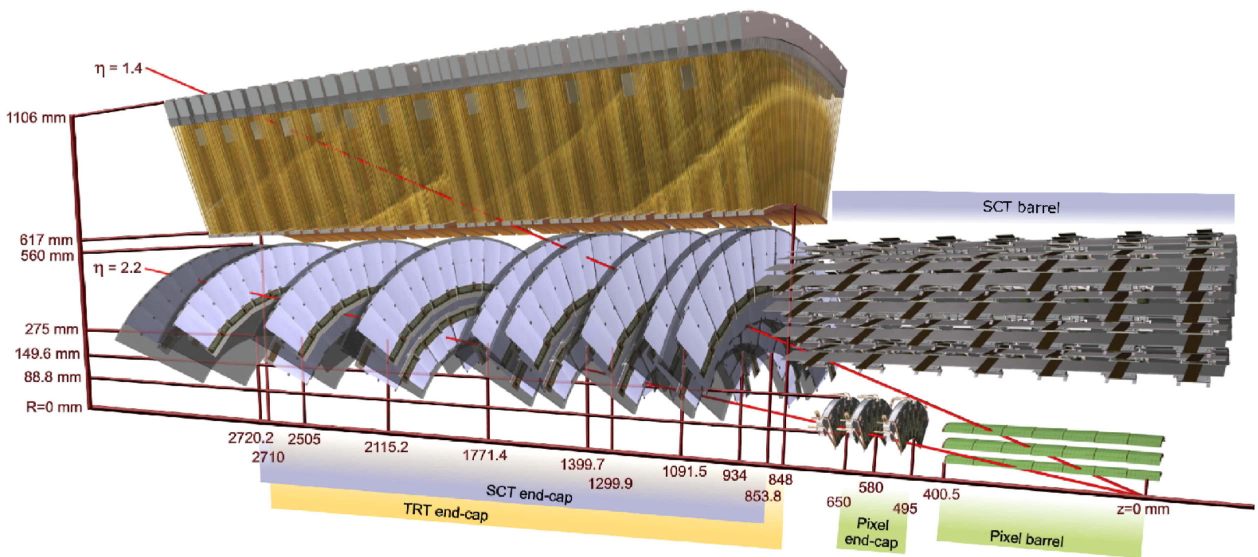

Figure 4.2: The ATLAS Inner detector, consisting of the pixel, SCT and TRT systems, both in the barrel and endcap. Two tracks are shown as they traverse the detector at pseudorapidity 1.4 and 2.2.

4.3 Calorimeters

The Liquid Argon calorimeter (LAr) measures the energy deposits left by particles as they are absorbed by the calorimeter. The LAr has fine granularity and covers the detector up to pseudorapidity, η, of 4.9, while fully covering the detector in azimuthal angle, ϕ. As charged particles pass through the calorimeters, ionization electrons are produced and drift towards the electrodes to produce signals proportional to the deposited energy. The LAr electromagnetic calorimeter provides measurements of the energy of particles with resolution of $\Delta E/E = 11.5\%/\sqrt{E} \bigoplus 0.5\%$, in addition to measuring the polar direction of a particle shower with a resolution of $\Delta\theta = 50\text{mrad}/\sqrt{E}$.

The Tile calorimeter consists of tiles of plastic scintillator cells which detect particles as they are absorbed by the calorimeter. Signals from the tiles are amplified using photomultiplier tubes, and the energy readout is proportional to the energy of the particle. The Tile calorimeter provides measurements of the energy of jets with resolution

$\Delta E/E = 50\%/\sqrt{E} \bigoplus 3\%$, with a segmentation of $\Delta\eta \times \Delta\phi = 0.1 \times 0.1$. Jets are cones of hadrons and other particles produced by the hadronization of quarks or gluons in particle physics experiments.

Fig. 4.3 shows the ATLAS calorimeters.

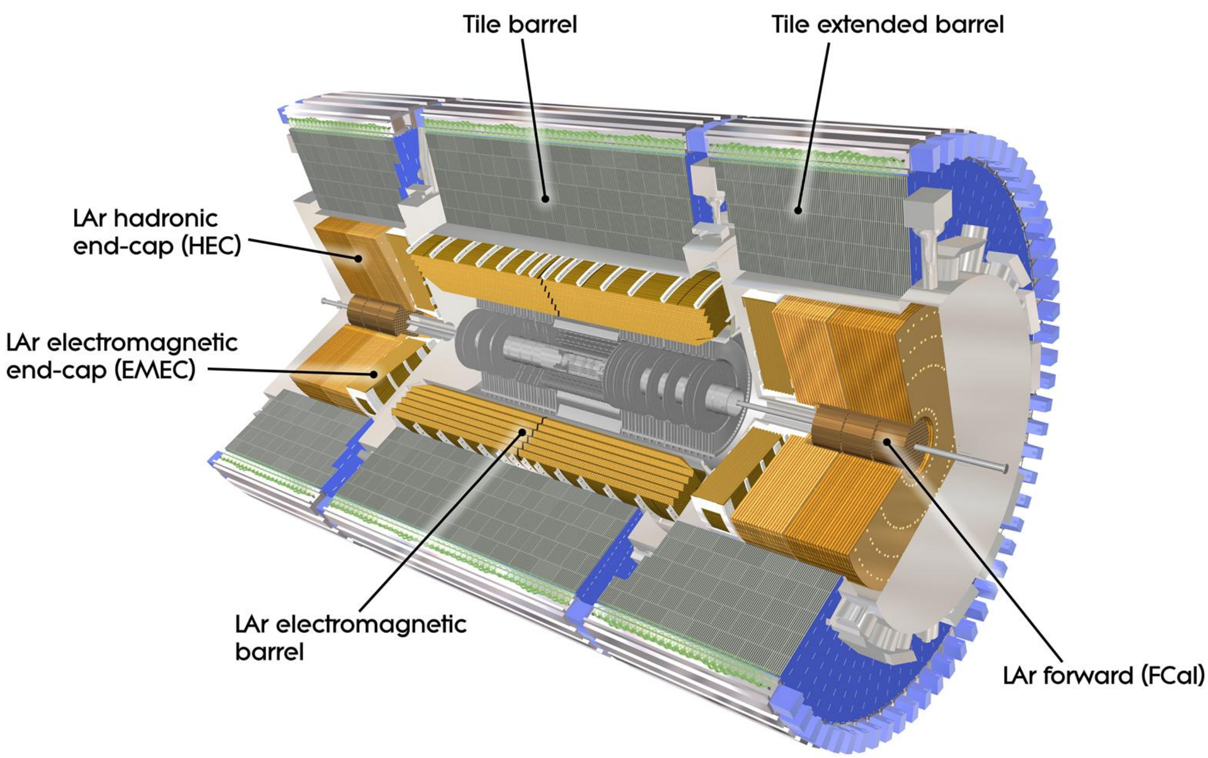

Figure 4.3: The ATLAS calorimeters, consisting of the LAr and Tile calorimeters, both in the barrel and endcap.

4.4 Muon detectors

The ATLAS Muon detector system consists of the Muon Drift Tubes, Cathode Strip Chambers, Resistive Plate Chambers and Thin Gap Chambers. Combining the tracks of the Inner Detector, with the hits of the muon detectors that lie at the outermost layers of ATLAS, yields muon track candidates.

Muon Drift Tubes consist of tubes filled with Argon centered with a 50 μm wire made of Tungsten. They cover a pseudorapidity range up to 2. Cathode Strip Chambers, with an Argon-Carbon Dioxide-Carbon Fluoride gas mixture cover the pseudorapidity range from 2 to 2.7. These constitute the precision chambers, capable of making precise measurements of the hits left by muon tracks on the detector.

Resistive Plate Chambers and Thin Gap Chambers operate with a much coarser space resolution, but faster decision time, making them ideal for triggering, i.e. choosing which collisions are interesting enough to be saved for further analysis, as will be explained in Section 4.5. They cover the pseudorapidity range up to 1.05 and 1.05–2.4 respectively.

The Muon detector system provides a measurement of the momentum of muons with resolution of approximately 10% for 1 TeV tracks, and around 3% for tracks below 100 GeV. Muon momenta down to approximately 4 GeV can be measured in the muon system, but below that, the energy loss at the calorimeters may not allow the muons to escape.

Fig. 4.4 shows the ATLAS Muon detector system.

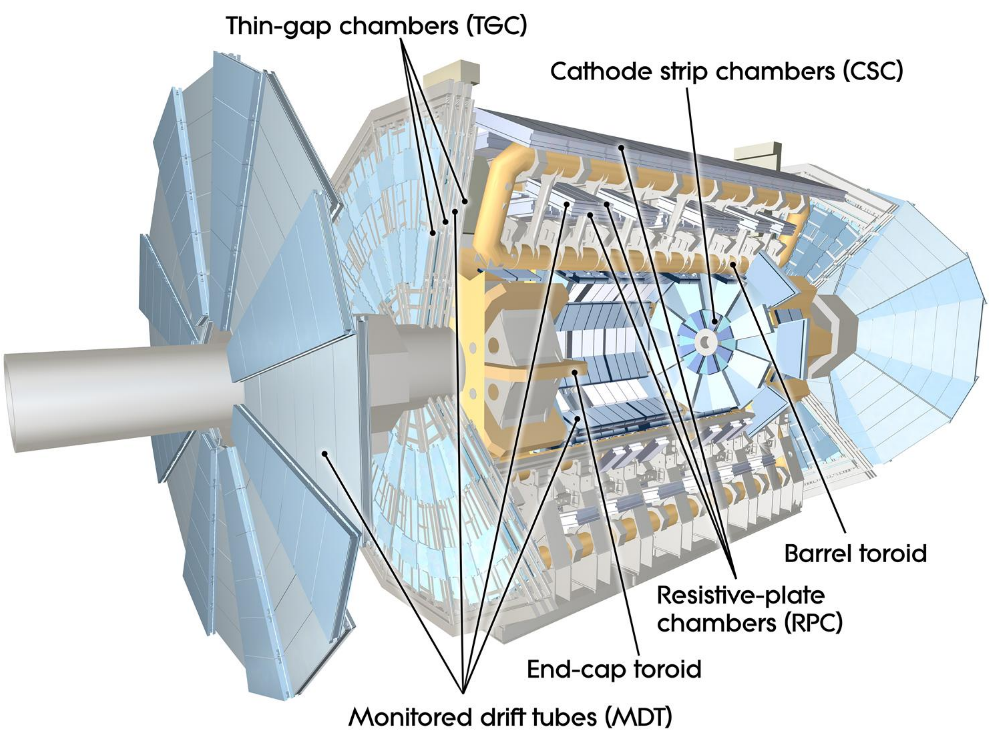

Figure 4.4: The ATLAS Muon detector system, consisting of Muon Drift Tubes, Cathode Strip Chambers, Resistive Plate Chambers and Thin Gap Chambers.

4.4.1 Muon reconstruction

Muon reconstruction at ATLAS occurs using all the aforementioned detectors, with an emphasis on the Muon detectors. Muon tracks with high enough transverse momentum tranverse the whole detector and leave a minimum ionizing energy profile in the calorimeter. "Standalone" muon tracks consist of hits in the muon chambers, that are then extrapolated to the interaction point to combine with the inner detector tracks to give "Combined" muons. "Segment-tagged" muon tracks consist of inner detector tracks that are matched with a segment in the muon detectors, but the segment is not a standalone muon. These are generally muons with lower transverse momentum, hence the muon tracks do not have enough energy to traverse through the whole detector. For the analysis in this thesis, combined and segment-tagged muons are used. In addition, the "STACO" algorithm is used for reconstructing the muons, using a statistical combination of track vectors and co variant matrices from the vertex and the muon inner detector tracks to extract the full track parameters [53].

4.4.2 Missing transverse energy measurement

Neutrinos are not detected in conventional particle detectors due to their lack of interaction with the particle material and their lack of electrical charge. Since they are the only known particle that is undetectable, their presence is inferred by the energy–momentum imbalance in the ATLAS detector, after all other particles are accounted for. Due to the principle of conservation of energy, and since the proton–proton collision is head-on, the total energy at the center of mass momentum frame should be zero. Any deviation from this is recorded as the missing transverse energy, $E_{\mathrm{T}}^{\mathrm{miss}}$. We use the "METRefFinal" algorithm to measure the missing transverse momentum, which takes into account all clusters of energy in the calorimeters, as well as the muon tracks [54].

4.5 Trigger

Thousands of proton–proton collisions occur per second in the ATLAS detector, during normal operations. A limit on the number of events that is possible to save for further analysis exists, due to computational constraints in transferring and saving the data in real time. The ATLAS trigger system aims to choose in each beam crossing the "best" 200 events to be saved for further analysis, according to some criteria. These criteria include the apparent physics interest of the experimental signature, but also the need to include random events, in order to ensure the detection of signatures that are not predictably interesting. The decisions need to be taken in microseconds, since the rate of proton–proton collisions is very high.

There are three levels of triggers, with increasing complexity and decreasing rejection power. The ATLAS trigger system is shown in Fig. 4.5. The Level 1 trigger uses information from the calorimeters and muon detectors to form regions of interest and decide in ≈2 ms whether to save the event in the buffer for the higher trigger levels [55]. The Level 2 and Event Filter Triggers work on the subset of the Level 1 chosen regions of interest and with algorithms can measure more complex objects, such as electrons, missing transverse energy, and dimuon events [56]. In ≈10 ms, the decision whether to save the event is taken by the higher level triggers, and the event moves from the buffer to the readout electronics to be recorded on tape. Only events chosen by at least one trigger are saved for further analysis. The trigger choices for an experiment are crucial for the success of the data collection of such experiment.

For the analysis described in this thesis, we use the `EF_mu18_MG` or `EF_mu18_MG_medium` triggers, depending on the period of the data collection. This stands for an "Event Filter" trigger which requires at least one muon in the event with transverse momentum above 18 GeV and which satisfies some basic isolation criteria to be a "good" muon candidate. Since triggering for muons occurs in the Resistive Plate Chambers or Thin Gap Chambers, the range of pseudorapidity for the triggered muon is up to 2.4, as described in Section 4.4.

4.5.1 The Fast Tracker trigger upgrade

The ATLAS trigger system is efficient and in good condition for data taking at the current conditions of proton proton collisions at 7 and 8 TeV. The upcoming upgrade to the full design energy of 14 TeV, and the subsequent increase in instantaneous luminosity, offers an unprecedented challenge for the trigger. While the rate of collisions will increase, the rate at which we can record and store data for further analysis will stay approximately constant, since the data transfer and storage infrastructure cannot be upgraded to a large extent. For this reason, smarter ways to trigger are necessary.

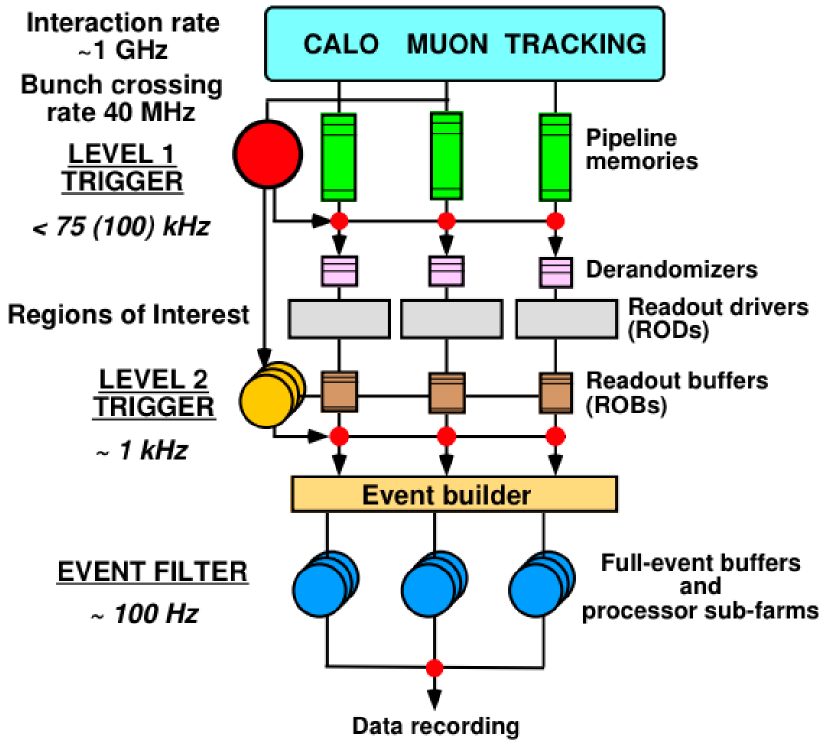

Figure 4.5: The ATLAS trigger system. Information from tracking, muon and calorimeter systems is used at the Level 1 hardware trigger to reduce the rate of events from 1 GHz to below 75 kHz and create the regions of interest to be used for higher level triggers. The Level 2 and Event Filter software triggers further reduce the event rate to a more manageable 200 Hz, to be used for further analysis.

Building on the success of the Silicon Vertex Tracker [57] at CDF, the Fast Tracker Trigger upgrade (FTK) aims to offer an additional hardware trigger layer between Level 1 and High Level Triggers [58, 59]. FTK will use associative memory banks to match the hits in the Inner Detector with offline "roads" and determine whether the event should be saved for further analysis. FTK is doing this at the hardware level, which is faster than software-based trigger systems. The FTK output, FTK tracks, can be used directly by the higher level trigger system, in addition to the Level 1 trigger regions of interest, which can use the additional time to run more sophisticated algorithms to enable even higher efficiency and better resolution for the helix parameters of the track than before.

Chapter 5
Analysis

Κυτάχτε τώρα τον Κωστάκη
Θαρρεί πως κάτι είναι που γράφει.

– Κώστας Μόντης, *Περί ποιήσεως*

For the results presented in this thesis, we use data from the ATLAS detector to detect and measure the cross section of the associated production of $W^{\pm}$+prompt J/ψ. The analysis strategy to select the experimental signature, the fit procedure to establish the observation of the process, and the details to take into account when performing the measurement are explained in this Chapter.

5.1 Strategy

The analysis serves two objectives:

1. The observation of associated production of $W^{\pm}$ + prompt J/ψ
2. The measurement of the cross section ratio $W^{\pm}$ + prompt J/ψ:W

We look for $W^{\pm}$ + prompt J/ψ in the decay channels $W^{\pm} \to \mu^{\pm}\nu$ and $J/\psi \to \mu^{+}\mu^{-}$ in 4.5 fb^{-1} of ATLAS data at 7 TeV center of mass energy proton-proton collisions. As such, our final state consists of three muons and missing transverse energy ($E_{\mathrm{T}}^{\mathrm{miss}}$). We do not consider the electron decay channel of the W boson because the multi-jet background is dominating the low statistics of this process. Processes with lots of jets, particles resulting from the hadronization of quarks and gluons, can easily mimic the signature of the electron, which is also detected in the calorimeter. The di-electron decay of the J/ψ is not considered because electrons of low transverse momentum are not detected to great accuracy with our detector. The dataset used in this analysis is described in Section 5.2, while the criteria to select the experimental signature are shown in Section 5.3.

The cross section of a physics scattering process is defined as:

$$\sigma \equiv \frac{N}{\mathcal{L} \times \epsilon \times \mathcal{A}} \tag{5.1}$$

where N is the number of events observed, $\mathcal{L}$ is the integrated luminosity of the data used, ϵ accounts for the efficiency of detecting the particles due to detector effects, and $\mathcal{A}$ accounts for the acceptance of detecting the J/ψ due to the spin-alignment of the J/ψ. These will be explained in Section 5.4.

For this analysis, we measure the cross section ratio of the $W^{\pm}$+prompt J/ψ production divided by the inclusive W production, $R_{J/\psi}$:

$$R_{J/\psi} \equiv \frac{\sigma_{W+J/\psi}}{\sigma_W} \equiv \frac{\frac{N_{W+J/\psi}}{\mathcal{L}\times\epsilon_W\times\epsilon_{J/\psi}\times\mathcal{A}_{J/\psi}}}{\frac{N_W}{\mathcal{L}\times\epsilon_W}} \equiv \frac{N_{W+J/\psi}}{N_W \times \epsilon_{J/\psi} \times \mathcal{A}_{J/\psi}} \tag{5.2}$$

The uncertainties related to the luminosity and the W production, as well as the efficiency of the W, cancel out in the ratio, leaving only the efficiency and acceptance related to the J/ψ in the final ratio measurement.

Background processes are physics processes that exhibit a similar experimental signature to the signal process, in this case the $W^{\pm} + J/\psi$. In Section 5.5, the various sources of backgrounds are described, along with the steps taken to eliminate them, or take them into account when establishing the signal process.

The multiple parton scattering contribution to the $W^{\pm}$+prompt J/ψ signal is considered in Section 5.6, along with an estimate of the amount of this contribution.

5.2 Dataset

We use the proton–proton collision data collected by the ATLAS detector between March and December 2011, with the LHC operating at a center-of-mass energy of 7 TeV. Since we are especially interested in final states with three muons and $E_{\mathrm{T}}^{\mathrm{miss}}$, we use the "muon stream" of data, a pre-selected group of events that contains at least one muon with transverse momentum above 5 GeV. In addition, we require that all ATLAS sub-detectors operate normally and use a "Good Run List"[1] prepared by the ATLAS Data Preparation group to select the runs which are good to use according to specific requirements.

We use a multitude of simulated samples to model the main background processes using Monte Carlo (MC) and detector–level corrections. Different MC generators handle different

1. `data11_7TeV.periodAllYear_DetStatus-v36-pro10-02_CoolRunQuery-00-04-08_All_Good.xml`

sources of physics processes, or different effects from the detector, such as hadronization, with varying accuracy. The main result of this analysis is data–driven. The simulated samples are not used in the derivation of the results, but rather as cross–checks of the procedure and for the purposes of modelling the background processes when designing the analysis, as will be described in this Chapter.

Table 5.1 summarizes the MC samples we used for this analysis, while each background will be specifically explained in Section 5.5.

5.3 Selecting the experimental signature

The $W^{\pm} + J/\psi$ final state in the muon decay channel consists of a muon and a neutrino from the W boson, and two oppositely charged muons from the J/ψ meson. These muons have different properties amongst each other and with respect to the background, and we optimize our selection of the experimental signature to reflect that.

The muon from the W decay tends to have high transverse momentum (p_{T}), in contrast to the muons from the J/ψ decay. In order to select a sample for further analysis, a trigger must be fired, and single lepton, high-p_{T} triggers are the most efficient triggers. For this reason, we require the muon originating from the W to match the `EF_mu18_MG(_medium)` trigger, as explained in Section 4.5. In addition, since the neutrino cannot be detected in the ATLAS detector, events with a W tend to have an energy-momentum imbalance. This is measured by adding vectorially all momentum contributions from detected particles, and taking the momentum vector in the opposite directions to define the missing transverse energy $E_{\mathrm{T}}^{\mathrm{miss}}$, as explained in Section 4.4.2. Combining muon originating from the W and the $E_{\mathrm{T}}^{\mathrm{miss}}$, we can calculate the W boson transverse mass, $M_T(W)$:

$$M_T(W) = \sqrt{2E_{\mathrm{T}}^{\mathrm{miss}} p_{\mathrm{T}}(\ell)(1 - \cos\Delta\phi(\ell, E_{\mathrm{T}}^{\mathrm{miss}}))} \quad (5.3)$$

which is expected to have a different shape for W events, than for multi-jet background events. Multi-jet events are products of the proton–proton collisions that contain a multitude of jets, of which at least one could mimic the muon signature, as will be explained in Section 5.5.1. The muon originating from the W is required to have p_{T} greater than 25 GeV and fall within the pseudorapidity range $|\eta| < 2.4$ to ensure high trigger efficiency.

Process	$\sigma\times$ BR (pb)	k-factor	Generator Efficiency	Effective Lumi (pb^{-1})	Sample Tag
Alpgen W+jets $\to e\nu$	6.9e+03	1.2	1.0	4.2e+02	107680
	1.3e+03	1.2	1.0	1.6e+03	107681
	3.8e+02	1.2	1.0	8.4e+03	107682
	1.0e+02	1.2	1.0	8.3e+03	107683
	26.	1.2	1.0	8.1e+03	107684
	7.0	1.2	1.0	8.4e+03	107685
Alpgen W+jets $\to \mu\nu$	6.9e+03	1.2	1.0	3.7e+02	107690
	1.3e+03	1.2	1.0	1.6e+03	107691
	3.8e+02	1.2	1.0	8.4e+03	107692
	1.0e+02	1.2	1.0	8.3e+03	107693
	26.	1.2	1.0	8.3e+03	107694
	6.9	1.2	1.0	8.5e+03	107695
Alpgen W+jets $\to \tau\nu$	6.9e+03	1.2	1.0	3.9e+02	107700
	1.3e+03	1.2	1.0	1.6e+03	107701
	3.8e+02	1.2	1.0	8.3e+03	107702
	1.0e+02	1.2	1.0	8.3e+03	107703
	26.	1.2	1.0	8.2e+03	107704
	7.0	1.2	1.0	7.7e+03	107705
Pythia W+jets $\to e\nu$	1.0e+04	1.0	1.0	1.0e+04	106043
Pythia W+jets $\to \mu\nu$	1.0e+04	1.0	1.0	1.0e+04	106044
Pythia W+jets $\to \tau\nu$	1.0e+04	1.0	1.0	1.0e+04	107054
Alpgen Z+jets $\to ee$	6.7e+02	1.2	1.0	8.0e+03	107650
	1.3e+02	1.2	1.0	8.0e+03	107651
	41.	1.2	1.0	4.0e+04	107652
	11.	1.2	1.0	4.0e+04	107653
	2.9	1.2	1.0	4.2e+04	107654
	0.83	1.2	1.0	4.8e+04	107655
Alpgen Z+jets $\to \mu\mu$	6.7e+02	1.2	1.0	7.3e+03	107660
	1.3e+02	1.2	1.0	8.0e+03	107661
	40.	1.2	1.0	4.0e+04	107662
	11.	1.2	1.0	3.9e+04	107663
	2.7	1.2	1.0	4.4e+04	107664
	0.77	1.2	1.0	5.2e+04	107665
Alpgen Z+jets $\to \tau\tau$	6.7e+02	1.2	1.0	1.3e+04	107670
	1.3e+02	1.2	1.0	2.0e+04	107671
	40.	1.2	1.0	2.0e+04	107672
	11.	1.2	1.0	3.6e+04	107673
	2.8	1.2	1.0	4.2e+04	107674
	0.77	1.2	1.0	4.7e+04	107675
MC@NLO $t\bar{t}$	1.6e+02	1.0	0.56	3.2e+04	105200
AcerMC Single Top	6.9	1.0	1.0	1.2e+05	117360
	6.8	1.0	1.0	1.2e+05	117361
	7.3	1.0	1.0	1.2e+05	117362
	0.50	1.0	1.0	4.0e+05	117363
	0.50	1.0	1.0	4.0e+05	117364
	0.50	1.0	1.0	1.0e+06	117365
	16.	1.0	1.0	6.4e+04	105500
Herwig Diboson ($WW/WZ/ZZ$)	30.	1.5	0.39	1.4e+05	105985
	4.6	1.4	0.21	1.8e+05	105986
	3.4	1.6	1.0	1.9e+05	105987

Table 5.1: Cross section times branching ratio (times k-factor when applied), and filter efficiency for MC samples used in the inclusive W studies. The k-factor and filter efficiency are factors that bring the rates of the MC closer to the predicted cross section, while the sample tag is the ATLAS run number that is allocated for each MC sample.

Moreover, the muon originating from the W has to be "combined", i.e. include both a track in the inner detector, as well as an additional segment in the muon spectrometers, as defined in Section 4.4.1. Additional requirements on the muon originating from the W are chosen to discriminate against the multi-jet background, such as very tight isolation criteria. The muon originating from the W is required to be nearest the primary vertex, as its track has to be within 1 mm in the z-direction (proton beam direction), and the impact parameter significance has to be smaller than 3. The impact parameter is the distance in the x–y plane (transverse) from the interaction point, as defined in Section 4.1. The significance is defined as the ratio of the impact parameter value to its resolution, and can give a more accurate measure of the impact parameter, since it takes into account the resolution. The requirements associated with the W boson are summarized in Table 5.2.

W boson requirements	
muon requirements	
Fire and match trigger `EF_mu18_MG` or `EF_mu18_MG_medium`	
STACO combined	
Pass MCP cuts	
Transverse Momentum	$p_{\mathrm{T}} > 25$ GeV
Pseudorapidity	$\lvert\eta\rvert < 2.4$
Distance from primary vertex in z-direction	$\lvert z_0\rvert < 1$ mm
Impact parameter significance	$\lvert d_0\rvert < 3\sigma_{d_0}$
Track isolation momentum in cone of $\Delta R < 0.3$	$< 0.05 p_{\mathrm{T}}$
Calorimeter isolation energy in cone of $\Delta R < 0.3$	$< 0.05 p_{\mathrm{T}}$
Missing Transverse Energy	$E_{\mathrm{T}}^{\mathrm{miss}} > 20$ GeV
W Transverse Mass	$M_T(W) > 40$ GeV

Table 5.2: Requirements for W boson

The inclusive W production was observed in ATLAS with 33 pb^{-1} of data, as shown in Fig. 5.1, from [60]. The figure shows the transverse mass of the W boson for both the positively charged and negatively charged W boson decay to a muon and neutrino.

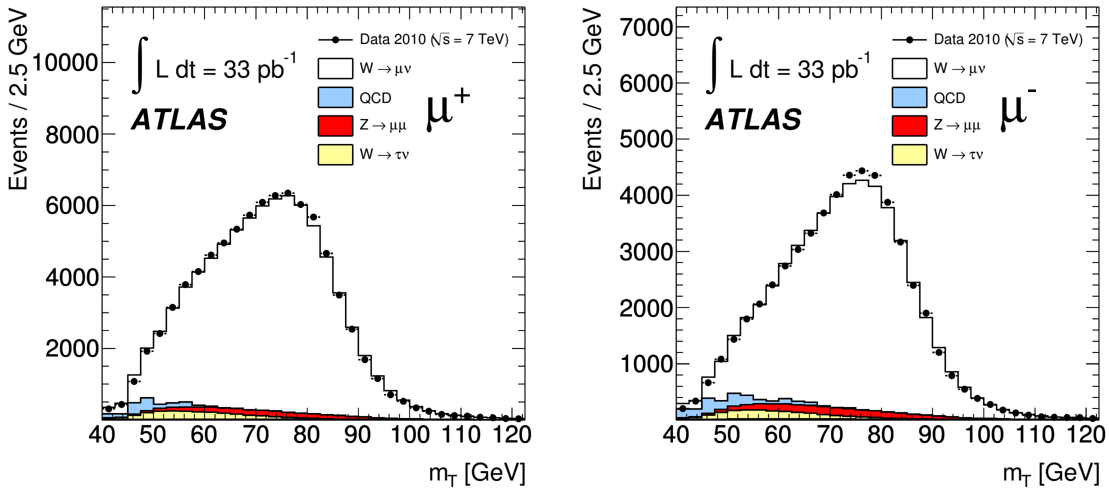

Figure 5.1: The W transverse mass distribution is shown for positvely and negatively charged W boson decays to a muon and neutrino for 33 pb^{-1} of data at ATLAS. The main backgrounds are multi–jet (QCD), the associated production of Z with jets, and the W decay to a tau and a neutrino.

Two additional muons whose invariant mass reconstructs the J/ψ mass are required for the J/ψ reconstruction. These muons have looser requirements than the muon originating from the W, and are required to be oppositely charged, as expected from the $J/\psi \rightarrow \mu^+\mu^-$ decay. The J/ψ muons can be either "combined" or "segment-tagged", which do not necessarily require a track in the muon spectrometer, to improve the efficiency for low-p_T, as defined in Section 4.4.1. The transverse momentum of J/ψ muons can be lower, down to 2.5 GeV for certain pseudorapidity regions, and the distance from the primary vertex in the z-direction can be up to 10 mm. The rapidity of the J/ψ is required to be $|y| < 2.1$ to ensure good acceptance of the J/ψ. The rapidity is used for the J/ψ, and the pseudorapidity for the muons, as explained in Section 4.1. An additional requirement is imposed on the invariant mass of the muon originating from the W and the oppositely charged J/ψ muon, to reject Z+jets background, as will be explained in Section 5.5.2. The requirements imposed because of the J/ψ are outlined in Table 5.3.

Following these requirements, events that are triggered and reconstruct one J/ψ candidate, in addition to a W candidate, are pre-selected for further analysis. The analysis separates prompt J/ψ production from non-prompt production by fitting the J/ψ pseudo-proper time, as will be explained in Chapter 6. The prompt J/ψ is chosen because it is a

J/ψ muon requirements	
STACO combined or segment-tagged	
pass MCP cuts	
Transverse Momentum	$p_{\mathrm{T}}>$ 2.5 GeV if $\lvert\eta\rvert > 1.3$
Transverse Momentum	$p_{\mathrm{T}}>$ 3.5 GeV if $\lvert\eta\rvert < 1.3$
Pseudorapidity	$\lvert\eta\rvert < 2.5$
Distance from primary vertex in z-direction	$\lvert z_0\rvert < 10$ mm
Dimuon requirements	
Oppositely charged muons	
At least one combined muon with $P_T > 4$ GeV	
Post-vertexing J/ψ Invariant Mass $\in (2.5, 3.5)$ GeV	
J/ψ transverse momentum $p_T \in (8.5, 30)$ GeV	
J/ψ rapidity $\lvert y\rvert \in (0, 2.1)$	
Invariant mass of "w muon" and oppositely charged "J/ψ muon" outside $(81, 101)$GeV	

Table 5.3: Requirements for J/ψ

result of direct J/ψ production, and not J/ψ produced from decays of long-lived particles, such as b-hadrons, as explained in Section 2.2.

The J/ψ pseudo-proper time is defined to separate prompt J/ψ from non-prompt decays, often associated with b-hadron decays [61]. Since we cannot fully reconstruct the b-hadron, we calculate

$$L_{xy} = \frac{\vec{L} \cdot \vec{p}_T^{J/\psi}}{p_T^{J/\psi}}, \tag{5.4}$$

where $\vec{L}$ is the vectorial distance between the primary vertex and J/ψ decay vertex. The probability for the decay of a b-hadron as a function of the proper decay time t follows an exponential decay distribution:

$$P(t) = \frac{1}{\tau_b}\exp(-\frac{t}{\tau_b}) \tag{5.5}$$

where τ_b is the lifetime of the b-hadron. The proper decay time for each decay can be calculated as:

$$t = \frac{L}{\beta\gamma} \tag{5.6}$$

where L is the distance between the b-hadron production and decay vertex, and $\beta\gamma$ is the Lorentz factor. Projecting the decay length and momentum on the transverse plane for b-hadrons, we obtain:

$$t = \frac{L_{xy} m_b}{p_{\mathrm{T}}^b} \tag{5.7}$$

where L_{xy} is the distance between the reconstructed secondary vertex and the primary vertex in the event. We then define the pseudoproper time, τ:

$$\tau = \frac{L_{xy} m_{J/\psi}^{\mathrm{PDG}}}{p_{\mathrm{T}}^{J/\psi}} \tag{5.8}$$

where $m_{J/\psi}^{\mathrm{PDG}}$ is the mass of the J/ψ.

Directly produced J/ψ mesons have $\tau = 0$ within the experimental resolution, while those produced from b decays tend to have vertices displaced from the primary vertex and to have positive τ which can be acceptably modeled by an exponential distribution. Negative pseudo-proper time values can arise due to resolution effects in the measurement of the distance L_{xy}, when a track decays at short distances and combines with another track that does not necessarily travel in the same direction.

Fig. 5.2 shows the mass and pseudo-proper time distributions for the inclusive J/ψ production [61], from 2.3 pb^{-1} of proton–proton collisions.

As has been shown, ATLAS has already observed the W boson and J/ψ meson separately. The associated production of W and J/ψ has not yet been observed, and the first search is reported in this thesis.

At the end of the selection, 149 events remain, which will be fit using the procedure explained in Chapter 6, to obtain the results in Chapters 7 and 8.

5.4 Efficiency determination

The ATLAS detector, as is often the case in particle physics experiments, is not perfect. Because of the construction and the shape of the detector, it is not possible to detect all

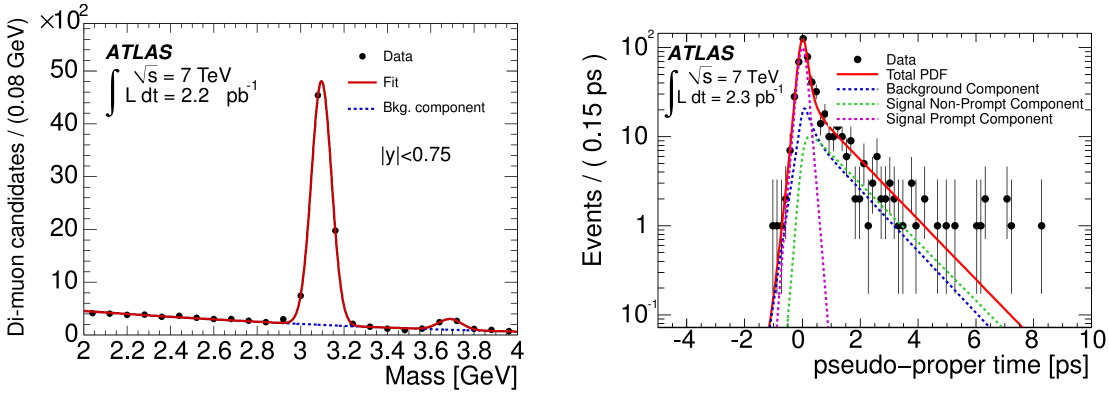

Figure 5.2: The dimuon invariant mass distribution for inclusive J/ψ production is shown (left), with a clear peak at the J/ψ mass, separating the J/ψ from combinatorial background. The pseudo-proper time distribution is shown (right), with the functional forms separating the prompt J/ψ component (Gaussian), from the non–prompt J/ψ component (exponential decay), and the combinatorial background (combination of Gaussian and exponential decay).

particles produced in proton–proton collisions in the interaction point at the center of the detector. In addition, even if a particle is produced in the geometrical space covered by the detector, it is possible that it is not sufficiently reconstructed or identified as the type of particle it is. For example, if a muon has too low transverse momentum, it will not be able to travel through the whole detector and leave hits in the muon detectors. With the few hits such a muon would leave in the inner detector, it is more challenging for ATLAS to reconstruct the track of the muon and identify that it is indeed a muon.

When a measurement of the cross section of a physics process is performed, it is necessary to evaluate the efficiency of the detection of the experimental signature, to extrapolate from the observed number of events of such process to the actual number of events that were produced in the proton–proton collisions.

For the measurement of the cross section ratio $W^{\pm}$ + prompt J/ψ:W, it is necessary to evaluate the efficiency of the detector to detect each of the J/ψ muons. The efficiency to detect the W boson is not needed, as it is a factor both in the numerator and denominator of the ratio expression. There are two types of J/ψ efficiency that need to be taken into account. First, the efficiency for the ATLAS detector to detect and reconstruct the two muons needs to be calculated, as it depends on the pseudorapidity and transverse momentum of each muon, as will be explained in Section 5.4.1. Secondly, the spin-alignment of the J/ψ, as will be explained in Section 5.4.2, is not known, but can be measured experimentally given enough statistics. Depending on the spin-alignment, the J/ψ can decay with the two muons traveling in different orientations, making them more, or less likely to be detected by the ATLAS detector. We have calculated both efficiencies, as described below.

5.4.1 Muon efficiencies

The muons used in this analysis include "segment-tagged" and "combined" muons with p_{T} below 4 GeV, which were not used for any other analysis in ATLAS.

The philosophy behind measuring the muon efficiencies relies on the "tag-and-probe" method (see for example [62]). Events are selected from triggers that fire on single muons, or muon and track pairs that fall in the J/ψ mass window. We use the J/ψ mass window, since we are interested in low-p_{T} muons, but the premise behind the method is similar in Z-boson "tag-and-probe" studies as well. A muon that satisfies a series of quality criteria, called a "tag muon", is required to be present in the event, and is combined with a track, called a "probe muon". The efficiency is then the number of "probe muons" that are also identified as "tag muons". In practice, we reconstruct the invariant mass of "tag-and-probe" pairs, and plot it in the range 2.5–4 GeV. We then fit the distributions with a Gaussian to represent the J/ψ and a polynomial to represent the background, as shown in Fig. 5.3. The number of J/ψ events is taken as the normalization constant of the Gaussian in the fit. Events where the "probe muon" also satisfies the "tag muon" requirements are also used to reconstruct the J/ψ invariant mass. The procedure is repeated for various bins in muon p_{T} and pseudorapidity to extract the efficiency for each bin, as it depends very strongly on the geometrical shape of the detector. The two-dimensional efficiency map, as well as the efficiencies as functions of p_{T} and pseudorapidity are shown in Fig. 5.3.

5.4.2 J/ψ acceptance

The spin of a particle is its intrinsic angular momentum (**S**), and when added to the orbital angular momentum (**L**), it gives rise to the total angular momentum, **J**=**L**+**S**. The total angular momentum (**J**) is a conserved quantity in physics. Spin-alignment arises from the alignment of the spin vector of the J/ψ and is difficult to determine experimentally (statistics-limited) and theoretically (current models do not describe the data correctly, both in cross sections and in spin-alignment).

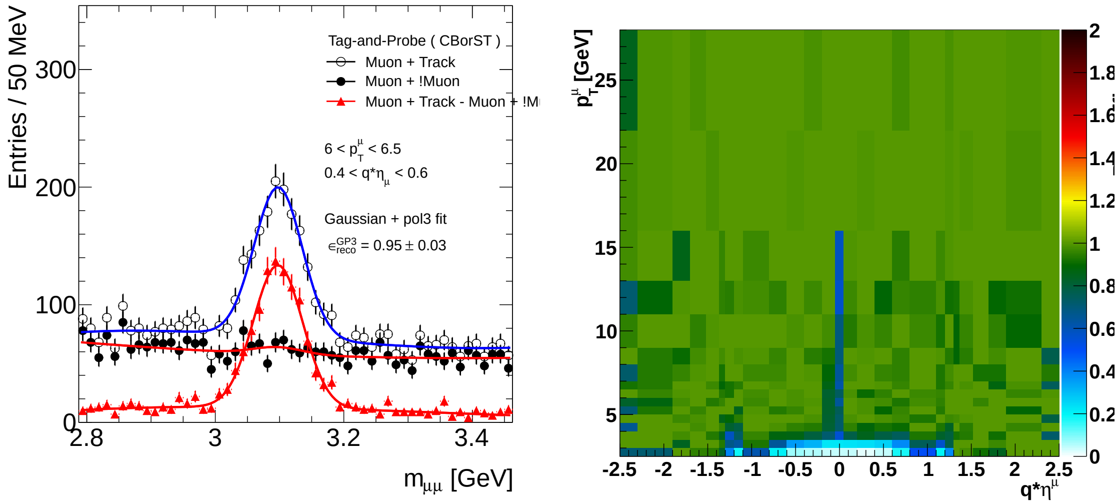

Figure 5.3: The fit performed in a specific η-p_{T} slice on pre-selected events to determine the muon reconstruction efficiency using the tag-and-probe method (left). The efficiency is the ratio of events that reconstruct the J/ψ mass, over the total number of events. The two-dimensional efficiency map in η and p_{T}, derived from data (right).

Generically, the fraction of J/ψ mesons produced in different spin-alignment states (the "spin-alignment profile") in different processes at the LHC is not known. Moreover, the spin-alignment profile can be quite different for inclusive prompt J/ψ processes and exclusive production processes such as $W^{\pm} + J/\psi$.

The procedure we followed to measure the corrections due to the acceptance of the J/ψ is explained here. With our muon selections, we simulate the probability that J/ψ candidates are able to be reconstructed as a function of the J/ψ p_{T} and rapidity. We vary the assumed spin-alignment profile of the J/ψ candidates and get acceptance maps for each scenario, as shown in Fig. 5.5. The angular distribution for the decay $J/\psi \to \mu\mu$ in the J/ψ decay frame is:

$$\frac{d^2N}{d\cos\theta^\star d\phi^\star} \propto 1 + \lambda_\theta \cos\theta^{\star 2} + \lambda_\phi \sin\theta^{\star 2}\cos 2\phi^\star + \lambda_{\theta\phi}\sin 2\theta^\star \cos\phi^\star, \tag{5.9}$$

where the angular variables are defined in Fig. 5.4. The terms λ_θ, λ_ϕ, and $\lambda_{\theta\phi}$ are the coefficients of each angular term, and can take values in $\in (0, 1)$. The extreme values of the λ coefficients cover the whole allowed phase space.

We quote the cross-section ratio for the envelope spanned by the following scenarios, as in [61]:

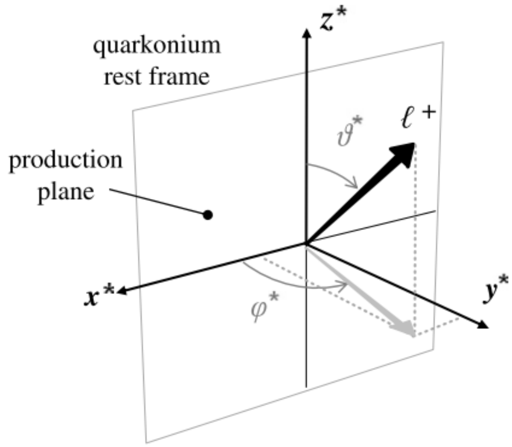

Figure 5.4: Definitions of the J/ψ spin-alignment angles, in the J/ψ decay frame. $\theta^\star$ is the angle between the direction of the positive muon momentum in the J/ψ decay frame and the J/ψ line of flight ($z^\star$-axis), while $\phi^\star$ is the angle between the J/ψ production plane ($x^\star - z^\star$) and the decay plane formed by the direction of the J/ψ and the positive muon (from [61])

1. Isotropic distribution, independent of $\theta^\star$ and $\phi^\star$, with $\lambda_\theta = \lambda_\phi = \lambda_{\theta\phi} = 0$. This is used for the nominal measurement.
2. Full longitudinal alignment with $\lambda_\theta = -1, \lambda_\phi = \lambda_{\theta\phi} = 0$
3. Transverse-0 alignment with $\lambda_\theta = +1, \lambda_\phi = \lambda_{\theta\phi} = 0$
4. Transverse-M alignment with $\lambda_\theta = +1, \lambda_\phi = -1, \lambda_{\theta\phi} = 0$
5. Transverse-P alignment with $\lambda_\theta = \lambda_\phi = +1, \lambda_{\theta\phi} = 0$

For each event, we apply a correction that is the inverse of the J/ψ acceptance, as shown in Eq. 5.2 in Section 5.1. We observe that the J/ψ acceptance falls to below 30% for events with J/ψ transverse momentum smaller than 8.5 GeV or absolute J/ψ rapidity larger than 2.1 (in some scenarios). Hence, we introduce a cut on the J/ψ transverse momentum $p_T > 8.5$ GeV and rapidity $|y| < 2.1$, in order to avoid outliers — events with extremely low acceptance and high inverse acceptance — which introduce large statistical uncertainties to our measurement. Since most of our events are on the low end of J/ψ p_{T}, we choose to focus on the $p_{\mathrm{T}} \in (8.5 - 30)$GeV region to measure the cross section ratio in this region.

In addition to the J/ψ spin-alignment not being known, the spin-alignment of J/ψ $+W$ can be quite different. This has an implication in the estimate of the double parton scattering

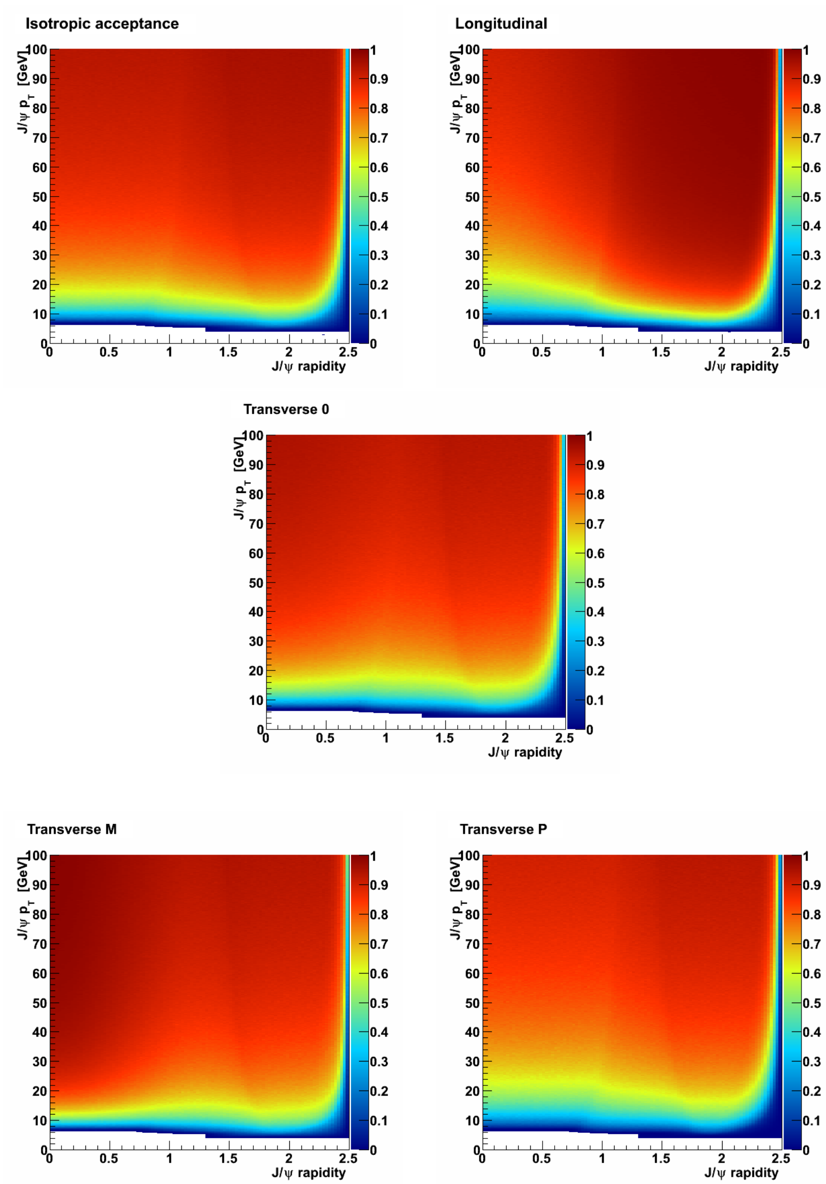

Figure 5.5: The J/ψ acceptance depends on the meson polarization. Since this is unknown, we simulate various polarization scenarios, and assume the unpolarized case as the baseline. Here, we show the acceptance maps for the unpolarized (left, up), longitudinal (up, right), transverse-0 (center), transverse-M (left, down) and transverse-P (right, down) cases.

contribution, which can change if the spin-alignment of J/ψ is correlated in inclusive J/ψ and J/ψ $+W$ events, as will be described in Sec. 5.6. We do not assume that the spin-alignment of J/ψ is the same for both processes, and introduce a systematic uncertainty due to the spin-alignment on the estimate of the double parton scattering contribution.

5.5 Background sources

Various sources of background have been considered for the $W^{\pm}$ + prompt J/ψ process. Background processes are processes that are detected using a similar experimental signature as our signal, and as such, they need to be taken into account when calculating the number of $W^{\pm}$+prompt J/ψ events. For example, the multi-jet background can give rise to a signature similar to a W boson, when a hadron is mis-identified as a muon. In addition, top–anti-top pairs and the associated production of Z with jets can produce similar signatures to the $W^{\pm} + J/\psi$ process, as well as $B_c^{\pm}$ decays. Pileup interactions at the LHC can allow for a W boson and a J/ψ meson to be produced in different proton–proton interactions. Some background sources predominantly produce non-prompt J/ψ, while others do not have a real J/ψ, falling in the combinatorial background category. Using the fit procedure, as will be described in Chapter 6, we can extract the prompt J/ψ component and differentiate it from the non-prompt J/ψ and combinatorial background. Pileup and multi-jet backgrounds are the only backgrounds that fall in the prompt J/ψ category.

5.5.1 Multi-jet background determination

Multijet background is mostly relevant in the cases where a muon produced from a hadronic decay due to Quantum Chromodynamic processes. This muon can mimic, or "fake", the muon from the W decay ($W \to \mu\nu$). When combined with a J/ψ, this is the same experimental signature as our signal process. To minimize the effect of this source of background, we have enforced strict isolation criteria on the muon that originates from the W decay, as explained in Section 5.3. In addition, to estimate the amount of the multi-jet background, we use a data-driven technique to extract a template distribution of the $M_T(W)$, defined in Eq. 5.3 in Section 5.3. This template will be used in a fit in conjuction with a template from W production, to estimate the amount of multi-jet background, as will be explained in Chapter 7.

The data-driven method is a refinement of the "ABCD" method, as explained below. We separate data in four regions, according to the missing transverse energy ($E_{\mathrm{T}}^{\mathrm{miss}}$) and W transverse mass ($M_T(W)$) of the event, and the isolation of the muon originating from the W, as follows:

A $E_{\mathrm{T}}^{\mathrm{miss}} < 20$ GeV and $M_T(W) < 40$ GeV and isolated muon
B $E_{\mathrm{T}}^{\mathrm{miss}} < 20$ GeV and $M_T(W) < 40$ GeV and anti-isolated muon
C $E_{\mathrm{T}}^{\mathrm{miss}} > 20$ GeV and $M_T(W) > 40$ GeV and isolated muon
D $E_{\mathrm{T}}^{\mathrm{miss}} > 20$ GeV and $M_T(W) > 40$ GeV and anti-isolated muon

The selections presented here are orthogonal to each other. An anti-isolated muon has the opposite isolation requirement than an isolated muon, as described in Section 5.3.

We assume that the ratio A/B gives a kinematic-independent "muon isolation fake factor", so $(A/B) \times D$ gives the multi-jet contamination of the signal region (C). This fake factor is calculated in muon transverse momentum bins of size 5 GeV in the range 0-200 GeV, to allow for the possibility that the factor depends on the kinematics of the muon. This procedure yields a template shape for the multi-jet contribution to be used to discriminate between real W events and multi-jet background.

Fig. 5.6 shows the multi-jet and W boson templates in the $M_T(W)$ distributions. The W boson templates were extracted from Monte Carlo simulation and validated in data. `ALPGEN` [63] was used to simulate the associated production of W and jets used for this template extraction, with the details shown in Table 5.1 in Section 5.2.

Since the multi-jet background mimics the W boson signature, it can fall in the prompt J/ψ background category. The amount of multi-jet background is negligible, since we use very strict isolation criteria, as will be shown in Chapter 7.

5.5.2 Z+jets production

Another possible source of background is the associated production of a Z boson with jets. In contrast to the muon originating from the W, the two J/ψ muons do not have strict isolation criteria, making it easier for an additional muon to be a jet-associated muon from Z+jets events. The Z boson can decay to two muons, of which one can be the muon originating from the W, and the other can be one of the "J/ψ muons" in our selections. When plotting the invariant mass of the muon originating from the W along with the oppositely charged

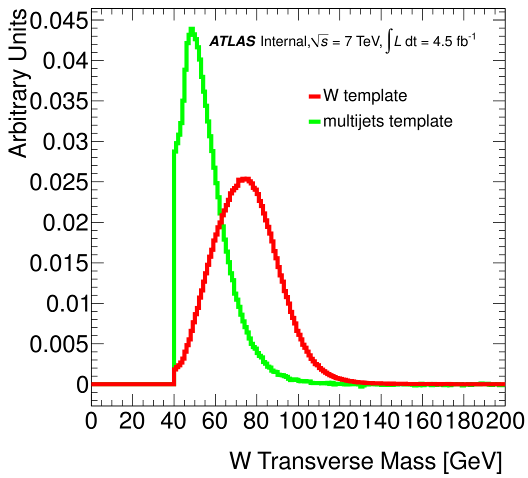

Figure 5.6: The template shapes of multi-jet and W boson in the $M_T(W)$ distribution are shown. The multi-jet template was obtained from data-driven methods, while the W template was obtained from simulation and validated in data.

"J/ψ muon" in a control region (dimuon mass outside J/ψ mass window, 3-3.2 GeV), the simulated Z+jets background clearly demonstrates the presence of a Z+jets component in the data, as seen in Fig. 5.7. `ALPGEN` [63] was used to simulate the associated production of Z and jets used for this template extraction, with the details shown in Table 5.1 in Section 5.2.

To reject the Z+jets background, an additional selection is applied to the invariant mass of the oppositely charged muon pair including the W muon, to exclude the region within 10 GeV of the mass of the Z boson $M_Z = 91.1876$ GeV. After the application of this selection, this background is found to be negligible.

5.5.3 $t\bar{t}$ production

The top quark decays almost exclusively to a W boson in association with a bottom quark. The W boson subsequently decays either leptonically or hadronically. Events with a leptonic decay tend to exhibit large missing transverse energy ($E_{\mathrm{T}}^{\mathrm{miss}}$). Subsequent decays of bottom quarks can produced final states with J/ψ. This results in $W^{\pm} + J/\psi$ signatures, that originate from $t\bar{t}$ production, Since the bottom quark is long-lived, the J/ψ produced from its decay tends to be non-prompt.

To confirm this, we performed a two-dimensional fit, as will be explained in Chapter 6, on

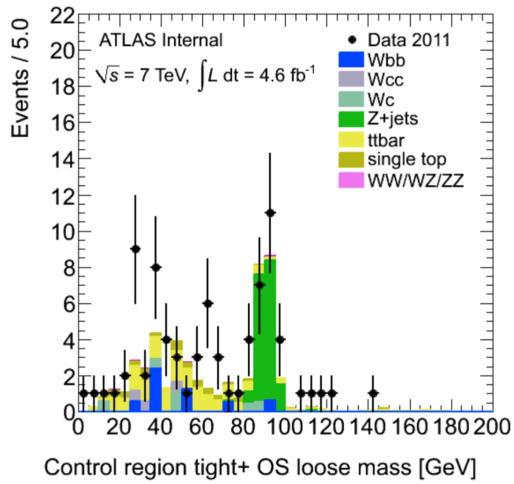

Figure 5.7: Combining the muon originating from the W decay with the oppositely charged "J/ψ muon" for $W^{\pm} + J/\psi$ candidates in the control region with J/ψ mass in 2.4–3 GeV or 3.2–3.6 GeV, yields a visible peak at M_Z. We reject events within 10 GeV of M_Z to reject Z+jets background.

the J/ψ mass and pseudo-proper time, in order to extract the amount of $t\bar{t}$ events that give a $W^{\pm}$ + prompt J/ψ component. The $t\bar{t}$ process was simulated using `MC@NLO` [64] generator, with the details shown in Table 5.1 in Section 5.2.

The fit results to a yield of -0.6 ± 4.1 $W^{\pm}$ + prompt J/ψ events, which is consistent with 0. This confirms the assumption that the $t\bar{t}$ process is a non-prompt background to the $W^{\pm} + J/\psi$ process.

5.5.4 $B_c^{\pm}$ decays

The $B_c^{\pm}$ meson can decay to J/ψ, a lepton and neutrino, mimicking the $W^{\pm} + J/\psi$ signature

$$B_c^{\pm} \rightarrow J/\psi \; l^{\pm}\nu X \tag{5.10}$$

where X can be any neutral particle. The branching ratio of this decay is low (5.2×10^{-5}), but the $B_c^{\pm}$ meson has a very short lifetime, compared to other B mesons, making the J/ψ look more prompt, like our signal. To determine if any B_c decays are included in the $W^{\pm} + J/\psi$ sample, we measure the invariant mass of the three muons $M(3\mu)$. The pre-selected events are weighted using `sPlot` [65] to get distributions for the $W^{\pm}$ + prompt J/ψ candidates.

We find no $W^{\pm} + J/\psi$ candidates having $M(3\mu)$ near the B_c mass of 6.277 ± 0.006 GeV, as shown in Fig. 5.8.

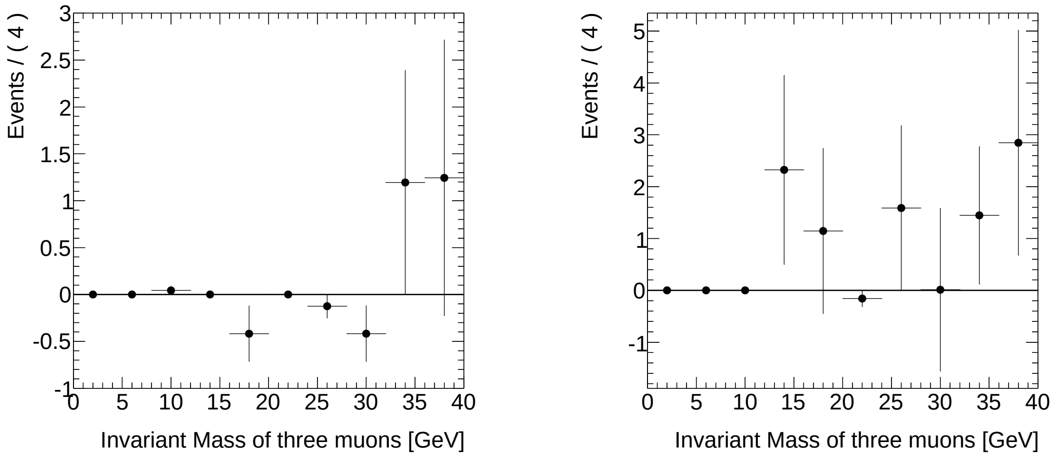

Figure 5.8: `sPlot`-weighted distribution for prompt J/ψ candidates, showing the invariant mass of the three muons $M(3\mu)$ for barrel (left) and endcap (right) in the range $M(3\mu) <$ 40GeV. There is no event with invariant mass near the B_c mass of 6.277 ± 0.006 GeV.

5.5.5 Pileup background

We are only interested in the $W^{\pm} + J/\psi$ candidates where the W boson and the J/ψ are produced in the same hard scatter. Since many pp interactions occur for each filled LHC bunch crossing, as explained in Chapter 3, it is possible for the W and the J/ψ to be produced in separate pp collisions which occur close to each other in the detector, also called pileup interactions.

We require that the muons from the J/ψ have $|z_0| < 10$ mm relative to the primary vertex. Thus, we effectively require that, for any real J/ψ candidates associated to a pileup vertex, the vertex is within 10 mm of the W vertex. As the beam spread σ_{z} for 2011 data was ≈ 5.5 cm, this already reduces the impact of pileup.

We use the following model to evaluate the background due to pileup. We obtain the luminosity-weighted distribution of $\langle\mu\rangle$, the mean number of collisions per bunch crossing, from the standard MC pileup reweighting mechanism. The values of μ we use in ATLAS for 7 TeV collisions assume an inelastic collision cross section of 71.5 mb [66]. We run a toy MC which samples the $\langle\mu\rangle$ distribution, throws a Poisson-distributed number of vertices, and then distributes them in z according to a Gaussian with width $\sigma_{\mathrm{Z}} = 55 \pm 5$ mm. One is randomly chosen as the primary vertex, and then the mean number of additional vertices within ± 10 mm is determined. The mean number of additional vertices is found to be 0.81 ± 0.08, with the uncertainty arising from assumed value of σ_{Z}.

These extra vertices have some probability of producing a J/ψ candidate with appropriate kinematics. For a $(|y|, p_{\mathrm{T}})$-bin i, we determine this probability (per extra vertex) to be

$$\frac{1}{\sigma_{\mathrm{inel}}} \int_{\mathrm{bin}\ i} \frac{d^2\sigma(pp \to J/\psi\ X)}{d|y|\ dp_{\mathrm{T}}} dy\ dp_{\mathrm{T}}$$

with $\sigma_{\mathrm{inel}} = 71.5$ mb. We take the inclusive J/ψ production cross sections from the ATLAS 7 TeV paper [61]. The expected pileup background levels are given in Table 5.4.

Pileup Background					
Bin $\|y\| \times p_{\mathrm{T}}$ (GeV)	σ(Prompt $J/\psi \rightarrow \mu\mu$) (nb)	$\sigma_{\mathrm{bin}}/\sigma_W$ (10^{-8})	$\frac{1}{\sigma_W}\frac{d^2\sigma}{dy\,dp_{\mathrm{T}}}$ (10^{-8})	$< \epsilon \times \mathcal{A} >$	Expected yield
$(0,1) \times (8.5,10)$	$6.34 \pm 0.23 \pm 0.84\ ^{+2.12}_{-1.71}$	$7.19 \pm 0.26 \pm 0.95\ ^{+2.41}_{-1.94} \pm 0.71$	$2.40 \pm 0.09 \pm 0.32\ ^{+0.80}_{-0.65} \pm 0.24$	0.27	0.30 ± 0.03
$(1,2.1) \times (8.5,10)$	$6.14 \pm 0.15 \pm 0.68\ ^{+1.65}_{-1.17}$	$6.96 \pm 0.17 \pm 0.77\ ^{+1.87}_{-1.33} \pm 0.69$	$2.11 \pm 0.05 \pm 0.23\ ^{+0.57}_{-0.40} \pm 0.21$	0.42	0.46 ± 0.05
$(0,1) \times (10,14)$	$4.85 \pm 0.10 \pm 0.55\ ^{+1.22}_{-1.28}$	$5.49 \pm 0.11 \pm 0.62\ ^{+1.38}_{-1.45} \pm 0.54$	$0.69 \pm 0.01 \pm 0.08\ ^{+0.17}_{-0.18} \pm 0.07$	0.43	0.37 ± 0.04
$(1,2.1) \times (10,14)$	$4.59 \pm 0.08 \pm 0.52\ ^{+0.94}_{-0.92}$	$5.20 \pm 0.09 \pm 0.59\ ^{+1.06}_{-1.05} \pm 0.51$	$0.59 \pm 0.01 \pm 0.07\ ^{+0.12}_{-0.12} \pm 0.06$	0.55	0.44 ± 0.04
$(0,1) \times (14,18)$	$0.93 \pm 0.04 \pm 0.10\ ^{+0.19}_{-0.22}$	$1.06 \pm 0.04 \pm 0.11\ ^{+0.21}_{-0.25} \pm 0.10$	$0.13 \pm 0.01 \pm 0.01\ ^{+0.03}_{-0.03} \pm 0.01$	0.56	0.09 ± 0.01
$(1,2.1) \times (14,18)$	$0.82 \pm 0.03 \pm 0.09\ ^{+0.12}_{-0.15}$	$0.93 \pm 0.03 \pm 0.10\ ^{+0.14}_{-0.17} \pm 0.09$	$0.11 \pm 0.00 \pm 0.01\ ^{+0.02}_{-0.02} \pm 0.01$	0.65	0.09 ± 0.01
$(0,1) \times (18,30)$	$0.39 \pm 0.02 \pm 0.04\ ^{+0.06}_{-0.08}$	$0.44 \pm 0.02 \pm 0.05\ ^{+0.07}_{-0.09} \pm 0.04$	$0.02 \pm 0.00 \pm 0.00\ ^{+0.00}_{-0.00} \pm 0.00$	0.67	0.05 ± 0.00
$(1,2.1) \times (18,30)$	$0.33 \pm 0.02 \pm 0.03\ ^{+0.04}_{-0.05}$	$0.37 \pm 0.02 \pm 0.04\ ^{+0.04}_{-0.06} \pm 0.04$	$0.01 \pm 0.00 \pm 0.00\ ^{+0.00}_{-0.00} \pm 0.00$	0.71	0.04 ± 0.00

Table 5.4: Expected background contributions from overlapping pileup events. The first column shows the bin in $|y| \times p_{\mathrm{T}}$ space of the J/ψ. The second column is the computed prompt inclusive J/ψ cross section in this kinematic bin, evaluated from the published 7 TeV ATLAS data [66]. The first uncertainty is statistical, the second systematic, and the third is the spin-alignment uncertainty. The third column shows the predicted ratio of efficiency- and acceptance-corrected $W^{\pm} + J/\psi$ events from this source to the inclusive W cross section. The first three uncertainties are statistical, systematic, and spin-alignment. The fourth uncertainty is due to σ_{Z}. The fourth column shows the values of the third column normalized by the size of the bin in $|y| \times p_{\mathrm{T}}$ space, i.e. these are the corrections to $R_{J/\psi}$ to be subtracted from the observed rates. The fifth column shows the average acceptance $\times$ efficiency from inclusive J/ψ in each bin, which is used to estimate the number of pileup events in our sample. The sixth column shows the expected yield of pileup events.

Applying the average efficiencies in each $|y| \times p_{\mathrm{T}}$ bin, we expect a total rate of *reconstructed* overlapping events of $\approx 15.1 \times 10^{-8}$ per inclusive W. Multiplying by the number of W candidates, 1.5×10^7, and taking into account the average efficiency from the inclusive J/ψ for each bin, we estimate an expected 1.8 ± 0.2 reconstructed events arising from pileup in our whole sample. We investigate the difference between the distance from the primary vertex in the z–direction of the muon originating from the W and the average distance from the primary vertex in the z–direction of the muons forming the J/ψ candidate for the prompt $W^{\pm} + J/\psi$ candidates. All events have a difference < 1 mm, except for one outlier with `sPlot` weight of 1.7 for $W^{\pm}$+prompt J/ψ. This is quite consistent with our a priori estimate.

5.6 Multiple parton scattering

It is possible for multiple hard processes to occur in a single *pp* collision; if there are two interactions the situation is called double parton scattering (DPS). DPS production is indistinguishable from the single parton scattering (SPS) process with low number of events. The SPS production is the $W^{\pm} + J/\psi$ production that is predicted by the theories described in Sec. 2.3. The kinematic distribution of the opening angle between the W and J/ψ in SPS $W^{\pm} + J/\psi$ events is expected to peak at π, since the W and J/ψ are produced in the same parton–parton interaction and conservation of energy holds. The DPS kinematic distribution is expected to be flat, since the W and J/ψ are produced in different parton–parton interactions. Fig. 5.9 shows the expected distributions with the DPS simulated from `PYTHIA` [67] and SPS simulated using `MadGraph` [68]. Since DPS process is indistinguishable from the SPS process, we observe both contributions, and estimate the amount of the DPS contribution a priori, in order to calculate the amount of SPS to compare with the theoretical predictions, as will be shown in Chapter 8.

For a collision in which hard process A occurs, the probability that an additional (distinguishable) process B occurs is parametrized as

$$P_B = \frac{\sigma_B}{\sigma_{\mathrm{eff}}}$$

where σ_{eff} is a parameter we take to be $15 \pm 3(\mathrm{stat.})^{+5}_{-3}(\mathrm{syst.})$ mb from the ATLAS measurement of hard double-parton scattering interactions in $W \to l\nu + 2$ jet events [69–71].

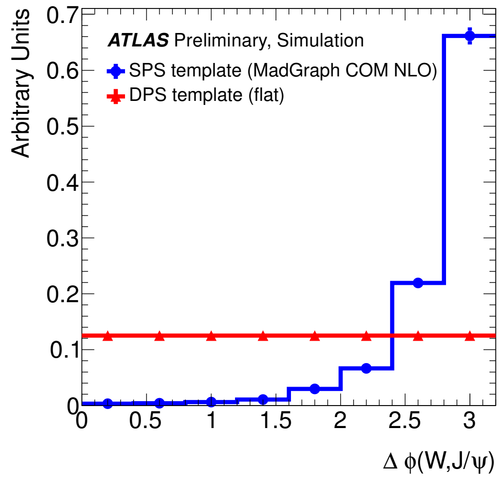

Figure 5.9: The azimuthal angle separation between the W boson and the J/ψ meson in single parton scattering (SPS) and double parton scattering (DPS) production as estimated from simulation. The DPS template is assumed flat, and was validated with `PYTHIA`, while the SPS template was simulated with specific phenomenological assumptions in `MadGraph`.

This has exactly the same form as the pileup term considered in Sec. 5.5.5 (i.e. a probability per W event, given by the J/ψ cross section divided by another cross section). Because σ_{eff} is much smaller than σ_{inel}, the DPS background is actually significantly higher ($4.8\times$) than the pileup background. The expected DPS production rates are shown in Table 5.5. Multiplying by the number of W candidates, 1.5×10^7, and taking into account the average efficiency from inclusive J/ψ for each bin, the total number of DPS production in our sample is expected to be 10.8 ± 4.2 events.

Double Parton Scattering contribution					
Bin $\|y\| \times p_{\mathrm{T}}$ (GeV)	$\sigma(\text{Prompt } J/\psi \to \mu\mu)$ (nb)	$\sigma_{\text{bin}}/\sigma_W$ (10^{-8})	$\frac{1}{\sigma_W}\frac{d^2\sigma}{dy\, dp_{\mathrm{T}}}$ (10^{-8})	$< \epsilon \times \mathcal{A} >$	Expected yield
$(0,1) \times (8.5,10)$	$6.34 \pm 0.23 \pm 0.84\ ^{+2.12}_{-1.71}$	$42.28 \pm 1.55 \pm 5.62\ ^{+14.17}_{-11.42} \pm 16.43$	$14.09 \pm 0.52 \pm 1.87\ ^{+4.72}_{-3.81} \pm 5.48$	0.27	1.74 ± 0.68
$(1,2.1) \times (8.5,10)$	$6.14 \pm 0.15 \pm 0.68\ ^{+1.65}_{-1.17}$	$40.94 \pm 0.97 \pm 4.52\ ^{+11.02}_{-7.81} \pm 15.91$	$12.41 \pm 0.29 \pm 1.37\ ^{+3.34}_{-2.37} \pm 4.82$	0.42	2.69 ± 1.05
$(0,1) \times (10,14)$	$4.85 \pm 0.10 \pm 0.55\ ^{+1.22}_{-1.28}$	$32.33 \pm 0.64 \pm 3.63\ ^{+8.13}_{-8.53} \pm 12.57$	$4.04 \pm 0.08 \pm 0.45\ ^{+1.02}_{-1.07} \pm 1.57$	0.43	2.17 ± 0.84
$(1,2.1) \times (10,14)$	$4.59 \pm 0.08 \pm 0.52\ ^{+0.94}_{-0.92}$	$30.60 \pm 0.52 \pm 3.48\ ^{+6.24}_{-6.16} \pm 11.89$	$3.48 \pm 0.06 \pm 0.40\ ^{+0.71}_{-0.70} \pm 1.35$	0.55	2.61 ± 1.01
$(0,1) \times (14,18)$	$0.93 \pm 0.04 \pm 0.10\ ^{+0.19}_{-0.22}$	$6.21 \pm 0.24 \pm 0.63\ ^{+1.24}_{-1.49} \pm 2.41$	$0.78 \pm 0.03 \pm 0.08\ ^{+0.15}_{-0.19} \pm 0.30$	0.56	0.54 ± 0.21
$(1,2.1) \times (14,18)$	$0.82 \pm 0.03 \pm 0.09\ ^{+0.12}_{-0.15}$	$5.45 \pm 0.18 \pm 0.60\ ^{+0.80}_{-0.98} \pm 2.12$	$0.62 \pm 0.02 \pm 0.07\ ^{+0.09}_{-0.11} \pm 0.24$	0.65	0.55 ± 0.21
$(0,1) \times (18,30)$	$0.39 \pm 0.02 \pm 0.04\ ^{+0.06}_{-0.08}$	$2.59 \pm 0.14 \pm 0.29\ ^{+0.39}_{-0.53} \pm 1.01$	$0.11 \pm 0.01 \pm 0.01\ ^{+0.02}_{-0.02} \pm 0.04$	0.67	0.27 ± 0.11
$(1,2.1) \times (18,30)$	$0.33 \pm 0.02 \pm 0.03\ ^{+0.04}_{-0.05}$	$2.18 \pm 0.11 \pm 0.22\ ^{+0.26}_{-0.34} \pm 0.85$	$0.08 \pm 0.00 \pm 0.01\ ^{+0.01}_{-0.01} \pm 0.03$	0.71	0.24 ± 0.09

Table 5.5: Expected contributions from double parton scattering (DPS) events. The first column shows the bin in $|y| \times p_{\mathrm{T}}$ space of the J/ψ. The second column is the computed prompt inclusive J/ψ cross section in this kinematic bin, evaluated from the published 7 TeV ATLAS data [66]. The first uncertainty is statistical, the second systematic, and the third is the spin-alignment uncertainty. The third column shows the predicted ratio of efficiency- and acceptance-corrected $W^{\pm} + J/\psi$ events from this source to the inclusive W cross section. The first three uncertainties are statistical, systematic, and spin-alignment. The fourth uncertainty is due to σ_{eff}. The fourth column shows the values of the third column normalized by the size of the bin in $|y| \times p_{\mathrm{T}}$ space, i.e. these are the corrections to $R_{J/\psi}$ to be subtracted from the observed rates. The fifth column shows the average acceptance $\times$ efficiency from inclusive J/ψ in each bin, which is used to estimate the number of DPS events in our sample. The sixth column shows the expected yield of DPS events.

Chapter 6
Fit Procedure

Alguien va en un entierro sollozando
¿Cómo luego ingresar a la Academia?

– Cesar Vallejo, *Un hombre pasa con un pan al hombro*

We use a fit procedure to extract the $W^{\pm}$ + prompt J/ψ signal from the dataset. The statistical significance of the observation of the $W^{\pm}$+prompt J/ψ process is calculated using the likelihood ratio method. Systematic uncertainties introduced due to the fit procedure are calculated and several cross-checks on the fit procedure are shown in this Chapter.

6.1 Signal extraction

The number of $W^{\pm}$ +prompt J/ψ candidates is extracted using a two-dimensional fit in the dimuon invariant mass and pseudo-proper time distributions. This allows for the separation of combinatorial and non-prompt background from the prompt J/ψ component. The J/ψ pseudo-proper time distribution is expected to peak at 0 for prompt J/ψ, while resolution effects allow for smearing of this distribution. The non-prompt background is expected to follow an exponentially falling distribution, as shown in Fig. 5.2 in Section 5.3. The following functional forms were used for the fits on the pseudo-proper time distributions:

$$\begin{aligned}
T_{\text{prompt } J/\psi}(\tau) &= G(\tau;0,\sigma_T)\otimes\left((1-a)\delta(\tau)+aC_0\mathrm{e}^{-|\tau|/\tau_0}\right)\\
T_{\text{non-prompt } J/\psi}(\tau) &= G(\tau;0,\sigma_T)\otimes\left(C_1\theta(\tau)\mathrm{e}^{-\tau/\tau_1}\right)\\
T_{\text{prompt bkg}}(\tau) &= G(\tau;0,\sigma_T)\otimes\left((1-b)\delta(\tau)+bC_4\mathrm{e}^{-|\tau|/\tau_0}\right)\\
T_{\text{non-prompt bkg}}(\tau) &= G(\tau;0,\sigma_T)\otimes\left(C_5\theta(\tau)\mathrm{e}^{-\tau/\tau_2}\right).
\end{aligned}$$

In the above, $G(x;\mu,\sigma)$ is a Gaussian function of x with mean μ and width σ; δ is the Dirac delta function; θ is the step function; a, b, and the τ_i are shape parameters; and the C_i are appropriate normalization constants.

The dimuon invariant mass distribution exhibits a Gaussian peak at the J/ψ mass for the J/ψ signal, and a combinatorial background on both sides of the J/ψ mass peak. The resolution of the Gaussian depends on the region of the detector where the J/ψ is detected. J/ψ candidates near the barrel region have better resolution, while those in the endcap region exhibit slightly worse resolution. To take advantage of the different resolution, we separate the fit in two regions, barrel and endcap, defined by the rapidity (y) of the J/ψ, $0 < J/\psi\ y < 1$ and $1 < J/\psi\ y < 2.1$, respectively. The following functional forms were used for the fits on the mass distributions:

$$\begin{aligned}
M_{J/\psi}(m_{\mu^+\mu^-}) &= G(m_{\mu^+\mu^-}; m_{J/\psi}^{\mathrm{PDG}}, \sigma_m) \\
M_{\text{prompt bkg}}(m_{\mu^+\mu^-}) &= C_2 \mathrm{e}^{-m_{\mu^+\mu^-}/k_0} \\
M_{\text{non-prompt bkg}}(m_{\mu^+\mu^-}) &= C_3 \mathrm{e}^{-m_{\mu^+\mu^-}/k_1}
\end{aligned}$$

In the above, $G(x; \mu, \sigma)$ is a Gaussian function of x with mean μ and width σ, the k_i are shape parameters; and the C_i are appropriate normalization constants.

The combined probability density function used for the fit is:

$$\begin{aligned}
p \propto\ & N_{\text{prompt } J/\psi} \times M_{J/\psi}(m_{\mu^+\mu^-}) \times T_{\text{prompt } J/\psi}(\tau) \\
+\ & N_{\text{non-prompt } J/\psi} \times M_{J/\psi}(m_{\mu^+\mu^-}) \times T_{\text{non-prompt } J/\psi}(\tau) \\
+\ & N_{\text{prompt bkg}} \times M_{\text{prompt bkg}}(m_{\mu^+\mu^-}) \times T_{\text{prompt bkg}}(\tau) \\
+\ & N_{\text{non-prompt bkg}} \times M_{\text{non-prompt bkg}}(m_{\mu^+\mu^-}) \times T_{\text{non-prompt bkg}}(\tau).
\end{aligned}$$

The functional forms and the values of the nuisance parameters used for the fits were derived using a combination of data-driven techniques and Monte Carlo simulated samples. Nuisance parameters are the parameters that define the shapes the functional forms will take in a fit, and are determined using inclusive J/ψ fits in the two regions. This is because the inclusive J/ψ fits have enough statistics to offer a more reliable measure of the nuisance parameters. In contrast, the pre-selected events for the $W^{\pm} + J/\psi$ analysis are too few to be able to constrain the nuisance parameters using a two-dimensional fit procedure. We allow for the possibility that the nuisance parameters are different between the inclusive J/ψ fit and the $W^{\pm} + J/\psi$ fit, by allowing the nuisance parameters to float with a Gaussian constraint equal to the uncertainty of the parameters from the inclusive fit. The following nuisance parameters are allowed to float: σ_m, σ_τ, τ_0,τ_1, τ_2, k_0, k_1, and the fractions a, b, while the mean values of the Gaussian functions in mass and pseudo-proper time are kept constant at the J/ψ mass and 0 respectively.

We use the Roofit statistical toolkit [72] for the implementation of our fits, which normalizes the probability density functions to unity. Roofit is a collection of standardized tools in particle physics that performs fits to datasets according to user-defined functional forms, in order to extract the nuisance parameters, or the yield of certain physics processes, modelled by each functional form.

We use the `sPlot` procedure [65] to extract weights for the prompt J/ψ hypothesis for all the events. Every event is assigned a weight for the prompt J/ψ, non-prompt J/ψ, and combinatoric background hypotheses. This allows us to determine the distributions of signal-like events in other variables. In particular, we plot the W transverse mass distribution for the prompt J/ψ component as determined by `sPlot`. We fit this distribution with the inclusive W shape from Monte Carlo simulation and the data-driven multi-jet shape to determine which hypothesis — W-only or multi-jet-only — better models the `sPlot` weighted distribution, using the χ^2 test. To determine the yields of $W^{\pm}$ + prompt J/ψ and multi-jet+prompt J/ψ from the fit we perform a fit on the W transverse mass including the W and multi-jet templates simultaneously and find the ratio of the models that minimizes the χ^2 value.

In order to determine the cross-section ratio, we apply an event-by-event correction for each $W^{\pm}$ + prompt J/ψ candidate given by the efficiency of reconstructing the J/ψ muons and the acceptance of reconstructing the J/ψ in the ATLAS detector. We use the maps of soft muon reconstruction efficiencies ϵ and J/ψ acceptance $\mathcal{A}$, as described in Section 5.4. We report the differential cross-section ratio $R_{J/\psi}$ in bins in J/ψ rapidity $|y|$, $(0, 1)$ and $(1, 2.1)$, and J/ψ transverse momentum p_T, $(8.5-10), (10-14), (14, 18)$ and $(18-30)$ GeV. Moreover, the branching ratio of the $J/\psi \to \mu\mu$ decay (5.98%) is implied in the results, to correct for the fact that we are only considering this decay channel of the J/ψ.

The measurement of the cross-section ratio strongly depends on the assumed spin-alignment scenario. We report the ratio with isotropic scenario assumption as our base measurement. In addition, we report the ratio measurement for the different scenarios.

For the ratio measurement, we assume all the prompt J/ψ candidates are associated with a W boson. The results in Chapter 7 show that the W-only hypothesis is strongly preferred, and that the amount of multi-jet background in consistent with 0.

6.2 Significance calculation

In particle physics, we define the p-value as a measure of the statistical significance of a physics process. The p-value is the probability that the background-only hypothesis (also known as null hypothesis) fluctuates to at least the number of signal events that were observed in the data. The statistical significance is obtained from the p-value by converting it to a "σ–level", or the number of standard deviations away from the mean of a normal distributions. The standard for observation of "new physics" in particle physics is 5σ. For a detailed treatise of statistical methods, see for example [73, 74].

To calculate the statistical significance of the $W^{\pm}$ + prompt J/ψ process, we use the likelihood ratio method. The likelihood ratio $\Delta(-2\ln\mathcal{L})$ between the best fit hypothesis (with a floating prompt J/ψ yield) and the null hypothesis (prompt J/ψ yield forced to zero) for the data, is compared with thousands of pseudoexperiments to generate the p-value, which is used to estimate the significance for prompt J/ψ production. After establishing the observation of prompt J/ψ, we fit the `sPlot`-weighted prompt J/ψ candidates in the W transverse mass distribution to separate the real W boson process from multi-jet background. We repeat the fit with the null hypothesis, assuming no W exists in association with the prompt J/ψ candidates. The significance of the W production, as opposed to multi-jet, in association with J/ψ is found using the $\Delta\chi^2$ between the two hypotheses. The results of applying this procedure will be described in Chapter 7.

6.3 Fit systematic uncertainties

Systematic uncertainties may be introduced due to our choice of fit functions. We try different functional forms, such as removing the double-sided exponential tails, changing the exponential in combinatorics mass distributions to Chebychev polynomials, using the same exponents for signal and background in pseudo-proper time, using the same exponents for prompt and non-prompt combinatorics in mass, using asymmetric double-sided exponential tails, and others, and find the maximum effect on the yields to be 4%. We attribute this as a systematic due to our choice of the fit functional forms. We allow the fit nuisance parameters to float with a Gaussian constraint equal to the error from the inclusive J/ψ fit. We estimate the uncertainty due to the fit procedure by repeating the two-dimensional fit by allowing a Gaussian constraint on each of the nuisance parameters equal to the error from the inclusive J/ψ fit, and comparing the errors on the yields with the errors on the yields when we keep the nuisance parameters constant at the fitted values. Keeping the nuisance parameters constant allows us to separate the statistical error from the total, statistical and systematic, error that is derived from the fit.

The systematic uncertainty due to the fit procedure is $^{+2.8}_{-1.8}\%$ in the barrel and $^{+1.5}_{-1.4}\%$ in the endcap. Applying the Gaussian constraint on the nuisance parameters from the inclusive parameter reduces the systematic uncertainty due to the fit, since it is derived from a well understood inclusive J/ψ fit, and takes into account the correlations between the nuisance parameters. When we allow the nuisance parameters to float with a Gaussian constraint equal to five times the error from the inclusive J/ψ fit, the results are comparable.

In addition, the fit systematic uncertainty in the significance calculation is taken into account when we allow the nuisance parameters to float in the final fit with the Gaussian constraints on the nuisance parameters of 1 σ from the inclusive fits, compared to keeping the nuisance parameters constant at their fitted values. The profile likelihood of the yield of $W^{\pm}$ + prompt J/ψ is shown in Fig. 6.1 for the two cases. We report the results of the fit when the nuisance parameters are allowed to float with a Gaussian constraint of 1 σ, to include the systematic uncertainties.

Table 6.1 shows the nuisance parameters of the inclusive J/ψ fit and the $W^{\pm} + J/\psi$ fitted values after we apply Gaussian constraints on the nuisance parameters with the error from the inclusive fit.

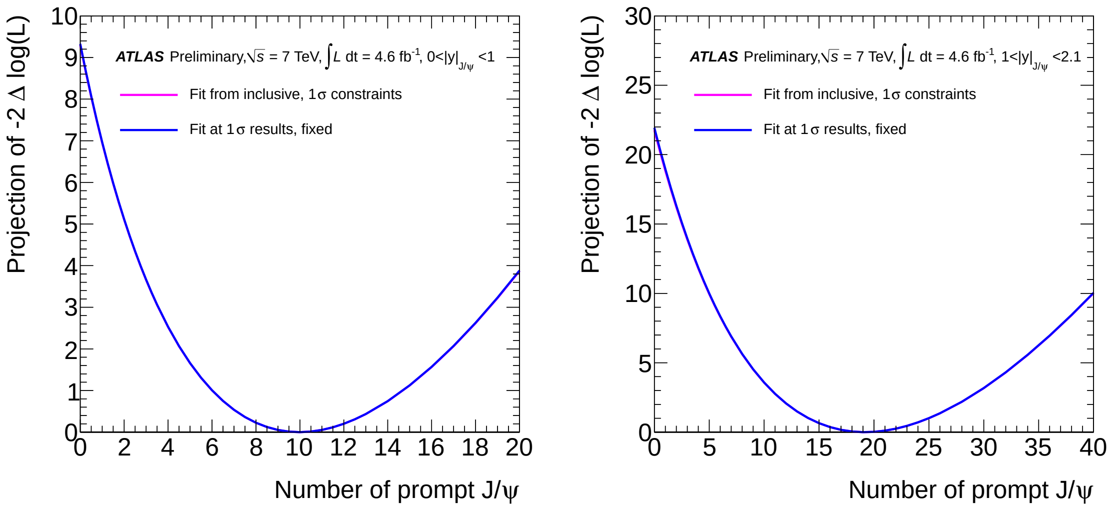

Figure 6.1: The profile likelihood ratio for the $W^{\pm}$ + prompt J/ψ yield is shown for the cases where the nuisance parameters are allowed to float with a Gaussian constraint on the nuisance parameters of 1σ of the parameters from the inclusive J/ψ fit (magenta), compared with keeping the nuisance parameters fixed at their fitted values (blue). The difference in the errors corresponds to the systematic uncertainty due to the fit procedure.

Fit nuisance parameter values and yields				
	J/ψ inclusive fit		$W^{\pm} + J/\psi$ fit using 1 σ constraint	
Parameter	Barrel	Endcap	Barrel	Endcap
μ_m	3.097	3.097	3.097	3.097
σ_m	0.0393 ± 0.0005	0.0701 ± 0.0008	0.0393 ± 0.0005	0.0700 ± 0.0008
μ_τ	0	0	0	0
σ_τ	0.0744 ± 0.0020	0.0929 ± 0.0022	0.0745 ± 0.0020	0.0933 ± 0.0022
τ_0	1.22 ± 0.03	1.14 ± 0.03	1.22 ± 0.03	1.14 ± 0.03
τ_{eff1}	1.29 ± 0.04	1.23 ± 0.04	1.29 ± 0.04	1.24 ± 0.04
τ_{eff2}	0.228 ± 0.013	0.205 ± 0.015	0.233 ± 0.013	0.212 ± 0.014
m_{eff1}	1.46 ± 0.10	1.08 ± 0.11	1.48 ± 0.10	1.11 ± 0.11
m_{eff2}	0.19 ± 0.13	-0.03 ± 0.16	0.21 ± 0.13	0.04 ± 0.15
Fraction of Double-sided in prompt J/ψ a_1	0.181 ± 0.022	0.118 ± 0.023	0.183 ± 0.022	0.119 ± 0.023
Fraction of Double-sided in prompt combinatorics b_1	0.724 ± 0.045	0.772 ± 0.070	0.732 ± 0.044	0.782 ± 0.069

Table 6.1: The values of the nuisance parameters of the fit with their uncertainties from the inclusive J/ψ fit, and the results of the fit using the errors from the inclusive fit as constraints on the nuisance parameters for the $W^{\pm} + J/\psi$ fit. We observe that the central values and the uncertainties of the nuisance parameters are comparable between the inclusive J/ψ and $W^{\pm} + J/\psi$ fits. The constraints are important to add information from the better understood inclusive J/ψ fit and this added information is not contradicted by the $W^{\pm} + J/\psi$ data.

The nuisance parameters of the fit were extracted from the inclusive J/ψ fit in the J/ψ transverse momentum range 8.5–30GeV, the same range used for the $W^\pm + J/\psi$. The J/ψ transverse momentum distribution is different between the inclusive J/ψ and the $W^\pm +$ prompt J/ψ. We estimated the effect of this discrepancy in the yields by fitting the inclusive J/ψ transverse momentum subregions 8.5–10, 10–14 and 14–30 GeV separately, first with no constraints on the fit, and then using the 8.5–30 GeV nuisance parameters with constraints, as done for the $W^\pm$+J/ψ fit. The prompt J/ψ yields for both fits are shown in Table 6.2. The results show that using a different J/ψ transverse momentum range for the extraction of the fit nuisance parameters has a small effect, less than 1%, on the prompt J/ψ yields, compared to leaving the inclusive J/ψ fit unconstrained and extracting the yields independently for each region. We assign a systematic uncertainty associated with this effect, to account for the assumption that the fit nuisance parameters extracted from the inclusive J/ψ distribution can be used as a template for the $W^\pm + J/\psi$ distribution, which might follow a different J/ψ transverse momentum distribution than the inclusive J/ψ.

Prompt J/ψ yields in inclusive J/ψ fits				
$(\lvert y\rvert \times p_T)$ bin	Unconstrained prompt J/ψ	Constrained prompt J/ψ	Absolute difference	Percentage difference
$(0,1) \times (8.5,10)$	4373±79	4413±77	40	1%
$(1,2.1) \times (8.5,10)$	4755±86	4693±83	-62	−1%
$(0,1) \times (10,14)$	4400±78	4400±76	0	0%
$(1,2.1) \times (10,14)$	4646±82	4620±80	-26	−1%
$(0,1) \times (14,30)$	3907±73	3898±72	-9	−0%
$(1,2.1) \times (14,30)$	4031±76	4065±75	34	1%

Table 6.2: The prompt J/ψ yields in inclusive fits in three subregions in J/ψ transverse momentum and two regions in rapidity are shown for unconstrained fits in the second column. The third column shows the prompt J/ψ yields for constrained fits, using the nuisance parameters from the fit in the whole J/ψ transverse momentum range, 8.5–30 GeV, with Gaussian constraints. The absolute and percentage difference of constrained-unconstrained yields is also shown. The differences are less than 1%.

6.4 Cross-checks

We performed various cross-checks to confirm that our fit procedure is robust and stable, without biases being introduced due to the choice of nuisance parameters or fit functional forms. Specifically, we calculated the pull distributions for thousands of pseudoexperiments and performed a cross-check for the $W+$ non-prompt J/ψ yields, as explained below.

6.4.1 Pull distributions

In order to confirm that our fit procedure is unbiased and that the errors are estimated correctly, we performed 20000 pseudoexperiments where for each we generated events drawn from a Poisson distribution of the yields of prompt J/ψ, non-prompt J/ψ, prompt combinatorics and non-prompt combinatorics. We then fit the generated pseudodata using the fit model described in Chapter 6 with floating nuisance parameters with a Gaussian constraint with the error from the inclusive J/ψ fit. We keep the results of the fits that successfully converged and get the pulls using the following formula:

$$\text{Pull} = \frac{\text{(Mean of Poisson generated yield)} - \text{(Yield result from fit)}}{\text{Yield error from fit}} \tag{6.1}$$

taking into account the asymmetric errors. Fig. 6.2 shows the pull distributions for the 20000 pseudoexperiments. The results exhibit a small bias, which does not affect the results.

Furthermore, during the fit, we allow the combinatorics background parameterization to vary explicitly, by not fixing the ratio of the prompt:non-prompt components in the J/ψ and combinatorics pseudo-proper time fit. The fact that the fit under the null hypothesis, ignoring the $W^{\pm}$ + prompt J/ψ contribution, cannot sufficiently describe the data, further illustrates the robustness of our fit. In addition, the fit sufficiently describes separately the J/ψ mass peak region and its sidebands in the pseudo-proper time distribution, even though the fit is performed simultaneously in the full J/ψ mass and pseudo-proper time distributions.

We conclude that the fit is robust and stable. The statistical uncertainties are derived by keeping the nuisance parameters fixed and performing the fit again. The systematic uncertainties due to the fit are found from the quadratic difference between the total error and the statistical error, when we allow the nuisance parameters to float within a 1σ Gaussian constraint of the values from the inclusive J/ψ fit. In the calculation of the significance, we use the fit with 1σ constraints, which takes into account both statistical and systematic uncertainties with correlations due to the fit procedure.

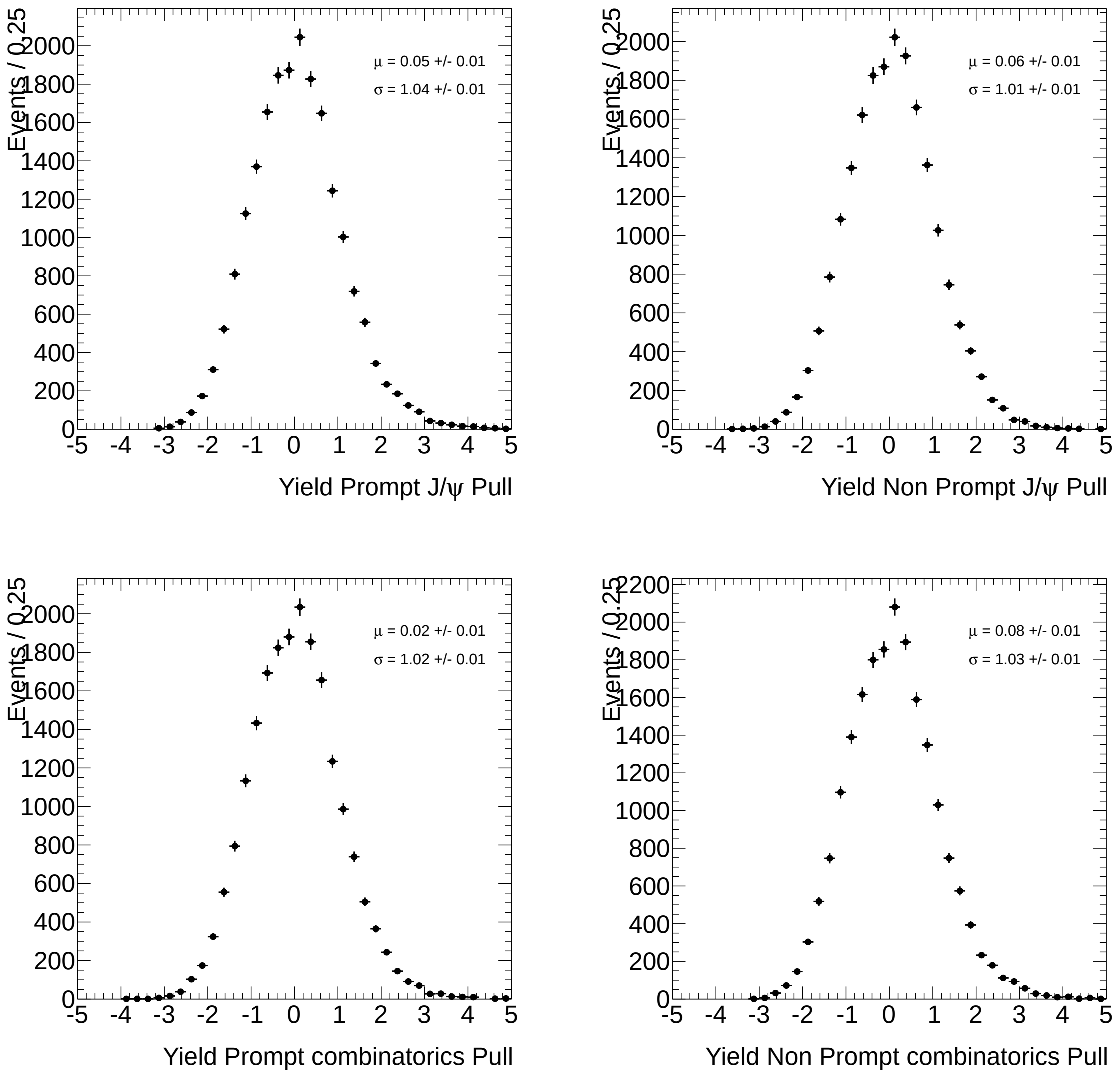

Figure 6.2: Pulls for 20000 pseudoexperiments generated with Poisson fluctuations of the expectations using our fit model, allowing the nuisance parameters to float. The results exhibit a small bias, which however does not affect the results.

6.4.2 $W + b$ cross-check

In addition to the $W^{\pm}$ + prompt J/ψ, this analysis can determine the W and non-prompt J/ψ production. In this section, we investigate if the results are consistent with the published $W + b$ results from ATLAS [75]. There are some differences between the phase space of the two analyses; we use muons with transverse momentum above 25 GeV and missing transverse energy above 20 GeV, compared to 20 GeV for the muon and 25 GeV for missing transverse energy in the $W + b$ result. In addition, the $W + b$ paper requires the $b - jets$ to have transverse momentum above 25 GeV, whereas in this analysis the J/ψ transverse momentum is required to be above 8.5 GeV.

The measured cross-section of $W + b$ in the muon channel is 9.7 pb, which we divide by the inclusive W cross-section from ATLAS [60], which is 5.127 nb, to get the ratio $W+b : W = 1.9\times10^{-3}$. Taking into account the $B^{\pm}/B^0/B_s^0/b-$baryon admixture branching fraction to J/ψ and the $J/\psi \rightarrow \mu\mu$ branching fraction (1.1% and 5.9% respectively), we calculate the ratio $W + b : W$ to be 1.2×10^{-6}.

From our fit in Chapter 7, we determine the number of W +non-prompt J/ψ events to be $41.8^{+8.4}_{-7.3}$. After correcting for the muon efficiencies and J/ψ acceptance, the weighted number of W +non-prompt J/ψ events becomes 86.2. We divide by the number of W candidates in data, 1.48×10^7, to get the ratio $W + \text{non-prompt}J/\psi : W = 5.8 \times 10^{-6}$. If we assume around 50% of this to come from double parton scattering (as estimated for the $W + \text{prompt}J/\psi$ in Section 5.6), the ratio becomes 2.9×10^{-6}.

This result has the same order of magnitude as the expected value from the published results, and considering the large statistical uncertainties in our measurement, it is consistent with expectation. Another reason for the difference is that in the $W + b$ paper, the minimum transverse momentum of the $b-jets$ was required to be 25 GeV, which corresponds to a higher transverse momentum requirement on the J/ψ product, than this analysis' requirement of 8.5 GeV. The $W + b$ background is non-prompt, and this study is meant as a rough cross-check of the fit procedure.

Chapter 7
Observation of $W^{\pm}+$ prompt J/ψ production

Scrivere è sempre nascondere qualcosa in modo che venga poi scoperto.
– Italo Calvino, *Se una notte d'inverno un viaggiatore*

We report on the search for $W^{\pm}$ + prompt J/ψ production, a process that has not been observed before, and has important implications towards our understanding of J/ψ production at hadron colliders, as explained in Chapter 2. Prompt J/ψ is selected as it is being produced directly in association with a W boson, in contrast to non-prompt J/ψ produced from long-lived particles, such as b-hadrons.

We select $W^{\pm}$ + J/ψ candidates as described in Section 5.3, and fit as described in Chapter 6. We have 78 candidate events in the barrel region and 71 events in the endcap region, shown in the two-dimensional J/ψ invariant mass - pseudo-proper time phase space in Fig. 7.1.

The $M_T(W)$ distribution of the candidates, as well as the $\Delta\phi(W, J/\psi)$ distribution are shown in Fig. 7.2. The shape of the $M_T(W)$ distribution is consistent with a W boson. These plots include the non-prompt J/ψ and combinatoric background in the windows in dimuon invariant mass between 3 and 3.2 GeV and pseudoproper time between -0.5 and 0.5 ps. A more sophisticated background subtraction technique, `sPlot`, is used after the two-dimensional fit is conducted, and the $M_T(W)$ and $\Delta\phi(W, J/\psi)$ distributions for $W^{\pm}$ + prompt J/ψ are shown in Figs. 7.4 and 7.6.

The two-dimensional fit in J/ψ candidate mass and pseudo-proper time τ determines the number of prompt J/ψ candidates. The fit is performed separately for barrel and endcap J/ψ candidates. Fig. 7.3 shows the result of the fit in the J/ψ mass for all the J/ψ candidates, when the two fits are summed. The pseudo-proper time fit for the J/ψ mass peak region is also shown in Fig. 7.3. The J/ψ mass peak region is defined as the region with dimuon invariant mass $3-3.2$ GeV.

Fig. 7.4 shows the `sPlot`-weighted distribution of the $\Delta\phi(W, J/\psi)$ for both regions. It is evident from the $\Delta\phi$ distribution that there is a tendency for the candidates to have angles close to π, i.e. for the W boson and J/ψ to be back-to-back. By studying the simulated predictions of $W^{\pm}+$prompt J/ψ production from simulation, they tend to also exhibit large angles, in contrast to the expected uniform distribution of double parton scattering events.

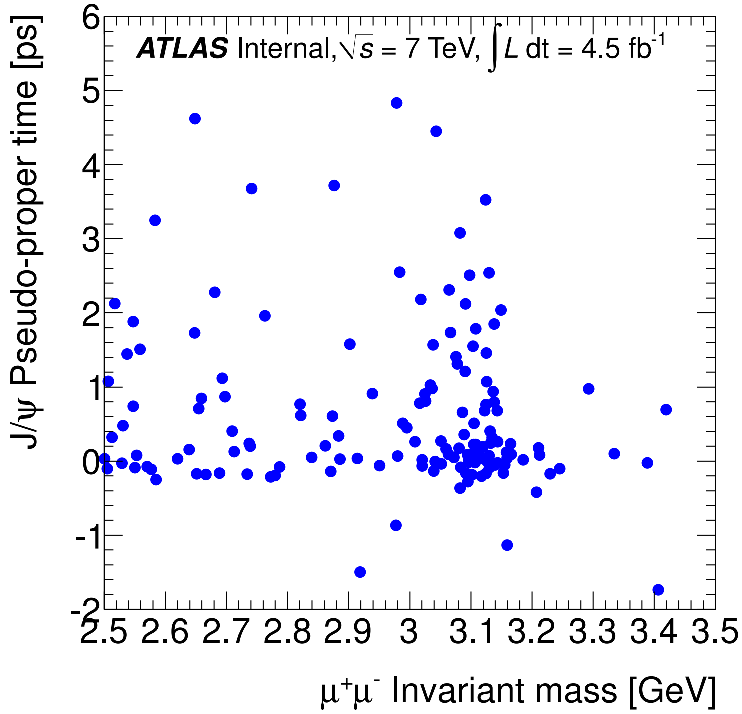

Figure 7.1: Two-dimensional plot of $W^\pm + J/\psi$ candidates in J/ψ invariant mass - pseudo-proper time in the whole region in J/ψ rapidity $(0-2.1)$. Most of the candidates fall near the J/ψ mass of 3.097 GeV and pseudo-proper time 0 ps, as expected from prompt J/ψ production.

The expected double parton scattering contribution is also shown on Fig. 7.4, normalized to the expected number of double parton scattering events as calculated in Section 5.6.

We observe a non-zero yield of $W^\pm +$ prompt J/ψ candidates, after subtraction of the pileup contribution. We use a two-step method to determine the significance of the $W^\pm +$ prompt J/ψ process production: first, we establish a significance for the production of prompt J/ψ candidates in $W^\pm +$prompt J/ψ candidates, and then establish that the prompt candidates are consistent with W production rather than multi-jet background. For the first stage, we fit the $W^\pm + J/\psi$ candidates in the data in the J/ψ mass and pseudo-proper time distributions with the procedure described in Chapter 6, and obtain the $-12\Delta(\ln \mathcal{L})$ between the best fit hypothesis (with a floating prompt J/ψ yield) and the null hypothesis (prompt J/ψ yield forced to zero).

After establishing the observation of prompt J/ψ, we fit the `sPlot`-weighted prompt

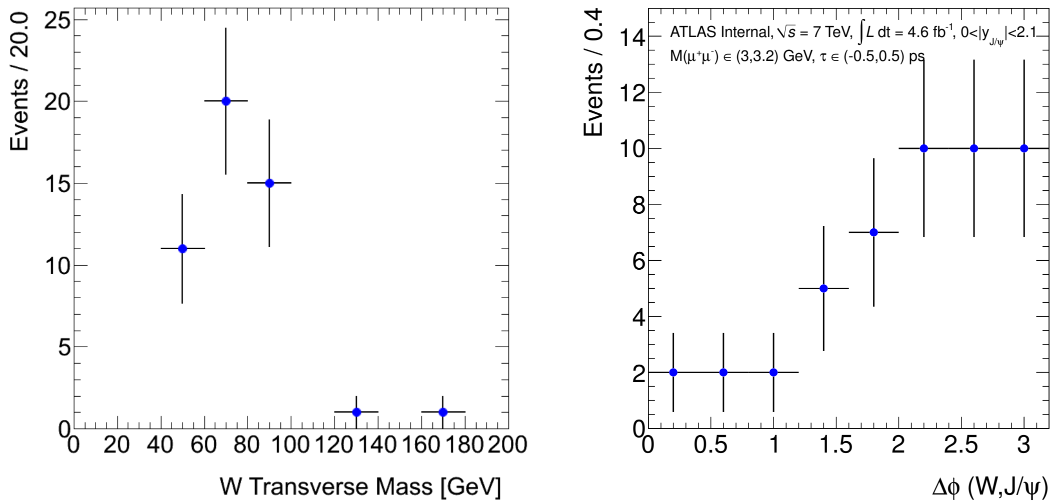

Figure 7.2: W Transverse Mass and $\Delta\phi(W, J/\psi)$ distributions for $W^{\pm} + J/\psi$ candidates, where the shape follows the expected shape of a W boson, and one-dimensional plot of the angle between the W boson and the J/ψ meson. The candidates are selected as the $W^{\pm}+J/\psi$ events with J/ψ invariant mass in $(3, 3.2)$ GeV and pseudo-proper time in $(-0.5, 0.5)$ ps. The events are not efficiency/acceptance-weighted, and no background has been subtracted.

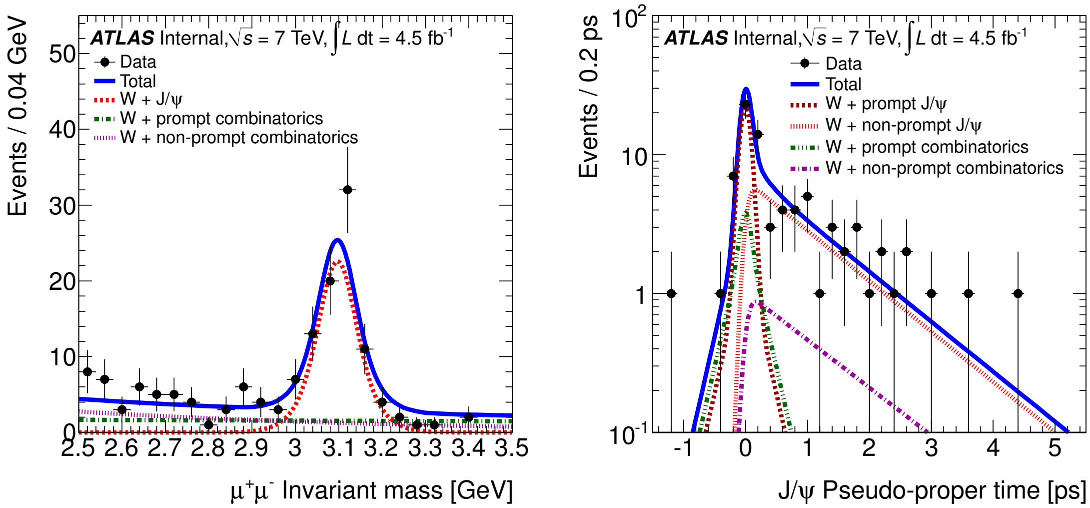

Figure 7.3: Invariant mass and lifetime projections of the two-dimensional mass-lifetime fit used to extract the prompt J/ψ candidates.

J/ψ candidates in the W transverse mass distribution to separate the real W boson process from multi-jet background. We repeat the fit with the null hypothesis, assuming no W exists in association with the prompt J/ψ candidates. The significance of the W production,

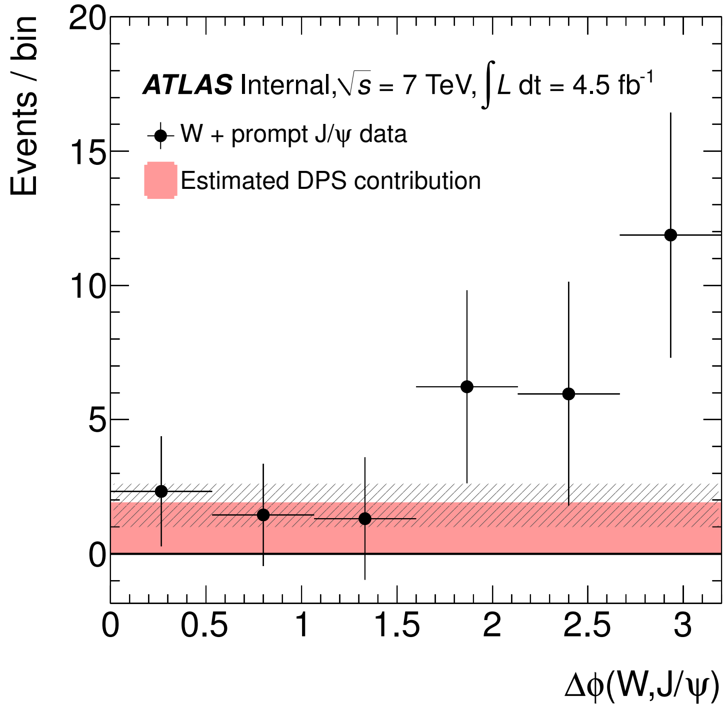

Figure 7.4: The sPlot-weighted azimuthal angle between the $W^{\pm}$ and the J/ψ is shown for $W^{\pm}$ + prompt J/ψ candidates. No efficiency or acceptance corrections are applied. The determined DPS contribution (with systematic uncertainties) is overlaid, using a flat DPS template validated using PYTHIA8 [67] MC simulation and normalized to the total rate as estimated in Section 5.6. The hashed region shows the uncertainty on the DPS estimate. The $\Delta\phi$ distribution is not itself used in the estimation of the DPS component of the $W^{\pm}$ + prompt J/ψ data.

as opposed to multi-jet, in association with J/ψ is found using the $\Delta\chi^2$ between the two hypotheses.

Table 7.1 shows the yields in each of the two detector regions, barrel and endcap, including the statistical error from the fit for the prompt J/ψ, non-prompt J/ψ and combinatoric background components. We also extract the p-value for the prompt J/ψ hypothesis, and find the significance with respect to the null hypothesis to be 5.1σ.

To estimate the p-value with pseudoexperiments, we performed 1.4 million pseudoexperiments where for each experiment we generated events drawn from a Poisson distribution of the yields of non-prompt J/ψ, prompt combinatorics and non-prompt combinatorics from the null (background-only) hypothesis. The nuisance parameters of the fit were also ran-

Yields and significance from 2-dimensional fit			
Process	Barrel	Endcap	Total
Prompt J/ψ	$10.0^{+4.7}_{-4.0}(\text{stat})^{+0.3}_{-0.2}(\text{syst})$	$19.2^{+5.8}_{-5.1}(\text{stat})^{+0.3}_{-0.3}(\text{syst})$	$29.2^{+7.5}_{-6.5}(*)$
Non-prompt J/ψ	$27.9^{+6.5}_{-5.8}(\text{stat})^{+0.2}_{-0.2}(\text{syst})$	$13.9^{+5.3}_{-4.5}(\text{stat})^{+0.1}_{-0.2}(\text{syst})$	$41.8^{+8.4}_{-7.3}$
Prompt combinatorics	$20.4^{+5.9}_{-5.1}(\text{stat})^{+0.2}_{-0.2}(\text{syst})$	$18.8^{+6.3}_{-5.3}(\text{stat})^{+0.3}_{-0.3}(\text{syst})$	$39.2^{+8.6}_{-7.3}$
Non-prompt combinatorics	$19.8^{+5.8}_{-4.9}(\text{stat})^{+0.2}_{-0.2}(\text{syst})$	$19.2^{+6.1}_{-5.1}(\text{stat})^{+0.3}_{-0.2}(\text{syst})$	$39.0^{+8.4}_{-7.1}$
p-value	8.0×10^{-3}	1.4×10^{-6}	2.1×10^{-7}
Significance (σ)	2.4	4.7	5.1

(*) of which 1.8 ± 0.2 originate from pileup

Table 7.1: The yields for the prompt J/ψ, non-prompt J/ψ and combinatorics background using the fit method in Chapter 6. The errors shown include the statistical and systematic uncertainties from the fit, as described in Section 6.3. The systematic uncertainties due to the fit procedure are negligible. The significance is calculated using the p-value from pseudoexperiments.

domized at generation for each pseudoexperiment. We then fit the generated pseudodata using the background-only hypothesis, and also with the signal+background hypothesis and we calculated for each pseudoexperiment the $-2\Delta(\ln\mathcal{L})$ value between the two fits. The nuisance parameters were allowed to float within their Gaussian constraints during the fitting stage, following the same procedure as for the data, as described in Chapter 6. This way, we can estimate the p-value, i.e. how often we can expect 0 prompt J/ψ events to fluctuate upwards to a value at least as high as the result from the data, hence a high $-2\Delta(\ln\mathcal{L})$ between the null and signal+background hypotheses.

As described in Chapter 6, we use `sPlot` to plot the W transverse mass for the prompt J/ψ candidates. We then compare multi-jet-only and W-only hypotheses using data-driven templates for $M_T(W)$. The W-only model is strongly preferred, with a $\Delta\chi^2$ with respect to the multi-jet-only model of > 40 for five degrees of freedom, as shown in Fig. 7.5.

We fit the `sPlot`-weighted W transverse mass distribution with both the W and the multi-jet templates, to extract the relative yield of the two processes in association with the prompt J/ψ production, by minimizing the χ^2 for the range of values for the fraction of W candidates. Table 7.2 shows the yields for W and multi-jet background, and Fig. 7.6 shows the fit in the W transverse mass for all the prompt J/ψ candidates. Assuming a flat prior in $[0, 1]$ for the multi-jet fraction, the probability of data given the hypothesis is proportional to $\exp(-(f(\text{multi-jet}) - \text{best fit} f(\text{multi-jet})^2/2\sigma_{\text{fit}}))$. Following Bayes' theorem, we get the

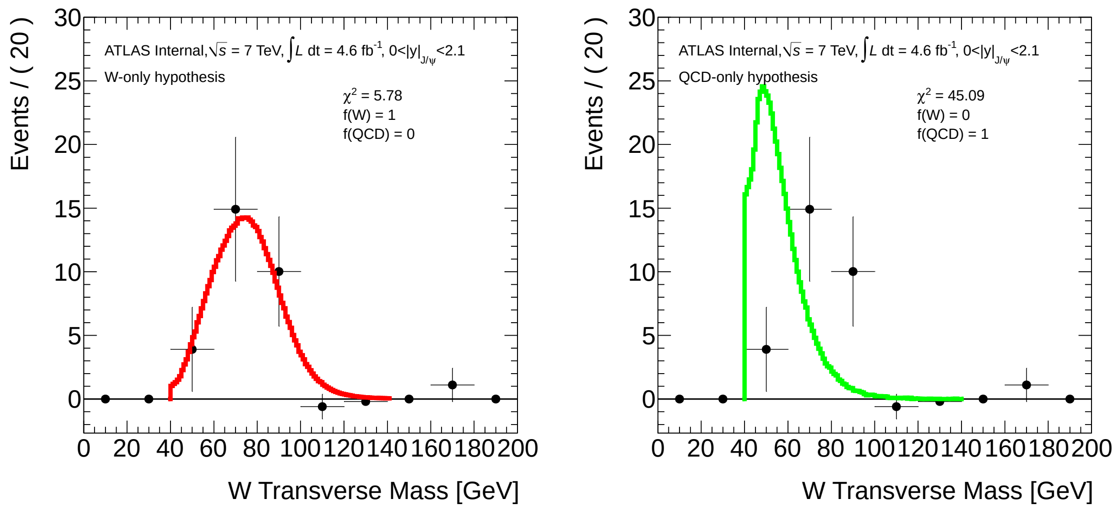

Figure 7.5: The fit on the W transverse mass distribution for prompt J/ψ candidates using `sPlot` is shown for the W-only hypothesis (left) and the multi-jet-only hypothesis (right). The W-only hypothesis is strongly preferred. Only the first five bins above 40 GeV are used to compute the χ^2. The fit is performed in the region 40–140 GeV in $M_T(W)$.

Process	Yield
W + prompt J/ψ	29.1 ± 4.6
multi-jet + prompt J/ψ	0.1 ± 4.6

Table 7.2: The yields for the prompt J/ψ candidates associated with W boson or multi-jet background, using the fit method in Chapter 6. The errors shown are statistical.

fraction of multi-jet to be smaller than 0.31 at 95% credibility level.

7.1 Event displays

To better illustrate the observation of the $W^{\pm} + J/\psi$ process, we use the Atlantis software package to draw the displays for specific events that have a high `sPlot` weight for being $W^{\pm}$ + prompt J/ψ events. Figs 7.7 and 7.8 show two examples of such events.

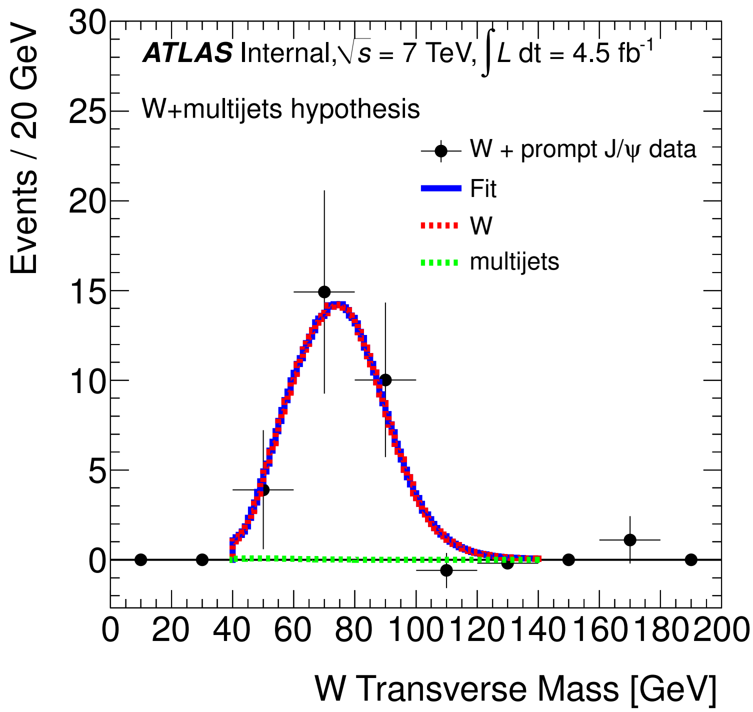

Figure 7.6: `sPlot` of W transverse mass for prompt J/ψ candidates, with fit to determine W and multi-jet components. The fit is performed in the region 40–140 GeV in $M_T(W)$.

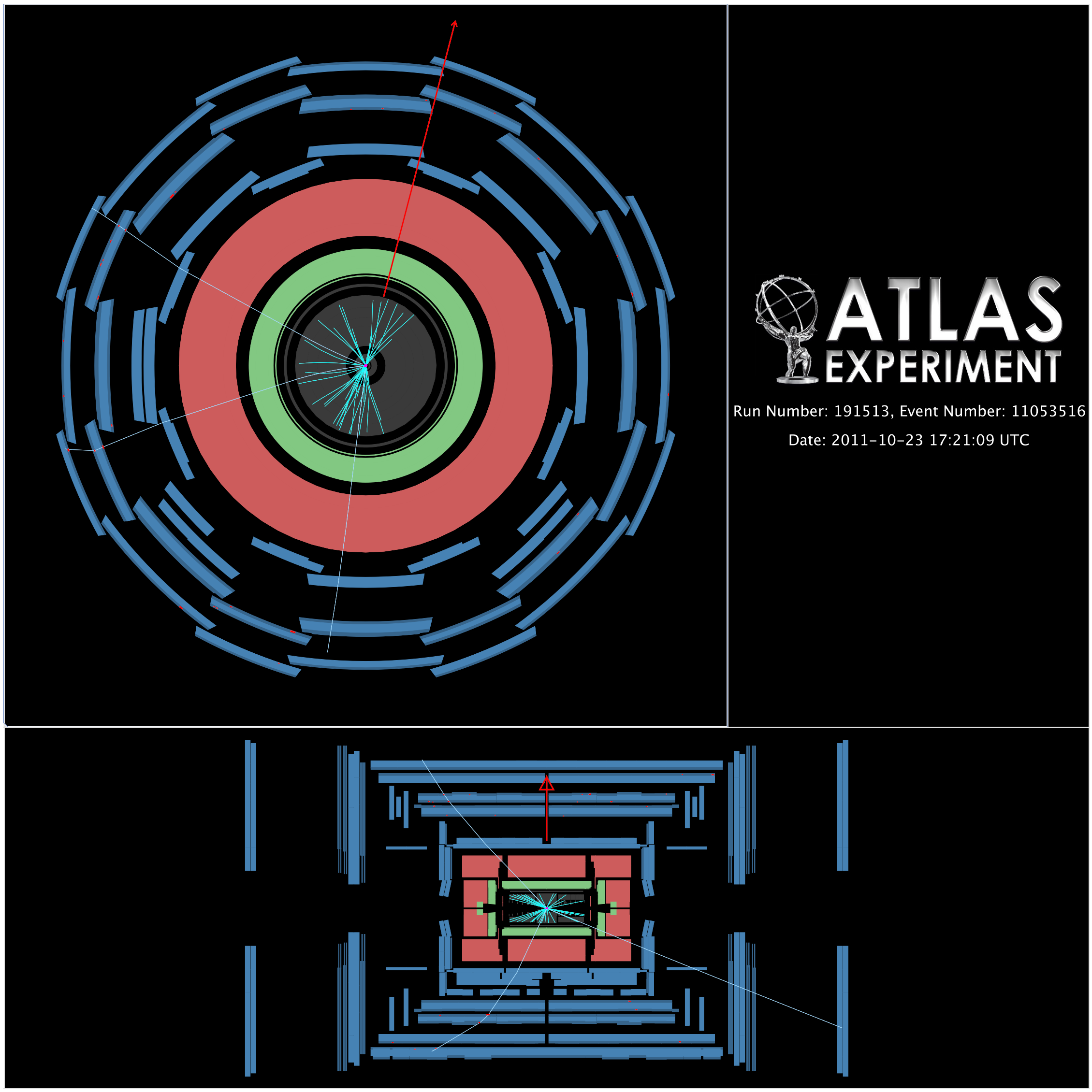

Figure 7.7: This event display for event 11053516 in run 191513 clearly shows the two J/ψ muons at the 9 o'clock position, the W muon at 6 o'clock, and the $E_{\mathrm{T}}^{\mathrm{miss}}$ vector in the direction of 12 o'clock, opposite from the muon originating from the W.

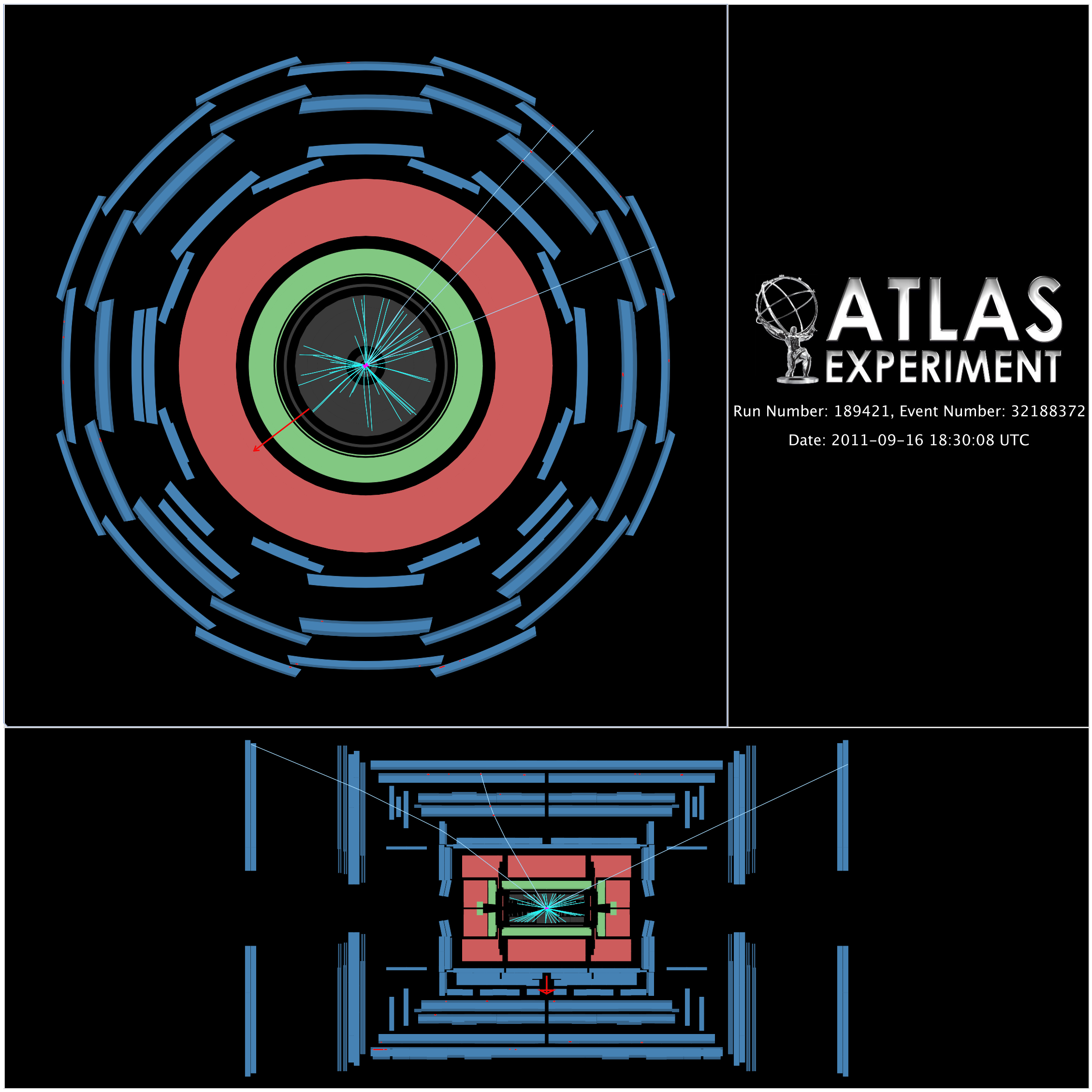

Figure 7.8: This event display for event 321883372 in run 189421 clearly shows the two J/ψ muons at the 1 o'clock position, the W muon at 3 o'clock, and the $E_{\mathrm{T}}^{\mathrm{miss}}$ vector in the direction of 9 o'clock, opposite from the muon originating from the W.

Chapter 8

Measurement of the cross section ratio $W^{\pm} + J/\psi$: W

C'est le temps que tu a perdu pour ta rose qui fait ta rose si importante.

– Antoine de Saint-Exupery, *Le petit prince*

Once the observation of the $W^{\pm}+$prompt J/ψ process is established, as shown in Chapter 7, we need to measure the cross section of the $W^{\pm}+$prompt J/ψ process. To cancel errors related to the W boson, we calculate the cross section ratio of the $W^{\pm}+$prompt J/ψ process to the inclusive W production, as explained in Section 5.1. Measuring the cross section ratio of the $W^{\pm}+$ prompt J/ψ process to the inclusive W, and subtracting the double parton scattering contribution, as explained in Section 5.6, allows us to compare our measurement with theoretical predictions for single parton scattering production of $W^{\pm}+$prompt J/ψ, as will be shown below.

We extract the cross-section ratio $R_{J/\psi}$, by dividing the number of $W^{\pm}+$ prompt J/ψ candidates determined by the two-dimensional mass-pseudoproper time fit described in Chapter 6, by the number of inclusive W candidates in the same fiducial region.

$$R_{J/\psi} \equiv \frac{\sigma_{W+J/\psi}}{\sigma_W} \equiv \frac{\frac{N_{W+J/\psi}}{\mathcal{L}\times\epsilon_W\times\epsilon_{J/\psi}\times\mathcal{A}_{J/\psi}}}{\frac{N_W}{\mathcal{L}\times\epsilon_W}} \equiv \frac{N_{W+J/\psi}}{N_W\times\epsilon_{J/\psi}\times\mathcal{A}_{J/\psi}}$$

Each $W^{\pm}+$prompt J/ψ candidate is weighted by the geometrical acceptance of the J/ψ for that rapidity and p_{T} (evaluated in Section 5.4.2), and the efficiency of reconstructing the J/ψ muons, discussed in Section 5.4.1. The nominal measurement assumes isotropic J/ψ decays. In addition, the branching fraction of the $J/\psi \to \mu\mu$ decay is implicitly included in the measurement.

Fig. 8.1 shows the inclusive and double parton scattering differential cross-section ratio as a function of J/ψ transverse momentum for the isotropic scenario, after the subtraction of the pileup background, whereas Fig. 8.2 shows the DPS-subtracted (SPS) differential cross-section ratio after the subtraction of the double parton scattering estimated contribution as well. Table 8.1 shows the inclusive and DPS-subtracted (SPS) differential cross-section ratio, after the subtraction of the double parton scattering component.

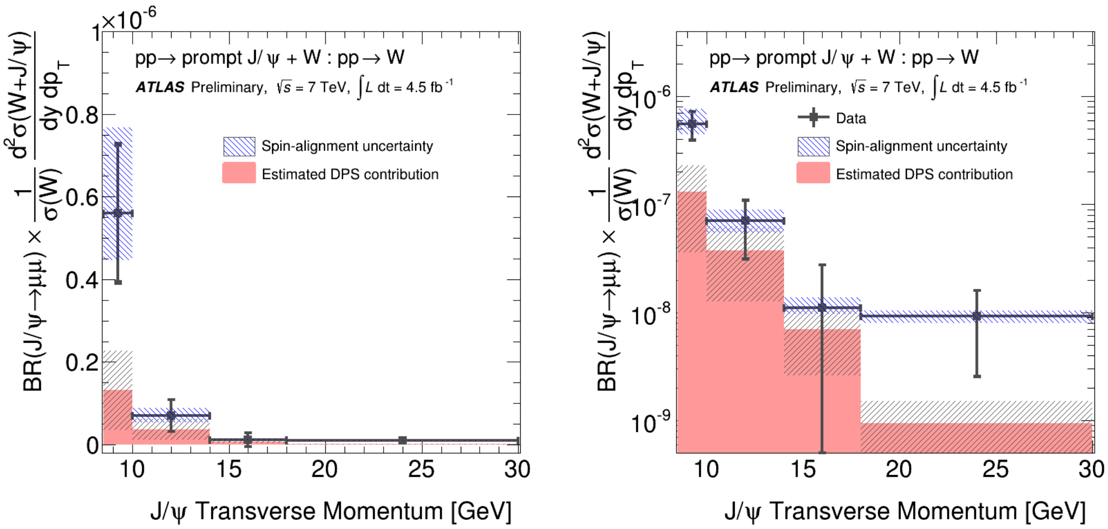

Figure 8.1: The inclusive differential cross-section ratio $R_{J/\psi}$ as function of J/ψ transverse momentum, for the isotropic spin-alignment scenario in linear (left) and logarithmic (right) scale. The error band shows the range of the value of the ratio with different spin-alignment scenarios. The total error is statistical and systematic, whereas the first tick shows the systematic error. The expected pileup background contribution has been subtracted, but the double parton scattering contribution is included in the total ratio. The expected contribution of double parton scattering is also shown.

Table 8.2 shows the differential cross-section ratio results for all considered spin alignment scenarios, after the subtraction of pileup background, estimated in Section 5.5.5. The double parton scattering expectation has a high uncertainty (33%(stat)$^{+20}_{-33}$%(syst)) as estimated in Section 5.6. The inclusive single parton scattering and double parton scattering contribution is shown in Table 8.2. The expected single parton scattering contribution is shown in Table 8.3, after the subtraction of the double parton scattering estimate, and the introduction of an additional systematic uncertainty due the DPS estimate.

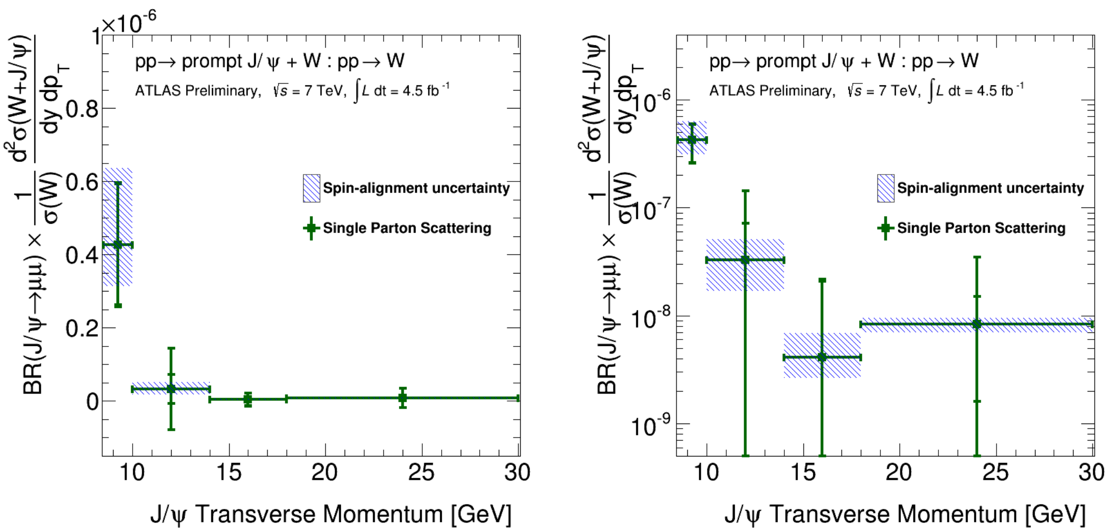

Figure 8.2: The DPS-subtracted (SPS) differential cross-section ratio $R_{J/\psi}$ as function of J/ψ transverse momentum, for the isotropic spin-alignment scenario in linear (left) and logarithmic (right) scale. The error band shows the range of the value of the ratio with different spin-alignment scenarios. The total error is statistical and systematic, whereas the first tick shows the systematic error, including the uncertainty due to the double parton scattering background estimate. The expected pileup background and double parton scattering contributions have been subtracted.

Differential cross-section ratio $R_{J/\psi}$ for the isotropic spin-alignment scenario		
Bin $\|y\| \times p_{\mathrm{T}}$ (GeV)	Observed (SPS+DPS) Ratio (10^{-6})	DPS–subtracted Ratio (10^{-6})
$(0, 1) \times (8.5, 10)$	$0.45 \pm 0.23(\mathrm{stat}) \pm 0.035(\mathrm{syst})^{+0.2}_{-0.12}(\mathrm{spin})$	$0.31 \pm 0.23(\mathrm{stat}) \pm 0.035(\mathrm{syst})^{+0.2}_{-0.12}(\mathrm{spin}) \pm 0.075(\mathrm{DPS})$
$(1, 2.1) \times (8.5, 10)$	$0.63 \pm 0.23(\mathrm{stat}) \pm 0.055(\mathrm{syst})^{+0.21}_{-0.1}(\mathrm{spin})$	$0.51 \pm 0.23(\mathrm{stat}) \pm 0.055(\mathrm{syst})^{+0.21}_{-0.1}(\mathrm{spin}) \pm 0.06(\mathrm{DPS})$
$(0, 1) \times (10, 14)$	$0.075 \pm 0.064(\mathrm{stat}) \pm 0.0062(\mathrm{syst})^{+0.023}_{-0.025}(\mathrm{spin})$	$0.034 \pm 0.064(\mathrm{stat}) \pm 0.0062(\mathrm{syst})^{+0.023}_{-0.025}(\mathrm{spin}) \pm 0.019(\mathrm{DPS})$
$(1, 2.1) \times (10, 14)$	$0.06 \pm 0.044(\mathrm{stat}) \pm 0.0057(\mathrm{syst})^{+0.013}_{-0.006}(\mathrm{spin})$	$0.026 \pm 0.044(\mathrm{stat}) \pm 0.0057(\mathrm{syst})^{+0.013}_{-0.006}(\mathrm{spin}) \pm 0.016(\mathrm{DPS})$
$(0, 1) \times (14, 18)$	$0.012 \pm 0.028(\mathrm{stat}) \pm 0.001(\mathrm{syst})^{+0.003}_{-0.0023}(\mathrm{spin})$	$0.0042 \pm 0.028(\mathrm{stat}) \pm 0.001(\mathrm{syst})^{+0.003}_{-0.0023}(\mathrm{spin}) \pm 0.0035(\mathrm{DPS})$
$(1, 2.1) \times (14, 18)$	$0.0095 \pm 0.019(\mathrm{stat}) \pm 0.00092(\mathrm{syst})^{+0.0023}_{-0.00054}(\mathrm{spin})$	$0.0033 \pm 0.019(\mathrm{stat}) \pm 0.00092(\mathrm{syst})^{+0.0023}_{-0.00054}(\mathrm{spin}) \pm 0.0027(\mathrm{DPS})$
$(0, 1) \times (18, 30)$	$0.0045 \pm 0.009(\mathrm{stat}) \pm 0.00033(\mathrm{syst})^{+0.00065}_{-0.00054}(\mathrm{spin})$	$0.0034 \pm 0.009(\mathrm{stat}) \pm 0.00033(\mathrm{syst})^{+0.00065}_{-0.00054}(\mathrm{spin}) \pm 0.00047(\mathrm{DPS})$
$(1, 2.1) \times (18, 30)$	$0.014 \pm 0.01(\mathrm{stat}) \pm 0.0011(\mathrm{syst})^{+0.0017}_{-0.0019}(\mathrm{spin})$	$0.013 \pm 0.01(\mathrm{stat}) \pm 0.0011(\mathrm{syst})^{+0.0017}_{-0.0019}(\mathrm{spin}) \pm 0.00033(\mathrm{DPS})$

Table 8.1: The inclusive (single parton scattering+double parton scattering) differential cross-section ratio $R_{J/\psi}$ with uncertainties for the isotropic spin-alignment scenario after the subtraction of the pileup background is shown in the second column for each ($|y| \times p_T$)-bin shown in the first column. The double parton scattering component, as estimated in Section 5.6 is subtracted from the inclusive ratio to calculate the DPS-subtracted differential cross-section ratio $R_{J/\psi}$, shown in the last column, with the addition of a systematic uncertainty for the double parton scattering estimate.

We define the fiducial cross section ratio

$$\begin{aligned} R^{\text{fid}}_{J/\psi} &= \frac{\text{BR}(J/\psi \to \mu^+\mu^-)}{\sigma_{\text{fid}}(pp \to W^\pm)} \cdot \frac{d\sigma_{\text{fid}}(pp \to W^\pm + J/\psi)}{dy} \\ &= \frac{N^{\text{ec}}(W^\pm + J/\psi)}{N(W^\pm)} \frac{1}{\Delta y} - R^{\text{fid}}_{\text{pileup}}, \end{aligned}$$

where $N^{\text{ec}}(W^\pm + J/\psi)$ is the yield of $W^\pm +$ prompt J/ψ events after correction for the J/ψ muon reconstruction efficiencies, $N(W^\pm)$ is the background-subtracted yield of inclusive $W^\pm$ events, $\Delta y = 4.2$ is the size of the fiducial region in $y_{J/\psi}$, and $R^{\text{fid}}_{\text{pileup}}$ is the expected pileup background contribution in the fiducal J/ψ acceptance. For $R^{\text{fid}}_{J/\psi}$, we do not correct either for the the incomplete acceptance for J/ψ muons or for the $W^\pm$ acceptance. Also note that only the cross section for $8.5 < p_{\text{T}}^{J/\psi} < 30$ GeV is considered.

In addition to reporting $R^{\text{fid}}_{J/\psi}$, we present results corrected for the fiducial acceptance of the muons from the J/ψ decay, but maintaining the p_{T} range:

$$\begin{aligned} R^{\text{incl}}_{J/\psi} &= \frac{\text{BR}(J/\psi \to \mu^+\mu^-)}{\sigma_{\text{fid}}(pp \to W^\pm)} \cdot \frac{d\sigma(pp \to W^\pm + J/\psi)}{dy} \\ &= \frac{N^{\text{ec+ac}}(W^\pm + J/\psi)}{N(W^\pm)} \frac{1}{\Delta y} - R_{\text{pileup}}, \end{aligned}$$

where $N^{\text{ec+ac}}(W^\pm + J/\psi)$ is the yield of $W^\pm +$ prompt J/ψ events after both J/ψ muon efficiency corrections and J/ψ acceptance corrections, R_{pileup} is the expected pileup contribution in the full J/ψ decay phase space, and other variables are as for $R^{\text{fid}}_{J/\psi}$. The J/ψ spin-alignment, which determines the angular distribution of the muons from the J/ψ decay and thus modifies the acceptance for the J/ψ to be detected within the fiducial volume, is not known and is dependent on the underlying production mechanism. Five extreme scenarios that bound the possible variation are considered for the acceptance and assigned as a systematic uncertainty.

The isotropic spin-alignment scenario is assumed for the central result, and the variations of the result with the different spin-alignment scenarios are also reported in HEPDATA. The DPS contribution to $R^{\text{incl}}_{J/\psi}$ is estimated to be $(48 \pm 19) \times 10^{-8}$. Subtracting the DPS contribution from $R^{\text{incl}}_{J/\psi}$ gives an estimate $R^{\text{DPS sub}}_{J/\psi}$ of the single parton scattering rate, which can be directly compared with leading-order (LO) color singlet pQCD predictions and next-to-leading-order (NLO) color octet predictions [44].

Inclusive Differential cross-section ratio $R_{J/\psi}$		
Spin-alignment scenario	Bin $\|y\| \times p_{\mathrm{T}}$ (GeV)	Ratio (10^{-6})
Isotropic	$(0, 1) \times (8.5, 10)$	$0.45 \pm 0.23(\mathrm{stat}) \pm 0.035(\mathrm{syst})^{+0.2}_{-0.12}(\mathrm{spin})$
	$(1, 2.1) \times (8.5, 10)$	$0.63 \pm 0.23(\mathrm{stat}) \pm 0.055(\mathrm{syst})^{+0.21}_{-0.1}(\mathrm{spin})$
	$(0, 1) \times (10, 14)$	$0.075 \pm 0.064(\mathrm{stat}) \pm 0.0062(\mathrm{syst})^{+0.023}_{-0.025}(\mathrm{spin})$
	$(1, 2.1) \times (10, 14)$	$0.06 \pm 0.044(\mathrm{stat}) \pm 0.0057(\mathrm{syst})^{+0.013}_{-0.006}(\mathrm{spin})$
	$(0, 1) \times (14, 18)$	$0.012 \pm 0.028(\mathrm{stat}) \pm 0.001(\mathrm{syst})^{+0.003}_{-0.0023}(\mathrm{spin})$
	$(1, 2.1) \times (14, 18)$	$0.0095 \pm 0.019(\mathrm{stat}) \pm 0.00092(\mathrm{syst})^{+0.0023}_{-0.00054}(\mathrm{spin})$
	$(0, 1) \times (18, 30)$	$0.0045 \pm 0.009(\mathrm{stat}) \pm 0.00033(\mathrm{syst})^{+0.00065}_{-0.00054}(\mathrm{spin})$
	$(1, 2.1) \times (18, 30)$	$0.014 \pm 0.01(\mathrm{stat}) \pm 0.0011(\mathrm{syst})^{+0.0017}_{-0.0019}(\mathrm{spin})$
Longitudinal	$(0, 1) \times (8.5, 10)$	0.5
	$(1, 2.1) \times (8.5, 10)$	0.53
	$(0, 1) \times (10, 14)$	0.094
	$(1, 2.1) \times (10, 14)$	0.054
	$(0, 1) \times (14, 18)$	0.0097
	$(1, 2.1) \times (14, 18)$	0.0091
	$(0, 1) \times (18, 30)$	0.0042
	$(1, 2.1) \times (18, 30)$	0.012
Transverse 0	$(0, 1) \times (8.5, 10)$	0.44
	$(1, 2.1) \times (8.5, 10)$	0.7
	$(0, 1) \times (10, 14)$	0.067
	$(1, 2.1) \times (10, 14)$	0.065
	$(0, 1) \times (14, 18)$	0.013
	$(1, 2.1) \times (14, 18)$	0.01
	$(0, 1) \times (18, 30)$	0.0045
	$(1, 2.1) \times (18, 30)$	0.015
Transverse P	$(0, 1) \times (8.5, 10)$	0.65
	$(1, 2.1) \times (8.5, 10)$	0.84
	$(0, 1) \times (10, 14)$	0.098
	$(1, 2.1) \times (10, 14)$	0.073
	$(0, 1) \times (14, 18)$	0.015
	$(1, 2.1) \times (14, 18)$	0.012
	$(0, 1) \times (18, 30)$	0.0051
	$(1, 2.1) \times (18, 30)$	0.015
Transverse M	$(0, 1) \times (8.5, 10)$	0.33
	$(1, 2.1) \times (8.5, 10)$	0.6
	$(0, 1) \times (10, 14)$	0.049
	$(1, 2.1) \times (10, 14)$	0.058
	$(0, 1) \times (14, 18)$	0.011
	$(1, 2.1) \times (14, 18)$	0.009
	$(0, 1) \times (18, 30)$	0.004
	$(1, 2.1) \times (18, 30)$	0.014

Table 8.2: Inclusive differential cross-section ratio $R_{J/\psi}$ for five spin-alignment scenarios per J/ψ transverse momentum and rapidity bin. Both single parton scattering and double parton scattering contributions are included. The statistical and systematic errors are the same between the different spin-alignment scenarios.

DPS–subtracted (SPS) Differential cross-section ratio $R_{J/\psi}$		
Spin-alignment scenario	Bin $\|y\| \times p_T$ (GeV)	Ratio (10^{-6})
Isotropic	$(0, 1) \times (8.5, 10)$	$0.31 \pm 0.23(\text{stat}) \pm 0.035(\text{syst})^{+0.2}_{-0.12}(\text{spin}) \pm 0.075(\text{DPS})$
	$(1, 2.1) \times (8.5, 10)$	$0.51 \pm 0.23(\text{stat}) \pm 0.055(\text{syst})^{+0.21}_{-0.1}(\text{spin}) \pm 0.06(\text{DPS})$
	$(0, 1) \times (10, 14)$	$0.034 \pm 0.064(\text{stat}) \pm 0.0062(\text{syst})^{+0.023}_{-0.025}(\text{spin}) \pm 0.019(\text{DPS})$
	$(1, 2.1) \times (10, 14)$	$0.026 \pm 0.044(\text{stat}) \pm 0.0057(\text{syst})^{+0.013}_{-0.006}(\text{spin}) \pm 0.016(\text{DPS})$
	$(0, 1) \times (14, 18)$	$0.0042 \pm 0.028(\text{stat}) \pm 0.001(\text{syst})^{+0.003}_{-0.0023}(\text{spin}) \pm 0.0035(\text{DPS})$
	$(1, 2.1) \times (14, 18)$	$0.0033 \pm 0.019(\text{stat}) \pm 0.00092(\text{syst})^{+0.0023}_{-0.00054}(\text{spin}) \pm 0.0027(\text{DPS})$
	$(0, 1) \times (18, 30)$	$0.0034 \pm 0.009(\text{stat}) \pm 0.00033(\text{syst})^{+0.00065}_{-0.00054}(\text{spin}) \pm 0.00047(\text{DPS})$
	$(1, 2.1) \times (18, 30)$	$0.013 \pm 0.01(\text{stat}) \pm 0.0011(\text{syst})^{+0.0017}_{-0.0019}(\text{spin}) \pm 0.00033(\text{DPS})$
Longitudinal	$(0, 1) \times (8.5, 10)$	0.36
	$(1, 2.1) \times (8.5, 10)$	0.41
	$(0, 1) \times (10, 14)$	0.054
	$(1, 2.1) \times (10, 14)$	0.02
	$(0, 1) \times (14, 18)$	0.0019
	$(1, 2.1) \times (14, 18)$	0.0029
	$(0, 1) \times (18, 30)$	0.0031
	$(1, 2.1) \times (18, 30)$	0.011
Transverse 0	$(0, 1) \times (8.5, 10)$	0.3
	$(1, 2.1) \times (8.5, 10)$	0.57
	$(0, 1) \times (10, 14)$	0.027
	$(1, 2.1) \times (10, 14)$	0.03
	$(0, 1) \times (14, 18)$	0.0051
	$(1, 2.1) \times (14, 18)$	0.0041
	$(0, 1) \times (18, 30)$	0.0034
	$(1, 2.1) \times (18, 30)$	0.014
Transverse P	$(0, 1) \times (8.5, 10)$	0.51
	$(1, 2.1) \times (8.5, 10)$	0.72
	$(0, 1) \times (10, 14)$	0.058
	$(1, 2.1) \times (10, 14)$	0.039
	$(0, 1) \times (14, 18)$	0.0072
	$(1, 2.1) \times (14, 18)$	0.0056
	$(0, 1) \times (18, 30)$	0.004
	$(1, 2.1) \times (18, 30)$	0.014
Transverse M	$(0, 1) \times (8.5, 10)$	0.19
	$(1, 2.1) \times (8.5, 10)$	0.47
	$(0, 1) \times (10, 14)$	0.0091
	$(1, 2.1) \times (10, 14)$	0.023
	$(0, 1) \times (14, 18)$	0.0034
	$(1, 2.1) \times (14, 18)$	0.0028
	$(0, 1) \times (18, 30)$	0.0029
	$(1, 2.1) \times (18, 30)$	0.013

Table 8.3: DPS-subtracted (SPS) differential cross-section ratio $R_{J/\psi}$ for five spin-alignment scenarios per J/ψ transverse momentum and rapidity bin. The double parton scattering contribution is subtracted from the inclusive ratio, and an additional systematic uncertainty is included to reflect this. The statistical and systematic errors are the same between the different spin-alignment scenarios.

The values of the three measured ratios are shown in Fig. 8.3 and are:

$$
\begin{aligned}
R^{\text{fid}}_{J/\psi} &= (51 \pm 13 \pm 4) \times 10^{-8} \\
R^{\text{incl}}_{J/\psi} &= (126 \pm 32 \pm 9^{+41}_{-25}) \times 10^{-8} \\
R^{\text{DPS sub}}_{J/\psi} &= (78 \pm 32 \pm 22^{+41}_{-25}) \times 10^{-8},
\end{aligned}
$$

where the first uncertainty is statistical, the second is systematic and the third (where applicable) is the uncertainty due to spin-alignment. The systematic uncertainty on the DPS-subtracted ratio includes the uncertainty on the estimated DPS contribution, which itself includes a separate spin-alignment uncertainty.

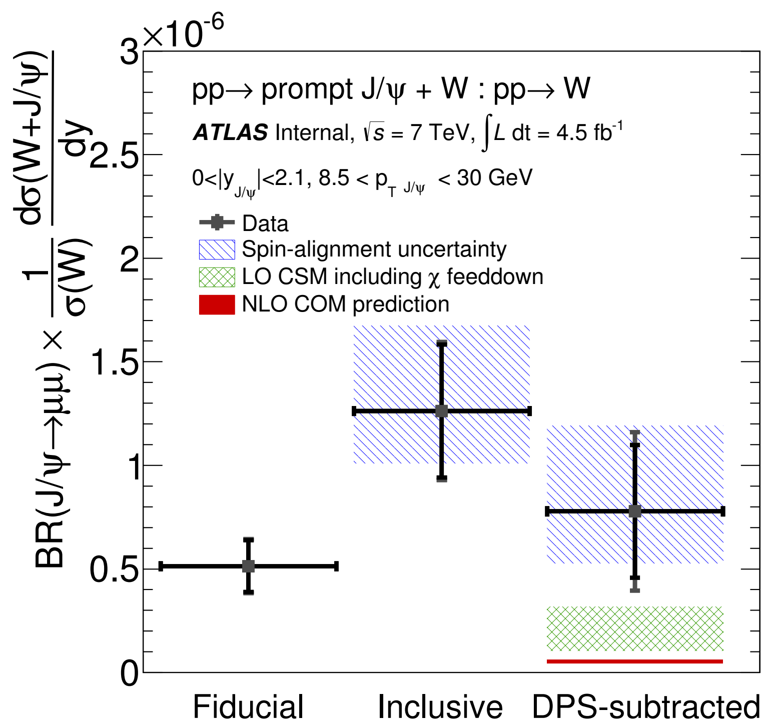

Figure 8.3: The $W^{\pm}$ + prompt J/ψ: W production differential cross section ratio in the J/ψ fiducial region (Fiducial), after correction for J/ψ acceptance (Inclusive), and after subtraction of the double-parton scattering component (DPS-subtracted). The shaded band represents the envelope of variation due to different possible spin-alignment configurations. Inner error bars represent statistical uncertainties, outer error bars represent statistical and systematic uncertainties added in quadrature. The LO color singlet (CSM) and NLO color octet (COM) predictions for SPS production are shown in comparison.

8.1 Comparison with theoretical expectations

The DPS-subtracted cross section ratio can be compared with theoretical expectations for the $W^{\pm}$ + prompt J/ψ production from the Color Singlet Model and Color Octet Model, as described in Chapter 2.

For comparison of the DPS-subtracted ratio to theory, we normalize the leading-order color singlet (CSM) and next-to-leading-order color octet (COM) predictions for $W^{\pm}$ + prompt J/ψ [44] to next-to-next-to-leading-order predictions for the $W^{\pm}$ production cross section derived from FEWZ 3.1.B2 [76, 77]. The expected SPS cross section ratio $R_{J/\psi}^{\text{DPS sub}}$ from normalized next-to-leading-order color octet calculations is $(4.6 - 6.2) \times 10^{-8}$. The COM predictions do not include any color singlet diagrams. The renormalization (μ_R) and factorization (μ_F) scales are set to the $W^{\pm}$ boson mass $\mu_R = \mu_F = M_W$ and the NRQCD scale μ_Λ is taken to be $\mu_\Lambda = m_{\text{charm}} = 1.5$ GeV. Two sets of color octet long-distance matrix elements are used as input parameters to the theory, obtained from two different parameter fits to experimental data [78, 79], and the variation in the results obtained is assigned as a systematic uncertainty. The normalized leading-order color singlet model predicts the SPS ratio to be $(10 - 32) \times 10^{-8}$ for the phase space region considered in this analysis [45]. The CSM predictions include contributions from $sg \to J/\psi + c + W$ and $q\bar{q}' \to \gamma^* W \to J/\psi W$, and account for indirect production to the $W^{\pm}$ + prompt J/ψ rate through decays of excited charmonium states of both $W^{\pm}$ + direct $\psi(2S)$ and $W^{\pm}$ + direct χ_{cJ} production. The uncertainties on the color singlet prediction arise from the combined variations of the charm quark mass in the range $m_{\text{charm}} = 1.5 \pm 0.1$ and independent variation of the factorization and renormalization scales between $0.75 \times \mu_{R,F}$ and $2 \times \mu_{R,F}$ of their central value $\mu_R = \mu_F = M_W$.

The leading-order CSM contributions are nearly an order of magnitude larger than the next-to-leading-order COM contributions, with the CSM prediction being consistent with the measured DPS-subtracted rate within the current experimental and theoretical uncertainties, emphasising that far from being a distinctive signature of COM production, CSM contributions appear to dominate this process. This shortfall in the COM production prediction might be explained by the presence of large higher-order contributions [78, 79] or a possible breakdown of NRQCD universality [33]. Figure 7.4 supports the hypothesis of DPS factorization (within current experimental uncertainties), but possible modifications to this formalism may also modify the DPS-subtracted rate. Nonetheless, large uncertainties on our result imply that current predictions for SPS production are compatible with the measurement at the 2 sigma level.

8.2 Sources of uncertainty

There are various sources of uncertainty associated with the search for the associated production of $W^{\pm} + J/\psi$ and the measurement of the cross section ratio $R_{J/\psi}$. The main uncertainties are statistical, due to the low number of events. In particular, for the observation of the process, uncertainties due to the fit procedure have to be taken into account. On the other hand, for the measurement of the ratio $R_{J/\psi}$, additional systematic uncertainties manifest themselves because of certain analysis assumptions or choices, such as the kinematics of the W boson, the J/ψ muon efficiencies and momentum scale, as well as the J/ψ spin-alignment. Some possible sources of systematic uncertainties cancel out in the ratio, and are not considered, such as uncertainties related to the W boson.

8.2.1 W boson kinematics

The W boson can exhibit different kinematic properties in inclusive W and $W^{\pm}$+prompt J/ψ events depending on its production mechanism. For example, the process $q\bar{q} \to Wg$ would contribute differently to W and $W^{\pm}$ + prompt J/ψ production. Since we are calculating the cross section ratio $R_{J/\psi}$, as defined in Eq. 5.2 in Section 5.1, we assume the detector can reconstruct the W boson in inclusive W events with the same efficiency as in $W^{\pm}$ + prompt J/ψ events. This helps simplify the ratio, as these efficiencies cancel out:

$$R_{J/\psi} = \mathrm{BR}(J/\psi \to \mu^+\mu^-)\frac{\mathrm{N}(W^{\pm}+\ J/\psi)}{\mathrm{N(W)}}\frac{\epsilon(W \text{ in inclusive})\mathcal{A}(W \text{ in inclusive})}{\epsilon(W \text{ in } W^{\pm}+J/\psi)\mathcal{A}(W \text{ in } W^{\pm}+J/\psi)\epsilon(J/\psi)\mathcal{A}(J/\psi)} \tag{8.1}$$

This cancellation is not guaranteed. The efficiency of finding the W boson in different physics processes depends strongly on the kinematics of the W boson. To estimate the systematic uncertainty associated with this effect, we investigate the variation of W reconstruction efficiency as a function of W p_{T} in Monte Carlo (MC) simulated W boson events, using different MC generators. The different MC generators make different assumptions about the production mechanism behind the W boson, and may include higher order calculations as well. In particular, we use ALPGEN [63] and PYTHIA [67] as leading-order simulations, and POWHEG [80]+JIMMY [81], POWHEG+PYTHIA and MC@NLO [64] as next-to-leading-order simulations.

The efficiency of reconstructing the W boson is defined as the number of events with a reconstructed W boson with muon p_{T} greater than 25 GeV, absolute muon pseudorapidity less than 2.4, missing transverse momentum greater than 20 GeV, and W transverse mass greater than 40 GeV, over the number of events with generator level, or "true", muon, neutrino and W boson properties with the same requirements. The efficiency is calculated per W p_{T} bin of size 5 GeV, and is shown in Fig. 8.4.

Using the sPlot technique [65], we plot the W transverse mass and momentum distributions for the $W^{\pm}$ + prompt J/ψ case, in Fig. 8.4. Using the efficiencies obtained from the inclusive W boson MC in Fig. 8.5, we obtain the weighted average efficiency for the W boson in $W^{\pm}$ + prompt J/ψ events, as shown in Table 8.4. We compare the average efficiency for W reconstruction in inclusive W events in PYTHIA and ALPGEN MC with the average efficiency for W reconstruction in $W^{\pm}$ + prompt J/ψ events using the same MC generators. We take the maximum variation in efficiency of reconstructing the W boson in inclusive W events (between ALPGEN and PYTHIA) compared to the efficiency of reconstructing the W boson in $W^{\pm}$+prompt J/ψ events as the systematic uncertainty due to the assumption that the efficiency of finding the W boson in inclusive W and $W^{\pm}$ + prompt J/ψ events is the same. This effect is found to be 2.2% in the barrel and 4.8% in the endcap for the maximum variation from the MC simulation, which we use for the results in Chapter 8.

Efficiency to reconstruct W boson in inclusive W and $W^{\pm}$ + prompt J/ψ events			
MC simulation	ALPGEN	PYTHIA	Maximum variation from inclusive
W in inclusive W events	$62.0 \pm 0.04\%$	$64.2 \pm 0.05\%$	
W in $W^{\pm}$ + prompt J/ψ events with J/ψ in barrel	$63.4 \pm 0.8\%$	$65.0 \pm 0.7\%$	2.2%
W in $W^{\pm}$ + prompt J/ψ events with J/ψ in endcap	$62.9 \pm 1.9\%$	$61.1 \pm 1.9\%$	4.8%

Table 8.4: The average efficiency to reconstruct the W boson in inclusive W and $W^{\pm}$ + prompt J/ψ events, using ALPGEN and PYTHIA simulation for the W boson kinematics.

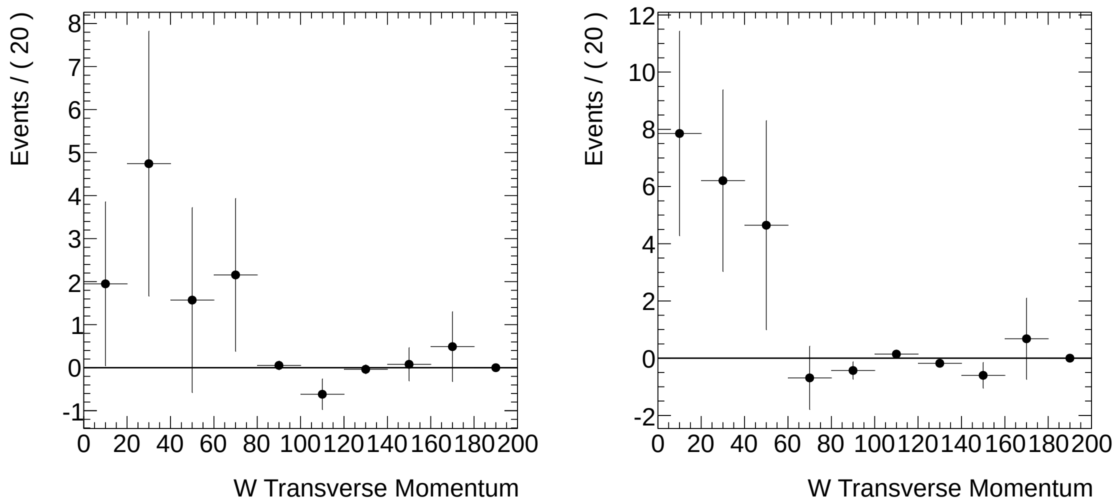

Figure 8.4: sPlot-weighted W boson transverse momentum distribution for the $W^{\pm}$ + prompt J/ψ candidates in the barrel ($0 < J/\psi\ |y| < 1$) (left) and endcap ($1 < J/\psi\ |y| < 2.1$) (right).

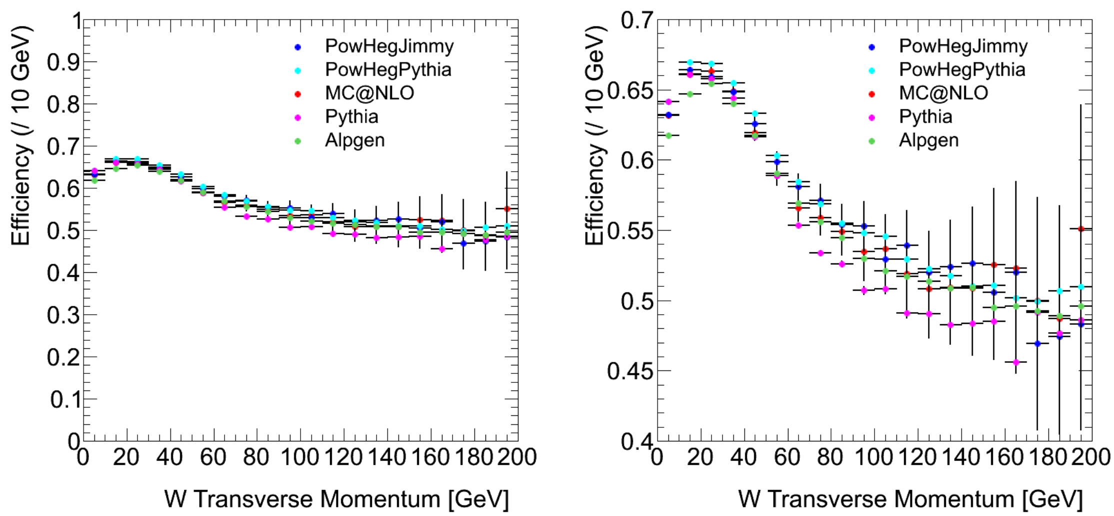

Figure 8.5: The efficiency of finding the W boson with our selection varies as a function of W transverse momentum, and is shown here for ALPGEN and ALPGEN leading-order MC simulated events. Next-to-leading-order simulations, POWHEG+JIMMY,POWHEG+PYTHIA and MC@NLO are also shown, to verify the variation of efficiency as a function of W transverse momentum. The left plot shows the full range in efficiency, while the right plot focuses on the range in efficiency $[0.4 - 0.7]$.

8.2.2 J/ψ muon efficiencies

The efficiency of the J/ψ muons is calculated using the tag-and-probe method, as described in Section 5.4. The efficiency is calculated for various bins in muon pseudorapidity, charge and transverse momentum. The uncertainty is estimated to take into account the differences in the central value of the efficiency that come from different functional forms from the fit model in the tag-and-probe method. This effect is typically small, but can change the muon efficiencies by up to 5% for some bins, usually bins with low statistics, such as those at low p_T. As a result, the cross section ratio $R_{J/\psi}$ can change, depending on the uncertainty on the efficiency of the two J/ψ muons. In addition to the tag-and-probe method in data, we performed the same procedure using Monte Carlo simulated samples of J/ψ production. The difference in the results between using the data-driven efficiencies and the simulated efficiencies, amounts to 3–5%, and is taken as the systematic uncertainty due to the J/ψ muon efficiencies.

8.2.3 J/ψ muon momentum scale

The momentum scale of the J/ψ muons is not known with complete precision. Often, the J/ψ muons have very low p_T, at the limit of the allowed p_T range of our requirements, as shown in Section 5.3. Small shifts in the muon momentum scale, could shift the number of reconstructed J/ψ. To find the extent of this effect, we shift the muon momentum scale by the uncertainty on the muon p_T and measure the number of J/ψ candidates in the two regions, barrel and endcap, before and after the shifting. The difference in the raw number of reconstructed J/ψ is taken as the systematic uncertainty due to the muon momentum scale.

The results of this procedure show a very small effect on the number of muons, as shown in Table 8.5. This is due to the fact that by allowing one muon to have transverse momentum above 2.5 GeV or to be segment-tagged muon, and considering the J/ψ transverse momentum lower bound of 8.5 GeV, the J/ψ muon momentum scale uncertainty does not have a sizeable effect on the number of candidates we detect.

Raw number of reconstructed J/ψ with transverse momentum $8.5 - 10$ GeV		
Detector Region	Nominal Momentum Scale	Shifted Momentum Scale
Barrel ($\|y\| < 1$)	1808772	1808775
Endcap ($1 < \|y\| < 2.1$)	1337563	1337602

Table 8.5: The raw number of reconstructed J/ψ with momentum $8.5-10$ GeV, with muons with nominal and shifted momentum scale. The difference is 2×10^{-6} in the barrel and 3×10^{-5} in the endcap.

8.2.4 Summary of systematic uncertainties

To summarize the systematic uncertainties associated with the ratio measurement, Table 8.6 shows the main sources and their effects, excluding the yield extraction uncertainties. The systematic due to the spin-alignment assumption is quoted separately; the quadratic sum of the other systematics is $^{+6.1}_{-5.8}\%$ in the barrel and $^{+7.1}_{-7.1}\%$ in the endcap. This analysis is dominated by the statistical uncertainties of $^{+47.2}_{-39.7}\%$ in the barrel and $^{+30.2}_{-26.7}\%$ in the endcap.

Summary of uncertainties		
Source	Barrel	Endcap
W boson kinematics	2.2%	4.8%
J/ψ daughter muon efficiency	3–5%	3–5%
muon momentum scale	0.0002%	0.003%
fit procedure	$^{+2.8}_{-1.8}\%$	$^{+1.5}_{-1.4}\%$
fit nuisance parameters choice	1%	1%
fit functional forms choice	4%	4%
statistical	$^{+47}_{-40}\%$	$^{+30}_{-27}\%$

Table 8.6: Summary of the main sources of systematic uncertainties for the ratio measurement. The systematic uncertainty is found to be $^{+7}_{-7}\%$ in the barrel and $^{+8}_{-8}\%$ in the endcap. The analysis is dominated by the statistical uncertainties of $^{+47}_{-40}\%$ in the barrel and $^{+30}_{-27}\%$ in the endcap.

Chapter 9
Conclusions

πήραμε τη ζωη μας ·λάθος!
κι αλλάξαμε ζωή.

– Γιώργος Σεφέρης, *Άρνηση*

The first observation of associated production of W and J/ψ was presented in this thesis, along with a measurement of its production cross section. The analysis was performed on proton–proton collisions from the Large Hadron Collider at a center of mass energy of 7 TeV, using 4.5 fb^{-1} of data collected by the ATLAS detector during 2011. The decay channels $W \to \mu\nu$ and $J/\psi \to \mu\mu$ were utilized to search for the W and J/ψ. Prompt J/ψ were separated using a fit on the J/ψ pseudo-proper time. There was no discrimination between directly produced J/ψ and χ feeddown resulting into J/ψ.

A total of $27.4^{+7.5}_{-6.5}$ $W^{\pm}$ + prompt J/ψ events were observed, with a statistical significance of 5.1σ. The observed production rate was measured as a ratio to the inclusive $W^{\pm}$ boson production rate. Multiple parton interactions in the colliding protons are expected to contribute significantly to the observed rate, and the double parton scattering contribution to the total cross-section was estimated.

The results were compared with predictions from two of the leading theoretical models that aim to explain the mechanism for J/ψ production the Color Singlet Model and the Color Octet Model. The measurement yields results that are slightly over the model predictions, albeit with a large statistical error. Hence, we do not have a definitive answer for the questions behind the mechanism for J/ψ production. However, as this is the first measurement of the $W^{\pm}$ + prompt J/ψ cross section, it paves the way towards better understanding the J/ψ production mechanism, and answering this long-standing question.

Additionally, this benchmark analysis opens the way for future searches for even rarer processes, such as the associated production of Z boson and J/ψ and the associated production of Υ and vector boson. Measuring all these processes will allow for a more precise characterization of the charmonium and bottomonium production, and will provide much needed feedback to phenomenologists to refine their theoretical models. More data, as is expected from the next LHC Run, will enable a more precise measurement of the $W^{\pm}$ + prompt J/ψ

process and the probing of the aforementioned processes. Furthermore, since this measurement occurred at a center of mass energy of 7 TeV and ATLAS has data for 8 TeV, and will operate at 14 TeV in the future, there is potential for a differential cross section measurement of the $W^{\pm} + J/\psi$ process.

Importantly, observing and measuring the $W^{\pm} +$ prompt J/ψ process demonstrates the strength and versatility of the ATLAS detector physics program, as well as the LHC. Using all parts of the detector, we were able to look for a rare process, discover it, and measure its properties. Being the first observation of associated production of charmonium with a vector boson, the analysis described in this thesis breaks new ground in the pursuit for knowledge that we strive for in science.

Bibliography

[1] S. Weinberg, *A Model of Leptons*, Phys.Rev.Lett. **19** (1967) 1264–1266.

[2] S. Glashow, *Partial Symmetries of Weak Interactions*, Nucl.Phys. **22** (1961) 579–588.

[3] A. Salam, *in "Elementary Particle Theory "*, ed. N. Svartholm, Almqvist and Wiksells (1969) 367.

[4] L. V. P. R. de Broglie, *Recherches sur la thÃľorie des quanta*, Annals Phys. **2** (1925) 22–128.

[5] R. Feynman, *Space - time approach to quantum electrodynamics*, Phys.Rev. **76** (1949) 769–789.

[6] UA1 Collaboration, G. Arnison et al., *Experimental Observation of Isolated Large Transverse Energy Electrons with Associated Missing Energy at s**(1/2) = 540-GeV*, Phys.Lett. **B122** (1983) 103–116.

[7] UA2 Collaboration, M. Banner et al., *Observation of Single Isolated Electrons of High Transverse Momentum in Events with Missing Transverse Energy at the CERN anti-p p Collider*, Phys.Lett. **B122** (1983) 476–485.

[8] UA1 Collaboration, G. Arnison et al., *Experimental Observation of Lepton Pairs of Invariant Mass Around 95-GeV/c**2 at the CERN SPS Collider*, Phys.Lett. **B126** (1983) 398–410.

[9] F. Englert and R. Brout, *Broken Symmetry and the Mass of Gauge Vector Mesons*, Phys.Rev.Lett. **13** (1964) 321–323.

[10] P. W. Higgs, *Broken symmetries, massless particles and gauge fields*, Phys.Lett. **12** (1964) 132–133.

[11] ATLAS Collaboration, G. Aad et al., *Observation of a new particle in the search for the Standard Model Higgs boson with the ATLAS detector at the LHC*, Phys.Lett. **B716** (2012) 1–29, `arXiv:1207.7214 [hep-ex]`.

[12] CMS Collaboration, S. Chatrchyan et al., *Observation of a new boson at a mass of 125 GeV with the CMS experiment at the LHC*, Phys.Lett. **B716** (2012) 30–61, `arXiv:1207.7235 [hep-ex]`.

[13] M. Gell-Mann, *A Schematic Model of Baryons and Mesons*, Phys.Lett. **8** (1964) 214–215.

[14] H. D. Politzer, *Reliable Perturbative Results for Strong Interactions?*, Phys.Rev.Lett. **30** (1973) 1346–1349.

[15] D. Gross and F. Wilczek, *Asymptotically Free Gauge Theories. 1*, Phys.Rev. **D8** (1973) 3633–3652.

[16] D. Gross and F. Wilczek, *Asymptotically Free Gauge Theories. 2*, Phys.Rev. **D9** (1974) 980–993.

[17] S. Herb, D. Hom, L. Lederman, J. Sens, H. Snyder, et al., *Observation of a Dimuon Resonance at 9.5-GeV in 400-GeV Proton-Nucleus Collisions*, Phys.Rev.Lett. **39** (1977) 252–255.

[18] N. Brambilla, A. Pineda, J. Soto, and A. Vairo, *Potential NRQCD: An Effective theory for heavy quarkonium*, Nucl.Phys. **B566** (2000) 275, `arXiv:hep-ph/9907240 [hep-ph]`.

[19] SLAC-SP-017 Collaboration, J. Augustin et al., *Discovery of a Narrow Resonance in e+ e- Annihilation*, Phys.Rev.Lett. **33** (1974) 1406–1408.

[20] E598 Collaboration, J. Aubert et al., *Experimental Observation of a Heavy Particle J*, Phys.Rev.Lett. **33** (1974) 1404–1406.

[21] M. Kobayashi and T. Maskawa, *CP Violation in the Renormalizable Theory of Weak Interaction*, Prog.Theor.Phys. **49** (1973) 652–657.

[22] N. Cabibbo, *Unitary Symmetry and Leptonic Decays*, Phys.Rev.Lett. **10** (1963) 531–533.

[23] CDF Collaboration, F. Abe et al., *Observation of top quark production in $\bar{p}p$ collisions*, Phys.Rev.Lett. **74** (1995) 2626–2631, `arXiv:hep-ex/9503002 [hep-ex]`.

[24] D0 Collaboration, S. Abachi et al., *Observation of the top quark*, Phys.Rev.Lett. **74** (1995) 2632–2637, `arXiv:hep-ex/9503003 [hep-ex]`.

[25] Particle Data Group Collaboration, J. Beringer et al., *Review of Particle Physics (RPP)*, Phys. Rev. **D86** (2012) 010001.

[26] S. Okubo, *Phi meson and unitary symmetry model*, Phys.Lett. **5** (1963) 165–168.

[27] G. Zweig, *An SU(3) model for strong interaction symmetry and its breaking. Pt. 1*, .

[28] J. Iizuka, *Systematics and phenomenology of meson family*, Prog.Theor.Phys.Suppl. **37** (1966) 21–34.

[29] Quarkonium Working Group Collaboration, N. Brambilla et al., *Heavy quarkonium physics*, `arXiv:hep-ph/0412158 [hep-ph]`.

[30] N. Brambilla, S. Eidelman, B. Heltsley, R. Vogt, G. Bodwin, et al., *Heavy quarkonium: progress, puzzles, and opportunities*, Eur. Phys. J. **C71** (2011) 1534, `arXiv:1010.5827 [hep-ph]`.

[31] J. Lansberg, *On the mechanisms of heavy-quarkonium hadroproduction*, Eur. Phys. J. **C61** (2009) 693–703, `arXiv:0811.4005 [hep-ph]`.

[32] M. Butenschoen and B. A. Kniehl, *World data of J/psi production consolidate NRQCD factorization at NLO*, Phys. Rev. **D84** (2011) 051501, `arXiv:1105.0820 [hep-ph]`.

[33] M. Butenschoen and B. A. Kniehl, *Next-to-leading-order tests of NRQCD factorization with J/ψ yield and polarization*, Mod. Phys. Lett. A, Vol. 28, No. **9** (2013) 1350027, `arXiv:1212.2037 [hep-ph]`.

[34] S. Baranov, A. Lipatov, and N. Zotov, *Prompt J/Ψ production at LHC: new evidence for the k_t-factorization*, Phys. Rev. **D85** (2012) 014034, `arXiv:1108.2856 [hep-ph]`.

[35] Y.-Q. Ma, K. Wang, and K.-T. Chao, *A complete NLO calculation of the J/ψ and ψ' production at hadron colliders*, Phys. Rev. **D84** (2011) 114001, `arXiv:1012.1030 [hep-ph]`.

[36] J. C. Collins, D. E. Soper, and G. F. Sterman, *Heavy Particle Production in High-Energy Hadron Collisions*, Nucl.Phys. **B263** (1986) 37.

[37] W. Caswell and G. Lepage, *Effective Lagrangians for Bound State Problems in QED, QCD, and Other Field Theories*, Phys.Lett. **B167** (1986) 437.

[38] G. T. Bodwin, E. Braaten, and G. P. Lepage, *Rigorous QCD analysis of inclusive annihilation and production of heavy quarkonium*, Phys. Rev. **D51** (1995) 1125–1171, `arXiv:hep-ph/9407339 [hep-ph]`.

[39] P. L. Cho and A. K. Leibovich, *Color octet quarkonia production*, Phys.Rev. **D53** (1996) 150–162, `arXiv:hep-ph/9505329 [hep-ph]`.

[40] P. L. Cho and A. K. Leibovich, *Color octet quarkonia production. 2.*, Phys.Rev. **D53** (1996) 6203–6217, `arXiv:hep-ph/9511315 [hep-ph]`.

[41] CDF Collaboration, D. Acosta et al., *Measurement of the J/ψ meson and $b-$hadron production cross sections in $p\bar{p}$ collisions at $\sqrt{s} = 1960\ GeV$*, Phys.Rev. **D71** (2005) 032001, `arXiv:hep-ex/0412071 [hep-ex]`.

[42] J. Amundson, O. J. Eboli, E. Gregores, and F. Halzen, *Quantitative tests of color evaporation: Charmonium production*, Phys.Lett. **B390** (1997) 323–328, `arXiv:hep-ph/9605295 [hep-ph]`.

[43] B. A. Kniehl, C. P. Palisoc, and L. Zwirner, *Associated production of heavy quarkonia and electroweak bosons at present and future colliders*, Phys. Rev. **D66** (2002) 114002, `arXiv:hep-ph/0208104 [hep-ph]`.

[44] G. Li, M. Song, R.-Y. Zhang, and W.-G. Ma, *QCD corrections to J/ψ production in association with a W-boson at the LHC*, Phys. Rev. **D83** (2011) 014001, `arXiv:1012.3798 [hep-ph]`.

[45] J. Lansberg and C. Lorce, *Reassessing the importance of the colour-singlet contributions to direct $J/\psi + W$ production at the LHC and the Tevatron*, Phys. Lett. **B 726** (2013) 218 – 222, `arXiv:1303.5327 [hep-ph]`.

[46] CDF Collaboration, *Search for associated production of Υ and vector boson in $p\bar{p}$ collisions at $\sqrt{s} = 1.8$ TeV*, Phys. Rev. Lett. **90** (2003) 221803.

[47] L. Evans and P. Bryant, *LHC Machine*, JINST **3** (2008) S08001.

[48] R. R. Wilson, *The Tevatron*, Phys.Today **30N10** (1977) 23–30.

[49] ATLAS Collaboration, G. Aad et al., *The ATLAS Experiment at the CERN Large Hadron Collider*, JINST **3** (2008) S08003.

[50] CMS Collaboration, S. Chatrchyan et al., *The CMS experiment at the CERN LHC*, JINST **3** (2008) S08004.

[51] ALICE Collaboration, K. Aamodt et al., *The ALICE experiment at the CERN LHC*, JINST **3** (2008) S08002.

[52] LHCb Collaboration, J. Alves, A. Augusto et al., *The LHCb Detector at the LHC*, JINST **3** (2008) S08005.

[53] S. Hassani, L. Chevalier, E. Lancon, J. Laporte, R. Nicolaidou, et al., *A muon identification and combined reconstruction procedure for the ATLAS detector at the LHC using the (MUONBOY, STACO, MuTag) reconstruction packages*, Nucl.Instrum.Meth. **A572** (2007) 77–79.

[54] ATLAS Collaboration, G. Aad et al., *Performance of Missing Transverse Momentum Reconstruction in Proton-Proton Collisions at 7 TeV with ATLAS*, Eur.Phys.J. **C72** (2012) 1844, `arXiv:1108.5602 [hep-ex]`.

[55] ATLAS Collaboration, *ATLAS first level trigger: Technical design report*, .

[56] ATLAS Collaboration, *ATLAS high-level trigger, data acquisition and controls: Technical design report*, .

[57] CDF Collaboration, W. Ashmanskas et al., *Silicon vertex tracker: A Fast precise tracking trigger for CDF*, Nucl.Instrum.Meth. **A447** (2000) 218–222.

[58] ATLAS Collaboration, *Fast TracKer (FTK) Technical Design Report*, Tech. Rep. CERN-LHCC-2013-007. ATLAS-TDR-021, CERN, Geneva, Jun, 2013. ATLAS Fast Tracker Technical Design Report.

[59] A. Andreani, A. Andreazza, A. Annovi, M. Beretta, V. Bevacqua, M. Bogdan, E. Bossini, A. Boveia, F. Canelli, Y. Cheng, M. Citterio, F. Crescioli, M. Dell'Orso, G. Drake, M. Dunford, J. F. Genat, P. Giannetti, F. Giorgi, J. Hoff, A. Kapliy, M. Kasten, Y. Kim, N. Kimura, A. Lanza, V. Liberali, T. Liu, A. McCarn,

C. Melachrinos, C. Meroni, A. Negri, M. Neubauer, M. Piendibene, J. Proudfoot, G. Punzi, M. Riva, F. Sabatini, I. Sacco, L. Sartori, M. Shochet, A. Stabile, F. Tang, A. Todri, R. Tripiccione, J. Tuggle, V. Vercesi, M. Villa, R. A. Vitullo, G. Volpi, J. Wu, K. Yorita, and J. Zhang, *The Fast Track real time processor and its impact on muon isolation, tau and b-jet online selections at ATLAS*, in *Real Time Conference (RT), 2010 17th IEEE-NPSS*, pp. 1–8. 2010.

[60] ATLAS Collaboration, *Measurement of the inclusive $W^{\pm}$ and Z/gamma cross sections in the electron and muon decay channels in pp collisions at $\sqrt{s} = 7$ TeV with the ATLAS detector*, Phys. Rev. **D85** (2012) 072004, `arXiv:1109.5141 [hep-ex]`.

[61] ATLAS Collaboration, *Measurement of the differential cross-sections of inclusive, prompt and non-prompt J/ψ production in proton-proton collisions at $\sqrt{s} = 7$ TeV*, Nucl. Phys. **B850** (2011) 387–444, `arXiv:1104.3038 [hep-ex]`.

[62] ATLAS Collaboration, *Determination of the muon reconstruction efficiency in ATLAS at the Z resonance in proton-proton collisons at sqrt(s)=7 TeV*, .

[63] M. L. Mangano, M. Moretti, F. Piccinini, R. Pittau, and A. D. Polosa, *ALPGEN, a generator for hard multiparton processes in hadronic collisions*, JHEP **0307** (2003) 001, `arXiv:hep-ph/0206293 [hep-ph]`.

[64] S. Frixione, P. Nason, and B. R. Webber, *Matching NLO QCD and parton showers in heavy flavor production*, JHEP **0308** (2003) 007, `arXiv:hep-ph/0305252 [hep-ph]`.

[65] M. Pivk and F. R. Le Diberder, *SPlot: A Statistical tool to unfold data distributions*, Nucl. Instrum. Meth. **A555** (2005) 356–369, `arXiv:physics/0402083 [physics.data-an]`.

[66] ATLAS Collaboration, *Luminosity Determination in pp Collisions at $\sqrt{s} = 7$ TeV Using the ATLAS Detector at the LHC*, Eur. Phys. J. **C71** (2011) 1630, `arXiv:1101.2185 [hep-ex]`.

[67] T. Sjostrand, S. Mrenna, and P. Z. Skands, *A Brief Introduction to PYTHIA 8.1*, Comput. Phys. Commun. **178** (2008) 852–867, `arXiv:0710.3820 [hep-ph]`.

[68] J. Alwall, P. Demin, S. de Visscher, R. Frederix, M. Herquet, et al., *MadGraph/MadEvent v4: The New Web Generation*, JHEP **0709** (2007) 028, `arXiv:0706.2334 [hep-ph]`.

[69] CDF Collaboration, *Double parton scattering in $\bar{p}p$ collisions at $\sqrt{s} = 1.8$ TeV*, Phys. Rev. **D56** (1997) 3811–3832.

[70] D. Treleani, *Double parton scattering, diffraction and effective cross section*, Phys. Rev. **D76** (2007) 076006, `arXiv:0708.2603 [hep-ph]`.

[71] ATLAS Collaboration, *Measurement of hard double-parton interactions in $W \to \ell\nu +$ 2 jet events at sqrt(s)=7 TeV with the ATLAS detector*, New J. Phys. **15** (2013) 033038, arXiv:1301.6872 [hep-ex].

[72] W. Verkerke and D. P. Kirkby, *The RooFit toolkit for data modeling*, eConf **C0303241** (2003) MOLT007, arXiv:physics/0306116 [physics].

[73] G. Cowan, *Statistical data analysis*, .

[74] F. James, *Statistical methods in experimental physics*, .

[75] ATLAS Collaboration, *Measurement of the cross section for the production of a W boson in association with b^- jets in pp collisions at $\sqrt{s} = 7$ TeV with the ATLAS detector*, Phys. Lett. **B707** (2012) 418–437, arXiv:1109.1470 [hep-ex].

[76] R. Gavin, Y. Li, F. Petriello, and S. Quackenbush, *FEWZ 2.0: A code for hadronic Z production at next-to-next-to-leading order*, Comput. Phys. Commun. **182** (2011) 2388–2403, arXiv:1011.3540 [hep-ph].

[77] R. Gavin, Y. Li, F. Petriello, and S. Quackenbush, *W Physics at the LHC with FEWZ 2.1*, arXiv:1201.5896 [hep-ph].

[78] M. Butenschoen and B. A. Kniehl, *J/ψ production in NRQCD: A global analysis of yield and polarization*, Nucl. Phys. Proc. Suppl. **222-224** (2012) 151–161, arXiv:1201.3862 [hep-ph].

[79] K.-T. Chao, Y.-Q. Ma, H.-S. Shao, K. Wang, and Y.-J. Zhang, *J/ψ Polarization at Hadron Colliders in Nonrelativistic QCD*, Phys. Rev. Lett. **108** (2012) 242004, arXiv:1201.2675 [hep-ph].

[80] S. Frixione, P. Nason, and C. Oleari, *Matching NLO QCD computations with Parton Shower simulations: the POWHEG method*, JHEP **0711** (2007) 070, arXiv:0709.2092 [hep-ph].

[81] M. Bahr, S. Gieseke, M. Gigg, D. Grellscheid, K. Hamilton, et al., *Herwig++ Physics and Manual*, Eur.Phys.J. **C58** (2008) 639–707, arXiv:0803.0883 [hep-ph].